

CFD modeling of the flow over Pedrógão dam spillway and roller bucket

Timo Methler

Thesis to obtain the Master of Science Degree in
Energy Engineering and Management

Supervisors: Prof. Jorge de Saldanha Gonçalves Matos

Dr. José Falcão de Melo

Examination Committee

Chairperson: Prof. José Alberto Caiado Falcão de Campos

Supervisor: Prof. Jorge de Saldanha Gonçalves Matos

Member of the Committee: Prof. Inês Osório de Castro Meireles

November 2018

I declare that this document is an original work of my own authorship and that it fulfils
all the requirements of the Code of Conduct and Good Practices of the
Universidade de Lisboa.

This thesis is dedicated to everybody who is conscious about the environment and serious about saving our planet. I am proud to count myself into this category and plan to contributing to our cause my whole life.

Let's celebrate our cause with a quote translated from a German song by "Die Ärzte":

"Es ist nicht deine Schuld das die Welt ist wie sie ist, es ist nur deine Schuld wenn sie so bleibt"

"It's not your fault that the world is as it is, it's only your fault if it stays the same"

Acknowledgements

I am very grateful and thankful for all the effort, time, provided knowledge, discussions, encouragement and moral support my supervisor Prof. Dr. Jorge Matos gave me during the process of this thesis. I am also very thankful for the very fast response and constructive feedback of my co-supervisor Dr. José Falcão de Melo. My thanks also belong to Prof. Dr. José María Carrillo in guiding my first experiences with Flow 3D®. A thank you goes also out to the company EDIA - *Empresa de Desenvolvimento e Infra-estruturas do Alqueva, S.A.*, for providing me with a tour of Alqueva and Pedrógão dams and for granting the access to information on the Pedrógão dam and respective hydraulic model study.

I would also like to acknowledge the great support of all the staff of Instituto Superior Técnico especially Ágata Nicolau for the support in all the paperwork. A very grateful thank you also belongs to Prof. Dr. José Falcão de Campos, coordinator of the MEGE program, for adapting, listening and dealing with the many issues and problems me and my colleges bring to him.

Inno energy for all the financial support in form of the scholarship, the network support in form of all the different events we could go to and were supported in attending them. And especially to Cornelia Schwenk and Marta Ramilo Abrantes for supporting us in the guideline jungle, a double degree brings with it.

And finally, a thank you to my family in supporting me financially as well as mentally through the whole process of my 7 yearlong study experience.

Abstract

The last three decades have witnessed a significant increase in the use of stepped spillways, which is closely linked to the roller compacted concrete technique applied to dam engineering.

This dissertation presents a numerical study of the flow over Pedrógão dam spillway and roller bucket using the Computational Fluid Dynamics (CFD) software code FLOW-3D[®]. The study embraced the analysis of CFD simulations on both prototype and physical model scales. Flow characteristics along the ogee crest, the stepped chute and the roller bucket, including flow depths and pressure heads, were evaluated and compared with those previously acquired on a physical model, assembled at the Laboratório Nacional de Engenharia Civil (LNEC).

In general, a fair agreement was found between numerical and experimental flow depth and pressure head data along an initial reach of the stepped chute and the roller bucket. However, considerable differences were obtained on the pressure head on the curved reach of the ogee crest. In fact, the mesh resolution in this initial reach was found to greatly influence the pressure head. Also, non-negligible impact of CFD scaling was found with regard to the flow depth and pressure head results. In general, the model scale CFD simulations were found to provide a better agreement with the physical model data.

The comparative analysis undertaken in this study indicate that CFD modelling on complex hydraulic structures, such as stepped spillways and roller buckets, remains a challenge for future research.

Keywords: stepped spillway; ogee crest; roller bucket; skimming flow; CFD simulation; FLOW-3D[®]

Resumo

Nas últimas três décadas verificou-se um aumento significativo no uso de descarregadores de cheias em degraus, o que se deve essencialmente à técnica de betão compactado por cilindros aplicada à construção de barragens.

Nesta dissertação, apresenta-se um estudo numérico do escoamento no descarregador de cheias e na bacia de dissipação de energia por rolo da barragem de Pedrógão, usando o software de Dinâmica dos Fluidos Computacional (CFD) FLOW-3D®. O estudo engloba a análise de CFD às escalas do protótipo e do modelo físico. As características do escoamento na soleira descarregadora, no descarregador e na bacia de dissipação, como a altura do escoamento e a altura piezométrica, foram comparadas com as obtidas anteriormente num estudo em modelo físico, no Laboratório Nacional de Engenharia Civil (LNEC).

Em geral, obtiveram-se resultados numéricos próximos dos experimentais para a altura do escoamento e a altura piezométrica, no trecho inicial do descarregador e da bacia de dissipação. Contudo, obtiveram-se diferenças consideráveis para a altura piezométrica no trecho curvo da soleira descarregadora. Com efeito, a resolução da malha neste trecho exerce assinalável influência na altura piezométrica. Observou-se também que a escala usada no modelo CFD teve um impacto não negligenciável nas alturas do escoamento e piezométricas. Em geral, as simulações numéricas à escala do modelo conduziram a resultados mais próximos dos experimentais.

A análise comparativa efetuada neste estudo indica que a modelação CFD do escoamento em estruturas hidráulicas complexas, como descarregadores de cheias em degraus e bacias de dissipação por rolo, constitui um desafio para investigação futura.

Palavras-chave: descarregador de cheias em degraus; soleira descarregadora; bacia de dissipação de energia por rolo; escoamento deslizante sobre turbilhões; simulação CFD; FLOW-3D®

Table of Contents

Acknowledgements	vii
Abstract.....	ix
Resumo.....	x
Table of Contents	xi
List of Figures	xiv
List of Tables	xvii
List of Acronyms	xviii
List of Symbols	xix
List of Software	xxii
1 Introduction	1
1.1 Overview.....	1
1.2 Objectives.....	2
1.3 Organization	2
2 Literature review	4
2.1 Preliminary remarks.....	4
2.2 Spillways.....	5
2.3 Stepped spillway concept	5
2.3.1 Stepped spillway flow conditions.....	6
2.3.2 Nappe flow	6
2.3.3 Skimming flow	7
2.4 Flow depth along the chute.....	9
2.4.1 Analytical method	9
2.4.2 Empirical formulae.....	9
3 Mathematical and numerical models.....	12
3.1 Preliminary remarks.....	12

3.2	Numerical environment.....	13
3.3	Governing equations and models	14
3.3.1	Mass continuity equation	14
3.3.2	Momentum conservation equations	15
3.3.3	Volume of fluid model (VOF).....	16
3.4	Turbulence models	17
3.4.1	k- ϵ model	18
3.4.2	RNG k- ϵ model.....	18
3.4.3	General remarks.....	19
3.5	Finite difference solution method.....	19
3.6	Flow 3D boundary conditions	20
3.6.1	Free-slip boundary.....	20
3.6.2	Fixed pressure/velocity boundary.....	20
3.6.3	Time dependent boundary	20
3.6.4	Outflow boundary	20
3.7	Flow 3D specialized bubble tracking	21
3.7.1	Adiabatic bubbles	21
3.7.2	Variable pressure void bubble.....	21
3.7.3	Buoyant flow due to bubbles.....	21
3.8	Mesh generation and “FAVOR” algorithm.....	22
4	Implementation	24
4.1	Preliminary remarks.....	24
4.2	Case study, Pedrógão dam	25
4.2.1	The experimental study and its purpose.....	26
4.2.2	Experimental set-up.....	26
4.2.3	Execution	27
4.2.4	Results and discussion	27
4.3	Creation and import of the 3-dimensional model	27
4.4	Mesh generation and orientation	28
4.5	Boundary condition selection.....	30
4.6	Steady state criterion.....	31
4.7	Probe positioning.....	31
4.7.1	Step probes.....	31
4.7.2	Ogee crest probes and roller bucket probes.....	32
4.7.3	Pressure taps	32
4.8	Experimental flow depths.....	35
4.9	Mesh convergence	36

4.9.1	Chute region.....	36
4.9.2	Roller bucket	39
4.10	Turbulence model selection	40
4.11	Time convergence for velocities on the chute.....	41
5	Results	44
5.1	Preliminary remarks.....	44
5.2	Flow depths on the chute.....	45
5.3	Flow depths on the roller bucket.....	50
5.4	Pressure heads at the ogee crest and roller bucket.....	53
6	Conclusions and outlook	57
6.1	Concluding remarks.....	57
6.2	Outlook	59
	References	60
	Appendix A Simulation result tables.....	A-1
	Appendix B Probe positioning along the chute steps.....	B-1
	Appendix C Export options for Stereolithography models in Inventor ..	C-1
	Appendix D Mesh block documentation	D-1
	Appendix E Original drawings and data extrapolation	E-1
	Appendix F Free surface data extracted from LNEC report	F-1
	Appendix G Steady state screenshots	G-1
	Appendix H Boundary layer recognition coding suggestion	H-1
	Appendix I Simulation overview on different times	I-1

List of Figures

Figure 2 1 Stepped overflow spillway, Melton dam in Australia [3]	5
Figure 2 2 Nappe flow schematic [2].....	6
Figure 2 3 Skimming flow region definitions [4].....	7
Figure 2 4 Sketch of the skimming flow regime, on a spillway with moderate slope [20]	8
Figure 2 5 Flow properties at the interception point: (a) location; (b) equivalent clear water depth (adapted from [18]).....	10
Figure 2 6 Evolution of the normalized equivalent clear-water depth in the nonaerated region: (a) comparison among equation 2.10 and experimental data from the study undertaken at LNEC; (b) comparison among equation 2.10 and experimental data from several studies for similar slope (adapted from [18]).....	11
Figure 3 1 Example cell in a Flow 3D® CFD mesh, with all values and their locations [22].....	13
Figure 3 2 Solid recognition examples by the FAVOR method used in Flow 3D® [22].....	23
Figure 4 1 Alqueva dam, view from downstream	25
Figure 4 2 Pedrógão dam, view from downstream	25
Figure 4 3 Representing slice of Pedrógão dam marking important positions in roller and surge location, from the original report, [32] in [31].	26
Figure 4 4 Single stereolithography triangle with its vertex coordinates and its normal vector, example of stereolithography data format [22].....	28
Figure 4 5 Mesh blocks in the simulated environment.....	28
Figure 4 6 Cell orientation on the constant sloped reach of the stepped spillway.....	29
Figure 4 7 Outline of the individual cells in the ogee crest region for the 1:12 mesh size	30
Figure 4 8 Overview over simulation environment, with isometric colouring for velocity	31
Figure 4 9 Line probe for pressure reading, along the ramp of the roller bucket, slight extension of the line probe is marked	32
Figure 4 10 Manually positioned spline probe.....	33
Figure 4 11 Pressure development along the manually positioned spline probe (increasing x coordinate with distance), screenshot of the output graph in the post processing software FlowSight, adapted axis labels	33
Figure 4 12 Pressure development perpendicular distance evolution, leading away from the crest	34
Figure 4 13 Free surface digital data overlay over original graph	36
Figure 4 14 Free surface elevation in chute region	37
Figure 4 15 (a) Velocity profiles at step 2 ($L/L_i = 0.047$); (b) Velocity profile at step 5 ($L/L_i = 0.084$); (c) Velocity profile at step 10 ($L/L_i = 0.152$); (d) Velocity profile at step 15 ($L/L_i = 0.217$); (e) Velocity profile at step 20 ($L/L_i = 0.282$)	38
Figure 4 16 Relative average velocity differences per step, of different mesh sizes and turbulent models to the 1:12 k- ϵ average velocities over the individual steps	39
Figure 4 17 Free surface elevation in the roller bucket, for different turbulent models and mesh sizes	40
Figure 4 18 Simulation environment with marked analysed steps in the time convergence analysis	41
Figure 4 19 Mass-averaged mean kinetic energy time evolution of the 1:6 k- ϵ 240s simulation	42
Figure 5 1 Free surface elevation along the chute	45
Figure 5 2 Flow depth along the chute.....	46

Figure 5 3 Flow depth results by Bombardelli et al. [5], adapted to have L/L_i axis	47
Figure 5 4 Flow depth differences compared to their experimental counterpart.....	47
Figure 5 5 Flow depths relative differences analytical formulae vs. CFD and experimental data over L/L_i	48
Figure 5 6 Flow depth differences, analytical formulae vs. CFD and experimental results, over L/L_i	49
Figure 5 7 Velocity profiles at step 1 ($L/L_i=0.037$)	49
Figure 5 8 Velocity profiles for 1:6 RNG k- ϵ ($L/L_i=0.112-0.152$).....	50
Figure 5 9 Free surface elevation roller bucket, Experimental and CFD, scale and full scale, data	50
Figure 5 10 Flow depth relative differences along the roller bucket with experimental right wall as baseline data.....	51
Figure 5 11 Riverbed deformation and scour documentation after a test run for $Q=12000\text{ m}^3\text{s}^{-1}$ adapted from [31]	52
Figure 5 12 Free surface elevation on the roller bucket, for $Q=7000\text{ m}^3\text{s}^{-1}$	53
Figure 5 13 Pressure head development along the ramp of the roller bucket, comparison of CFD simulation with experimental data at pressure taps number 6, 7 and 8, with oscillation indication	54
Figure 5 14 Pressure head and flow depth along the ramp of the roller bucket.....	54
Figure 5 15 Pressure head differences compared to model values in %, ordered by pressure tap number.....	55
Figure 5 16 Pressure head and flow depth in the ogee crest region	56
Figure 5 17 Pressure distribution isometric colouring view at the crest in the 1:12 k- ϵ simulation, with gridlines	56
Figure B 1 Perpendicular step probes and their functions	B-1
Figure B 2 All line probe positions in the simulated area	B-1
Figure B 3 Pressure tap location overview [31].....	B-2
Figure B 4 Manually positioned pressure probes at the ogee crest (3D view).....	B-3
Figure B 5 Experimental free surface elevation on the right wall, for $Q=12000\text{ m}^3\text{s}^{-1}$	B-3
Figure B 6 Experimental free surface elevation on the left wall, for $Q=12000\text{ m}^3\text{s}^{-1}$	B-4
Figure B 7 Experimental free surface elevation on the right wall, for $Q=7000\text{ m}^3\text{s}^{-1}$	B-4
Figure C 1 Export options while saving Stereolithography file from inventor.....	C-1
Figure E 1 Rating curve of the Pedrógão dam spillway; designer computation, prototype and semiempirical formula, as well as physical model adapted from [31]	E-1
Figure E 2 Rating curve downstream of Pedrógão dam adapted from [31].....	E-1
Figure E 3 Original construction plans of Pedrógão [33]	E-2
Figure E 4 Original plans, showing the topography of the surrounding area of Pedrógão [33]	E-3
Figure E 5 Measuring the free surface elevation of the experimental study, utilizing AutoCAD Inventor.....	E-4
Figure G 1 Mass-averaged fluid mean kinetic energy for 1:3 RNG k- ϵ model scale ($Q=7000\text{ m}^3\text{s}^{-1}$)	G-1
Figure G 2 Mass-averaged turbulent dissipation for 1:3 RNG k- ϵ model scale ($Q= 7000\text{ m}^3\text{s}^{-1}$)	G-1
Figure G 3 Mass-averaged turbulent kinetic energy for 1:3 RNG k- ϵ model scale ($Q= 7000\text{ m}^3\text{s}^{-1}$)	G-1
Figure G 4 Mass-averaged fluid mean kinetic energy for 1:3 k- ϵ prototype scale ($Q= 12000\text{ m}^3\text{s}^{-1}$).....	G-2
Figure G 5 Mass-averaged turbulent dissipation for 1:3 k- ϵ prototype scale ($Q= 12000\text{ m}^3\text{s}^{-1}$)	G-2
Figure G 6 Mass-averaged turbulent kinetic energy for 1:3 k- ϵ prototype scale ($Q= 12000\text{ m}^3\text{s}^{-1}$)	G-2

.....	G-2
Figure G 7 Mass-averaged fluid mean kinetic energy for 1:3 RNG k- ϵ prototype scale (Q= $12000m^3s^{-1}$).....	G-2
Figure G 8 Mass-averaged turbulent dissipation for 1:3 RNG k- ϵ prototype scale (Q= $12000m^3s^{-1}$).....	G-3
Figure G 9 Mass-averaged turbulent kinetic energy for 1:3 RNG k- ϵ prototype scale (Q= $12000m^3s^{-1}$).....	G-3
Figure G 10 Mass-averaged fluid mean kinetic energy for 1:6 k- ϵ prototype scale (Q= $12000m^3s^{-1}$).....	G-3
Figure G 11 Mass-averaged turbulent dissipation for 1:6 k- ϵ prototype scale (Q= $12000m^3s^{-1}$).....	G-3
Figure G 12 Mass-averaged turbulent kinetic energy for 1:6 k- ϵ prototype scale (Q= $12000m^3s^{-1}$).....	G-4
Figure G 13 Mass-averaged fluid mean kinetic energy for 1:6 RNG k- ϵ model scale (Q= $12000m^3s^{-1}$).....	G-4
Figure G 14 Mass-averaged turbulent dissipation for 1:6 RNG k- ϵ model scale (Q= $12000m^3s^{-1}$).....	G-4
Figure G 15 Mass-averaged turbulent kinetic energy for 1:6 RNG k- ϵ model scale (Q= $12000m^3s^{-1}$).....	G-4
Figure G 16 Mass-averaged fluid mean kinetic energy for 1to12 k- ϵ prototype scale (Q= $12000m^3s^{-1}$).....	G-5
Figure G 17 Mass-averaged turbulent dissipation for 1:12 k- ϵ prototype scale (Q= $12000m^3s^{-1}$).....	G-5
Figure G 18 Mass-averaged turbulent kinetic energy for 1:12 k- ϵ prototype scale (Q= $12000m^3s^{-1}$).....	G-5
Figure I 1 Simulation overview of 1:6 k- ϵ at time 107 s, colour scaling with velocity.....	I-1
Figure I 2 Simulation overview of 1:6 k- ϵ at time 134 s, colour scaling with velocity.....	I-1
Figure I 3 Simulation overview of 1:6 k- ϵ at time 213 s, colour scaling with velocity.....	I-2
Figure I 4 Simulation overview of 1:6 k- ϵ at time 220 s, colour scaling with velocity.....	I-2

List of Tables

Table 4 1 Mesh cell sizes and total number of cells	29
Table 4 2 Mesh cell sizes and the total number of cells in the scale set ups	30
Table 4 3 Relative flow depth differences on the chute based on mesh size and turbulent model	37
Table 4 4 Flow depth relative differences in the roller bucket to the 1:12 k- ϵ mesh, based on mesh size and turbulence model	40
Table 4 5 velocity profile comparisons, avg. δ and maximum δ , in % and m s-1	43
Table 5 1 Flow depth average and maximum, relative differences to LNEC experimental results	48
Table 5 2 Flow depth in the roller bucket: avg. $\delta\%$ and max. $\delta\%$, compared with experimental results	51
Table 5 3 Flow depth relative differences in the roller bucket compared to experimental data, for $Q=7000 \text{ m}^3\text{s}^{-1}$	52
Table A-1 Flow depth on the chute overview by steps for the prototype scale mesh sizes and turbulent models	A-1
Table B-1 Coordinates of pressure taps	B-2
Table D-1 Individual mesh block data, mesh 1:3	D-1
Table D-2 Individual mesh block data, mesh 1:6	D-1
Table D-3 Individual mesh block data, mesh 1:12	D-2
Table D-4 Individual mesh block data, mesh 1:6 model scale simulation	D-2
Table D-5 Individual mesh block data, mesh 1:3 model scale simulation	D-2
Table F-1 Flow depth comparisons per step along the chute, LNEC experimental data as baseline	F-1
Table F-2 Flow depth comparisons per step along the chute, analytical data as baseline	F-2
Table F-3 Velocity average differences to simulation results 1:12 k- ϵ , per step	F-3

List of Acronyms

RCC	Roller compacted concrete
STL	Stereolithography file type
LNEC	Laboratório Nacional de Engenharia Civil
VOF	Volume of Fluid
CFD	Computational Fluid Dynamics
FAVOR	Fractional Area/Volume Obstacle Representation
TLEN	Turbulent mixing length

List of Symbols

γ	Isentropic exponent
δ	Boundary layer thickness
ϵ_T	Rate of turbulent energy dissipation
θ	Chute slope
μ	Kinematic viscosity
ξ_{cyl}	Cylindrical coordinate system transfer, cylindrical motion flag
τ_{suffix}	Stress tensor derivatives indicated by suffix
ρ	Density
A_{suffix}	Area at location indicated by the suffix
b_{suffix}	Porous media losses term at location indicated by the suffix
c_p, c_F	Inverse Turbulent Schmidt number
d	Flow depth
d_c	Critical flow depth
d_i	Flow depth at the point of inception
D_m	Molecular diffusivity of scalar in fluid
F^*	Roughness Froude number
F_{DIF}	Diffusion term
F_{SOR}	Generation of mass term
f_{suffix}	Viscous acceleration term at location indicated by suffix
G_T	Buoyancy production term

G_{suffix}	Body acceleration terms at location indicated by the suffix
g	Gravitational acceleration
h	Step height
H_0	Upstream total head
k	Macro-roughness
k_T	Turbulent kinetic energy
l	Step length
L	Length along the chute
L_i	Length along the chute until the point of interception
M	Molecular weight
N	Exponent of the velocity power law
P_T	Energy production term
p	Pressure
q_w	Unit discharge
R	Gas constant
R_{cyl}	Cylindrical coordinate system transfer, movement transformation multiplier
R_{DIF}	Turbulent diffusion term
R_{SOR}	Mass source term
Sc	Turbulent Schmidt number
T	Temperature
t	Time
$TLEN$	Turbulent mixing length
u	Velocity in x direction in cartesian coordinates

u_{max}	Free stream velocity
v	Velocity in y direction in cartesian coordinates
ν_p, ν_F	Diffusion coefficient
V_F	Volume of fluid
w	Velocity in z direction in cartesian coordinates
x	Coordinate in x direction in cartesian coordinates
y	Coordinate in y direction in cartesian coordinates
z_x	Vertical coordinate at suffix x coordinate
z	Coordinate in z direction in cartesian coordinates

List of Software

Flow 3D	CFD Simulation software by “Flow 3D®” version 11.2
FlowSight	Post processing software by “Flow 3D®” version 11.2
Excel	Spreadsheet software by “Microsoft” version 2016
Word	Text editing software by “Microsoft” version 2016
Acrobat Reader	PDF reading software by “Adobe” version 18.011.20058
Origin	Spreadsheet and graph creation software by “Origin” version 2018b
Team Viewer 13	Remote Control software by “Team Viewer” version 13.1.3629
Inventor	CAD software by “Autodesk” version professional 2018

Chapter 1

Introduction

1.1 Overview

Water is one of the most basic resources necessary for life. Due to global warming or better the concentration of extreme weather occurrences, the importance of storing large amounts of water becomes more and more important. With this increase in demand for water storage capabilities, the age-old technology of dams to store large amounts of water, sees an increase in use once again. A recent publication by Aquatic Sciences (Springer), made a case to show this strong increase in the construction of barrages/dams. These analyses of Zarfl et al. [1], at “University of Tübingen”, claims to know about at least 3700 new dam construction projects, which are planned or being designed at the moment and in the near future. Naturally, most of these projects will be small scale constructions. The increased use of small scale dam and water storage structures, will lead to an increase in the use of embankment dams. Relevant dam structures include necessarily a spillway, to be able to discharge excessive amounts of water. Spillways can feature a wide range of shapes. All designs are supposed

to reduce the energy content in the water. The energy present in the water needs to be reduced to protect the river bed and environment in the direct vicinity of the dam structure. If the dissipation of energy is not done properly, river bed erosion may occur, which can have a significant impact on the environment as well as on the structural integrity of the dam itself. The increase in new dams and dam rehabilitation will lead to an increase in overtopping spillways. For overtopping protection roller compacted concrete (RCC) surfaces are often used, due to its comparatively cheap cost. The RCC construction method utilizes individually compacted concrete granulate layers. The layer construction method facilitates the use of the stepped spillway concept. This stepped spillway design will be analysed in this report. The steps themselves are used to dissipate the kinetic energy of the flow. In their design guidelines for hydraulic dam structures [2], it is stated "...the kinetic energy dissipation potential may be reduced as flow depth (relative to the step size) increases (due to skimming flows). Also, consideration should be given to evaluating the cavitation potential." Hence, higher unit discharges reduce the effectiveness of stepped spillways and therefore need specific evaluation, whereas special consideration should be given to cavitation.

1.2 Objectives

This thesis compares computational fluid dynamics (CFD) simulations of a RCC dam, Pedrógão, in model scale and prototype scale with experimental results from laboratory testing of its physical model, as well as analytical and empirical predictions. These CFD simulations employ different mesh sizes and models to represent the flow conditions. The results will be compared and areas of attention on how to improve the accuracy of CFD simulations will be pointed out. Areas that will be focused on include:

- Flow depth representation along a non-aerated stepped spillway in high discharge scenarios.
- Flow depth representation in the roller bucket.
- Pressure head estimations at the crest and in the roller bucket.

1.3 Organization

This thesis is divided into six chapters. This chapter gives a brief introduction to the topic. Chapter two focuses on the experimental set up in the laboratory as well as the hydrodynamic baseline for stepped spillways, and its use for estimating the flow behaviour. Chapter three follows with explaining the basic concept of CFD simulation and the implementation in Flow 3D®, a commercially available CFD simulation software. Followed by the implemented governing equations and the numerical models/methods to solve these equations. Specific attention will be given to the turbulence models. The Chapter ends with specific Flow 3D® handling of boundaries and models to handle special cases like bubbles. The fourth chapter focuses on the actual executed work to implement the simulation environment and

the selected simulation parameters. FlowSight is the post processing software belonging to Flow 3D®, which is the CFD simulation software used for the simulations in this thesis. Both software packages are briefly discussed. The chapter goes on to explain the reasoning for the positioning of the probes used to show mesh convergence and used to compare different turbulence models. To conclude the mesh convergence of velocity profiles on the chute will be addressed. Results are shown in Chapter five and broken down into different areas of attention, flow depths on the chute and in the roller bucket reach, in model and prototype scale, as well as pressure heads at the crest and on the ramp of the roller bucket. Finally, chapter six discusses all results and their significance for future research. The thesis also contains nine appendixes where all supporting figures, documents, tables with CFD simulation results and screenshots are included.

Chapter 2

Literature review

2.1 Preliminary remarks

This section focuses on the general need for spillways, and a brief explanation to the concept of the spillway this report is based on. Also, different flow patterns are defined and explained in the later parts of this section. Using the knowledge of the flow patterns on stepped spillways, some methods for estimating the flow depths are presented.

2.2 Spillways

Dams for water storage are designed to restrict water flow. Every major dam needs an outlet for excess water, which is realized and designed with specific spillways, which serve the purpose of dissipating as much energy from the flow as possible. This is a very important safety measure to ensure the safe discharge of excess water. This is necessary in cases where the power generating discharge is not able to keep the stored water level at safe condition. Such a situation might occur in the case of maintenance, damage in the power generation system or in case of natural floods. The spillways are important for a multitude of safety reasons. If the water would be discharged unguided, with all its energy, the flow could erode the riverbed rapidly. In what ways would be unpredictable upfront. This unpredictable erosion could have strong repercussions for inhabitants in the area, human and nonhuman, as well as erode the structural integrity of the whole dam. For these reasons the discharge needs to be guided and the energy levels need to be lowered to a sufficiently level to be handled by the environment. Spillways can have many different shapes and can have different approaches as to how the energy is dissipated. The rise of RCC constructed surfaces promotes naturally the use of stepped spillways [3].

2.3 Stepped spillway concept

The stepped spillway, in general, is the concept of breaking the full-scale vertical fall into multiple smaller sections. The resulting geometry resembles steps, where the name of this chute design is given. A common example is shown in Figure 2-1.



Figure 2-1 Stepped overflow spillway, Melton dam in Australia [4]

Stepped spillways have a very specific set of flow behaviours which have been the scope of research over the last 20 years [5] [6] [7] [8]. This report will specifically focus on Pedrógão stepped spillway and its terminal structure, a roller bucket design.

2.3.1 Stepped spillway flow conditions

Stepped spillways develop very specific and distinguished flow conditions and patterns. As main influence on the flow pattern are unit discharge, spillway slope and step height. For a given channel slope and step height, with increasing flow rate the flow regime evolves from nappe, then transition, and finally skimming flow [5]. For a strongly developed nappe flow the step length needs to be higher than flow depth [9]. Skimming flow is defined by fully submerged steps and eventually a fully aerated flow in the downstream region [10].

2.3.2 Nappe flow

Nappe flow is defined as series of small individual free-falling sections. These small falls can create individual hydraulic jumps and dissipate the energy through different hydraulic behaviours, such as, jet break up, jet mixing, and the potential hydraulic jump. A general schematic of a nappe flow region is shown in Figure 2-2. Individual steps can be calculated as regular waterflow drops with hydraulic jumps [11].

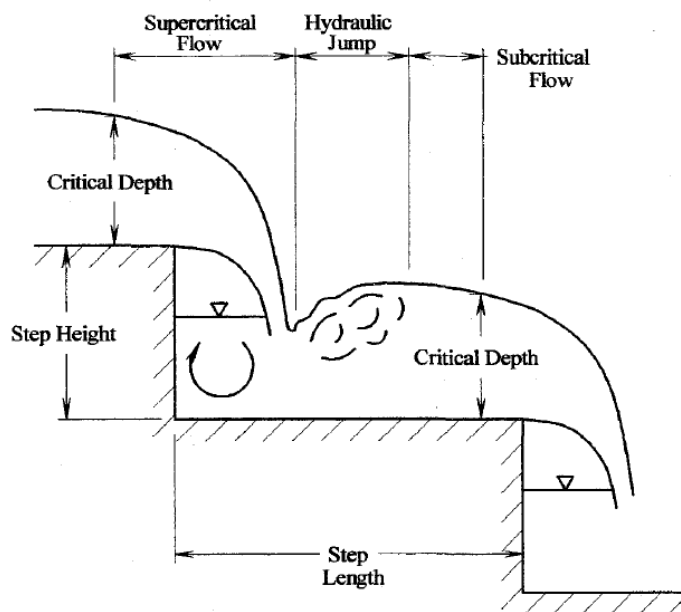


Figure 2-2 Nappe flow schematic [3]

For such a flow to be present the discharge values need to be relatively low. An upper limit to be considered nappe flow was proposed by [12] as

$$\frac{d_c}{h} = 0.89 - 0.4 \left(\frac{h}{l} \right) \quad 2.1$$

for $0.05 \leq h/l \leq 1.7$, where h = step height, l = step length and d_c = critical flow depth which is calculated by

$$d_c = \sqrt[3]{\frac{q_w^2}{g}} \quad 2.2$$

with q_w = unit discharge and g = gravitational acceleration.

A continuous nappe flow is able to dissipate more energy than a skimming flow set up [13] [14]. Due to the necessity of low unit discharge values and small slope, construction costs are generally larger, compared to a chute designed for skimming flow set up [15].

2.3.3 Skimming flow

With the steps fully submerged in skimming flow the resulting free surface resemble the free surface of a common open channel flow. The steps of the chute form, on a hydrodynamic standpoint, a bottom with large macro roughness [11]. Gonzalez and Chanson [16] derived an analogy between stepped spillways and the occurrence of cavities in open channel flow. This theoretical bottom is called pseudo-bottom and is formed from step tip to step tip. Commonly a skimming flow is separated in four regions: clear water region, partially aerated flow region, fully aerated region and uniform flow region [5].

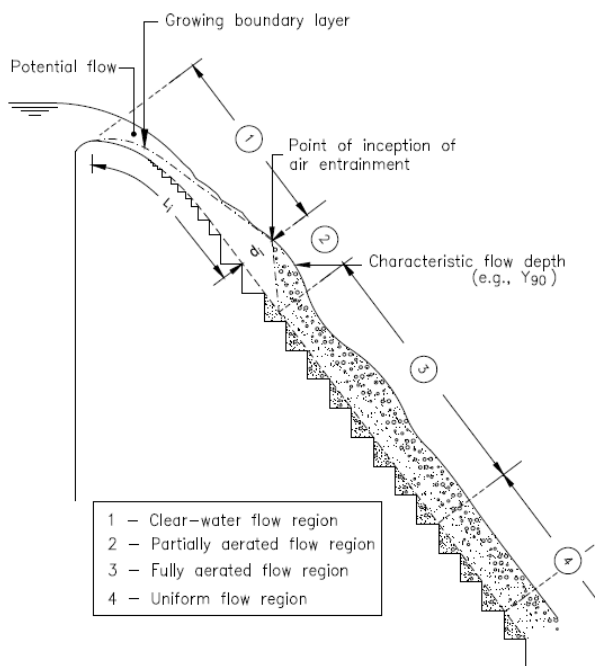


Figure 2-3 Skimming flow region definitions [5]

The transition between the non-aerated region and partially aerated flow regions, where the boundary layer reaches the free surface, is called the inception point. The inception point is the point where the boundary layer reaches the free surface. The prediction of this point has been subject of many studies and researched extensively in the past, e.g. [17] [18]. The chute studied in this report is too short to reach the inception point for the analysed discharge values. This study will therefore focus on the non-aerated region. As mentioned before, the flow in the non-aerated region has strong similarities with

common open channel flow [16]. Therein, free-stream velocity, may be calculated by equation 2.3 [19]. It represents the maximum achievable velocity by the flow at a given cross-section

$$u_{max} = \sqrt{2g(H_0 - z_0 - d \cos \theta)} \tag{2.3}$$

with u_{max} = free-stream velocity, g = gravitational acceleration, H_0 = upstream total head, z_0 = vertical coordinate along the pseudo-bottom, d = flow depth and θ = channel slope.

The lower section of the velocity profile is a representation of the boundary layer [20]. In the case of the stepped spillway, additionally to the smooth bottom of the flow are the interaction with the step cavities and their circulation flow pattern [21].

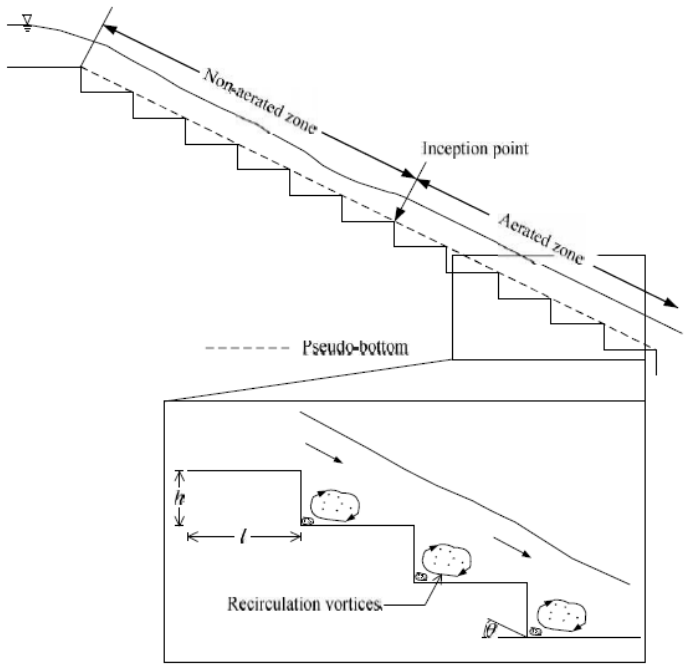


Figure 2-4 Sketch of the skimming flow regime, on a spillway with moderate slope [21]

The additional interaction between these macro-roughnesses, its turbulent eddies and the flow above the pseudo-bottom, create a unique boundary layer development for each stepped spillway. The boundary layer concept divides high Reynolds number flows, such as stepped spillway flow, into two regions, considering a cross-section of the flow. In the non-boundary layer region, viscous forces are not considered to be dominant and flow can be estimated as described in equation 2.3. The second region is the boundary layer at the wall where the viscosity forces are a dominant contributor [22]. In chute arrangements, stepped or smooth bottoms, the boundary layer increases its thickness in function of L , length of the chute. The prediction of this thickness is still a research topic up till today, due to the high impact of surface roughness, slope, discharge and more factors [19] [18]. The thickness of boundary layers is commonly expressed by δ . The increasing thickness of the boundary layer along the chute is a very important parameter, since it is the essential part to the inception point. Proposed calculation equations are,

$$\frac{\delta}{L} = 0.112 * \left(\frac{L}{k}\right)^{-0.309} \quad [18] \quad 2.4$$

$$\frac{\delta}{L} = 0.114 * \left(\frac{L}{k}\right)^{-0.311} \quad [19] \quad 2.5$$

with L = length along the chute and $k = h \cos\theta$. This study will use equation 2.5 to proceed further, due to its wider application range; equation 2.4 was proposed for a range of $15 < L/k < 25$ [18] whereas equation 2.5 is applicable in the range of $10 < L/k < 140$ and specifically more optimised for an ogee crest [19], which is the studied crest type.

2.4 Flow depth along the chute

2.4.1 Analytical method

The flow on the chute of a stepped spillway has a developing boundary layer, as previously discussed. The non-boundary layer region theoretically assumes free stream velocity, u_{max} , which is calculated by equation 2.3, as discussed in section 2.3.3. Based on the continuity equation and the velocity distribution in the developing flow region, the flow depth, d , can be calculated from [17] [19]

$$q_w = u_{max} * \left(d - \frac{\delta}{N + 1}\right) \quad 2.6$$

with $N = 3.4$ the exponent of the power law velocity distribution within the boundary layer (e.g. [19]). This is an empirical value, determined for specific hydraulic arrangements. In this case a value for steep stepped spillways was proposed by Meireles et al. [19], which is close to the $N=3.0$ empirical value of Amador et al. [18]. Considering δ given by equation 2.5, the combination of equations 2.6 and 2.3 form an iteration loop, providing a flow depth prediction for a given distance along the chute. Further analyses will be based on the N value of Meireles et al. [19].

2.4.2 Empirical formulae

Meireles et al. [19] analysed a multitude of data sources to create equations for empirical clear water depth predictions. The empirical prediction for the length coordinate of the inception point, L_i , and an empirical solution for the flow depth at the inception point, d_i , equations 2.7 and 2.8, are combined with equation 2.10 [19].

$$\frac{L_i}{k} = 6.75F_*^{0.76} \quad 2.7$$

$$\frac{d_i}{k} = 0.35F_*^{0.59} \quad 2.8$$

with, $k = h \cos\theta$, θ being the chute slope. Equations 2.7 and 2.8 are shown in Figure 2-5 by Meireles, et al. [19], with F_* the roughness Froude number calculated by

$$F_* = q_w / \sqrt{g \sin(\theta) k^3} \quad 2.9$$

where, q_w is the unit discharge and g the gravitational acceleration.

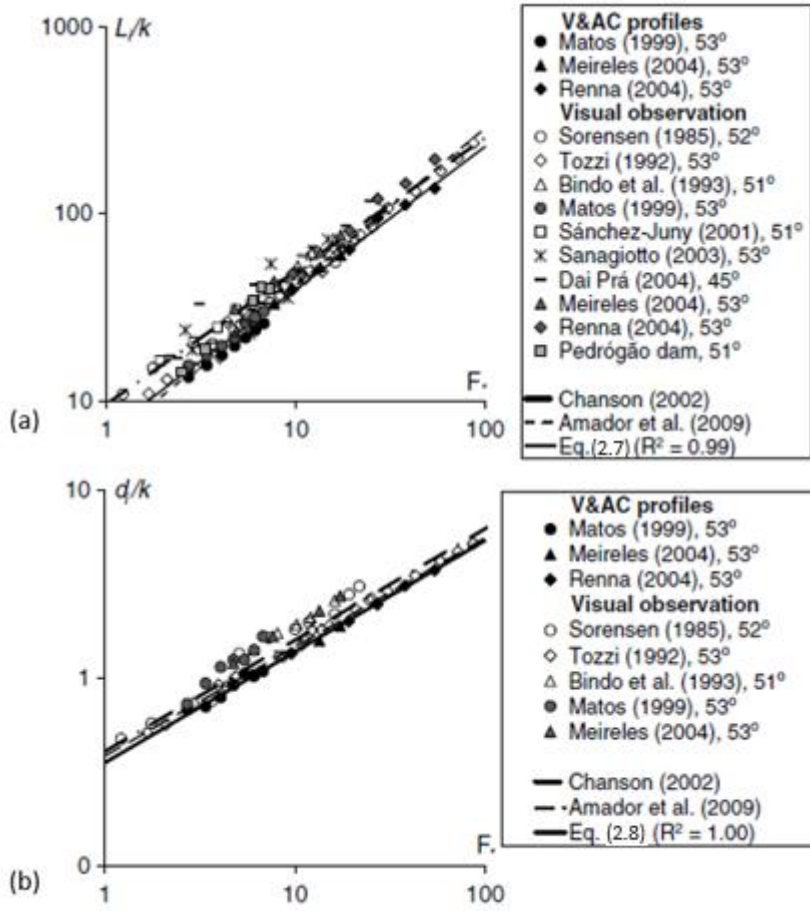


Figure 2-5 Flow properties at the inception point: (a) location; (b) equivalent clear water depth (adapted from [19])

$$\frac{d}{d_i} = 1.17 - 0.25 \frac{L}{L_i} + \frac{0.084}{L/L_i} \quad 2.10$$

Equation 2.10 is only valid in the region of $0.1 \leq L/L_i \leq 1$ and for $0.4 \leq d_c/h \leq 19.3$ [19]. The critical flow depth is referred to as d_c and is calculated by equation 2.2. Applying equation 2.2 to the case of Pedrógão dam gives $d_c/h = \sqrt[3]{q_w^2/g}/h = 9.1$ and is therefore in the applicable range for the empirical flow depth prediction method of Meireles et al. [19], provided in the correct L/L_i region. Equation 2.10

is plotted in Figure 2-6 presented by Meireles et al. [19]. The figures show the very good agreement in the larger L/L_i region and more deviation in the lower L/L_i region, which is significant considering that the flow on Pedrógão dam spillway only reaches a L/L_i of 0.25, for the design discharge.

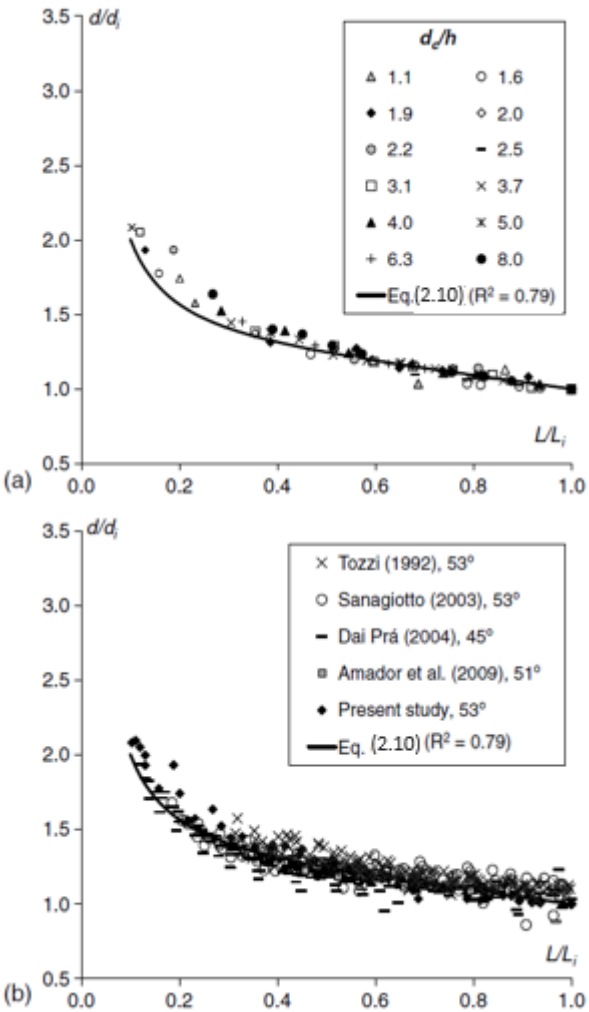


Figure 2-6 Evolution of the normalized equivalent clear-water depth in the non-aerated region: (a) comparison among equation 2.10 and experimental data from the study undertaken at LNEC; (b) comparison among equation 2.10 and experimental data from several studies for similar slope (adapted from [19])

Chapter 3

Mathematical and numerical models

3.1 Preliminary remarks

This section will focus on the explanation of basic CFD simulation concept and its implementation in Flow 3D[®] with solvers and the turbulence models $k-\epsilon$ and RNG $k-\epsilon$, as well as different boundary conditions and additional provided models.

3.2 Numerical environment

The used software Flow 3D[®] is based on a typical approach to subdivide the physical model into a grid like mesh structure to create many small volumes. Any of these small volumes has surfaces and the volume itself as theoretical storage and interaction locations for the parameters, which are part of the calculation. Parameters might be values such as pressure, temperature or velocity. These artificial volumes are typically rectangular or cube like volumes. An example is shown in Figure 3-1, it also shows the location of the individual values. All values in the centre of the volume are averages over the whole volume and the wall parameters are A as the area and the velocity vectors, w , v and u .

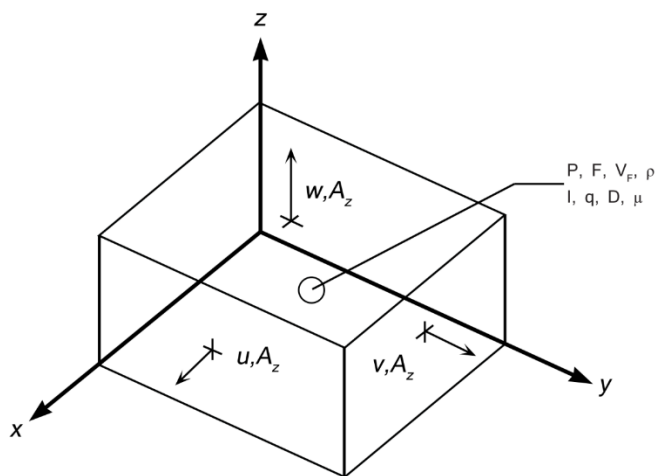


Figure 3-1 Example cell in a Flow 3D[®] CFD mesh, with all values and their locations [23]

As common for programmes all surfaces and volumes are numbered with regular indices, but all instances have their own unique “address” (i,j,k) . These indices will appear in later equations to symbolize neighbouring cell by:

“NF $i,j,k = 0$ full or obstacle cell
= 1 surface ($i-1$ inward neighbour)
= 2 surface ($i+1$ inward neighbour)
= 3 surface ($j-1$ inward neighbour)
= 4 surface ($j+1$ inward neighbour)
= 5 surface ($k-1$ inward neighbour)
= 6 surface ($k+1$ inward neighbour)” [23]

All physical phenomena, laws, behaviours have to be represented in this volumetric discrete mesh. To implement reality like behaviour, many mathematical connections and models have to be used and obeyed [23].

3.3 Governing equations and models

3.3.1 Mass continuity equation

The conservation of mass or transferred mass continuity has to be fulfilled at all times. Therefore it is one of the most important equations in CFD calculations and “mass lost“ is commonly a measure to break simulations prematurely since they are obviously faulty. Flow 3D® implementation of the mass continuity equation is [23]

$$V_F \frac{\partial \rho}{\partial t} + \frac{\partial}{\partial x} (\rho u A_x) + R_{cyl} \frac{\partial}{\partial y} (\rho v A_y) + \frac{\partial}{\partial z} (\rho w A_z) + \xi_{cyl} \frac{\rho u A_x}{x} = R_{DIF} + R_{SOR} \quad 3.1$$

where V_F is the volume, ρ the density, R_{DIF} is a turbulent diffusion term and R_{SOR} a mass source. As shown in the previous section, u , v and w are the velocities in x , y and z directions, as well as the respective areas, A_x , A_y and A_z . R_{cyl} is a multiplier used for conversion between cartesian and cylindrical coordinate systems ($R_{cyl} = r_m/r$; r_m =reference radius; r =radius at calculation point) and therefore is set to 1 in the case of using a cartesian coordinate system. The term $\xi_{cyl} \frac{\rho u A_x}{x}$ is representing cylindrical motion and is part of the conversion process from cartesian coordinates to cylindrical coordinates. In the following equations this term will be neglected together with the R_{cyl} constant [23]. The individual left-hand side terms of equation 3.1 can be summarized as mass fraction differential through the surfaces and change in density. The turbulent diffusion term is implemented as, (adapted from Flow 3D, 2012)

$$R_{DIF} = \frac{\partial}{\partial x} \left(v_p A_x \frac{\partial \rho}{\partial x} \right) + \frac{\partial}{\partial y} \left(v_p A_y \frac{\partial \rho}{\partial y} \right) + \frac{\partial}{\partial z} \left(v_p A_z \frac{\partial \rho}{\partial z} \right) \quad 3.2$$

with $v_p = c_p \mu / \rho$ in which μ the kinematic viscosity and c_p is a constant being $= 1/Sc$ with Sc being the turbulent Schmidt number. The Schmidt number has been subject of dedicated studies and is generally calculated as [24]

$$Sc = \frac{\mu}{D_m} \quad 3.3$$

where, μ is the kinematic viscosity and D_m the molecular diffusivity of the fluid. The turbulent diffusion equation (3.2) needs a non-uniform density to be useful, which excludes water only simulations but includes water with air entrainment calculations. The other term, R_{SOR} , is a density source term which is needed for mass injection for example through porous obstacle surfaces [23]. Since there will be no mass injection in the present study, this term can be neglected and will be neglected in all following equations.

3.3.2 Momentum conservation equations

There are three different fluid velocity components, u , v and w , as mentioned earlier. These velocity components have to follow the Navier-Stokes equations, where Flow 3D[®] has added some additional terms to incorporate special scenarios, for example, porous media or injection of extra mass adapted [23]

$$\frac{\partial u}{\partial t} + \frac{1}{V_f} \left\{ u A_x \frac{\partial u}{\partial x} + v A_y \frac{\partial u}{\partial y} + w A_z \frac{\partial u}{\partial z} \right\} = -\frac{1}{\rho} \frac{\partial p}{\partial x} + G_x + f_x - b_x \quad 3.4$$

$$\frac{\partial v}{\partial t} + \frac{1}{V_f} \left\{ u A_x \frac{\partial v}{\partial x} + v A_y \frac{\partial v}{\partial y} + w A_z \frac{\partial v}{\partial z} \right\} + \xi \frac{A_y u v}{x V_F} = -\frac{1}{\rho} \left(\frac{\partial p}{\partial y} \right) + G_y + f_y - b_y \quad 3.5$$

$$\frac{\partial w}{\partial t} + \frac{1}{V_f} \left\{ u A_x \frac{\partial w}{\partial x} + v A_y \frac{\partial w}{\partial y} + w A_z \frac{\partial w}{\partial z} \right\} = -\frac{1}{\rho} \frac{\partial p}{\partial z} + G_z + f_z - b_z \quad 3.6$$

Here G_x , G_y and G_z are body acceleration terms, which represent physical moving parts that influence the fluid and can therefore be neglected [23]. The variables b_x , b_y and b_z are flow losses in porous media and therefore can also be neglected, as well as the previously explained R_{SOR} terms f_x , f_y and f_z . are viscous accelerations and need to be calculated when fluid might change viscosity, which is clearly the case, in a highly turbulent water flow, (adapted from [23])

$$\rho V_F f_x = w s x - \left\{ \frac{\partial}{\partial x} (A_x \tau_{xx}) + \frac{\partial}{\partial y} (A_y \tau_{xy}) + \frac{\partial}{\partial z} (A_z \tau_{xz}) \right\} \quad 3.7$$

$$\rho V_F f_y = w s y - \left\{ \frac{\partial}{\partial x} (A_x \tau_{xy}) + \frac{\partial}{\partial y} (A_y \tau_{yy}) + \frac{\partial}{\partial z} (A_z \tau_{yz}) \right\} \quad 3.8$$

$$\rho V_F f_z = w s z - \left\{ \frac{\partial}{\partial x} (A_x \tau_{xz}) + \frac{\partial}{\partial y} (A_y \tau_{yz}) + \frac{\partial}{\partial z} (A_z \tau_{zz}) \right\} \quad 3.9$$

where:

$$\tau_{xx} = -2\mu \left\{ \frac{\partial u}{\partial x} - \frac{1}{3} \left(\frac{\partial u}{\partial x} + \frac{\partial v}{\partial y} + \frac{\partial w}{\partial z} \right) \right\} \quad 3.10$$

$$\tau_{yy} = -2\mu \left\{ R \frac{\partial v}{\partial y} + \xi \frac{u}{x} - \frac{1}{3} \left(\frac{\partial u}{\partial x} + \frac{\partial v}{\partial y} + \frac{\partial w}{\partial z} \right) \right\} \quad 3.11$$

$$\tau_{zz} = -2\mu \left\{ \frac{\partial w}{\partial z} - \frac{1}{3} \left(\frac{\partial u}{\partial x} + \frac{\partial v}{\partial y} + \frac{\partial w}{\partial z} \right) \right\} \quad 3.12$$

$$\tau_{xy} = -\mu \left\{ \frac{\partial v}{\partial x} + \frac{\partial u}{\partial y} \right\} \quad 3.13$$

$$\tau_{xz} = -2 \left\{ \frac{\partial u}{\partial z} + \frac{\partial w}{\partial x} \right\} \quad 3.14$$

$$\tau_{yz} = -2 \left\{ \frac{\partial v}{\partial z} + \frac{\partial w}{\partial y} \right\} \quad 3.15$$

3.3.3 Volume of fluid model (VOF)

Flow 3D[®] uses an adapted version of the VOF method, developed by Hirt and Nichols [25] for its free surface calculations and other optimisations [26]. VOF is a specialized procedure to handle computational cells with surfaces between fluids, void and fluid as well as environment and fluid. The original VOF consist of three individual steps of solver. A first “Explicit approximation”, second satisfactions of continuity equation and thirdly generation of a suitable function for the free surface inside of the single control volumes to house the fluid fraction F [25]. The “Explicit approximation” a linear extrapolation for “F” fluid fraction surface is calculated, together with the fluid fraction itself, which ranges from 1 to 0 (completely filled to empty cell). Secondly in a donor-acceptor relation between neighbouring cells the governing transport equation is being iterated. Individually this is expressed in the mandatory fulfilment of equation 3.16. The fluid fraction and the different interfaces between cells are then used to create a normalised surface through the cell to which then a boundary condition is applied, [23].

Flow 3D[®] implements equation 3.4 as follows (adapted from [23])

$$\frac{\partial F}{\partial t} + \frac{1}{V_f} \left[\frac{\partial}{\partial x} (FA_x u) + \frac{\partial}{\partial y} (FA_y v) + \frac{\partial}{\partial z} (FA_z w) \right] = F_{DIF} \quad 3.16$$

For a two fluid scenario a specific equation is used (adapted from [23])

$$F_{DIF} = \frac{1}{V_f} \left\{ \frac{\partial}{\partial x} \left(v_f A_x \frac{\partial F}{\partial x} \right) + \frac{\partial}{\partial y} \left(v_f A_y \frac{\partial F}{\partial y} \right) + \frac{\partial}{\partial z} \left(v_f A_z \frac{\partial F}{\partial z} \right) \right\} \quad 3.17$$

The diffusion coefficient is defined as $v_f = c_f \mu / \rho$ where c_f is a often referred to as the invert turbulent Schmidt number.

3.4 Turbulence models

The high energetic flow state of turbulent flow and its self-created large and small eddies need a specific evaluation method. This energetic state is measured as a turbulent kinetic energy value per unit mass, k_T . This turbulent energy has its own transport equation to represent the turbulent velocity fluctuations [23]

$$k_T = \frac{1}{2} (\overline{u'^2} + \overline{v'^2} + \overline{w'^2}) \quad 3.18$$

where, u' , v' and w' are the -x, -y and -z components of the fluid velocity. These are meant to represent the turbulent flow variations. This is implemented in Flow 3D® as [23]

$$\frac{\partial k_t}{\partial t} + \frac{1}{V_F} \left\{ u A_x \frac{\partial k_T}{\partial x} + v A_y \frac{\partial k_T}{\partial y} + w A_z \frac{\partial k_T}{\partial z} \right\} = P_T + G_T + Diff_{k_T} - \epsilon_T \quad 3.19$$

with, V_F, A_x, A_y, A_z as FAVOR created functions. The Flow 3D® specific representing variables ($P_T, G_T, Diff_{k_T}, \epsilon_T$) will explained in the following. P_T is the kinetic energy production term including all available parameters to the simulation, given as (adapted from [23])

$$\begin{aligned} P_T = CSPRO \left(\frac{\mu}{\rho V_F} \right) & \left\{ 2A_x \left(\frac{\partial u}{\partial x} \right)^2 + 2A_y \left(\frac{\partial v}{\partial y} \right)^2 + 2A_z \left(\frac{\partial w}{\partial z} \right)^2 \right. \\ & + \left(\frac{\partial v}{\partial x} + \frac{\partial u}{\partial y} \right) \left[A_x \frac{\partial v}{\partial x} + A_y \left(\frac{\partial u}{\partial y} \right) \right] + \left(\frac{\partial u}{\partial z} + \frac{\partial w}{\partial x} \right) \left(A_z \frac{\partial u}{\partial z} + A_x \frac{\partial w}{\partial x} \right) \\ & \left. + \left(\frac{\partial v}{\partial z} + \frac{\partial w}{\partial y} \right) \left(A_z \frac{\partial v}{\partial z} + A_y \frac{\partial w}{\partial y} \right) \right\} \end{aligned} \quad 3.20$$

where, CSPRO is a turbulence representing parameter with the default value of 1.0. G_T is the buoyancy production term which is formulated on the following way (adapted from [23])

$$G_T = -CRHO \left(\frac{\mu}{\rho^3} \right) \left(\frac{\partial \rho}{\partial x} \frac{\partial p}{\partial x} + \frac{\partial \rho}{\partial y} \frac{\partial p}{\partial y} + \frac{\partial \rho}{\partial z} \frac{\partial p}{\partial z} \right) \quad 3.21$$

where μ the fluid inherent molecular dynamic viscosity, ρ the fluid density, p the pressure and CRHO another turbulence representing parameter specific to Flow 3D®. Lastly the kinetic turbulent diffusion term is given as (adapted from [23])

$$Diff_{k_T} = \frac{1}{V_F} \left\{ \frac{\partial}{\partial x} \left(u_k A_x \frac{\partial k_T}{\partial x} \right) + \frac{\partial}{\partial y} \left(u_k A_y \frac{\partial k_T}{\partial y} \right) + \frac{\partial}{\partial z} \left(u_k A_z \frac{\partial k_T}{\partial z} \right) \right\} \quad 3.22$$

with, u_k being the diffusion coefficient of k_T and is individually calculated depending on flow state and therefore turbulent viscosity at the specific spot and time [23]; ϵ_T the rate of turbulent energy dissipation is calculated in the basic model, called one equation model,

related to the overall turbulent energy as [23]

$$\epsilon_T = CNU \sqrt{\frac{3}{2} \frac{k_T^{3/2}}{TLEN}} \quad 3.23$$

where CNU is a Flow 3D[®] specific parameter set to 0.09, to be able to mitigate the influence of this term, TLEN is the turbulent mixing length scale which is by default 7% of the smallest domain dimension and is recommended to be 7% of the smallest hydraulic parameter [27]. As adaptation to this model and seen as more sophisticated are the $k - \epsilon$ model and the *RNG* $k - \epsilon$ model.

3.4.1 $k - \epsilon$ model

The $k - \epsilon$ model was developed by Harlow and Welch [28] and later by Launder and Spalding [29] under the assumption that the flow is fully turbulent, and the effects of molecular viscosity are negligible. The model uses an additional transport equation to solve for the turbulent energy dissipation ϵ_T and therefore replaces equation 3.23 [23]

$$\frac{\partial \epsilon_T}{\partial t} + \frac{1}{V_F} \left\{ u A_x \frac{\partial \epsilon_T}{\partial x} + v A_y \frac{\partial \epsilon_T}{\partial y} + w A_z \frac{\partial \epsilon_T}{\partial z} \right\} = \frac{CDIS1 * \epsilon_T}{k_T} (P_T + CDIS3 * G_T) + Diff_{f_\epsilon} - CDIS2 \frac{\epsilon_T^2}{k_T} \quad 3.24$$

where the default values of the model constants, *CDIS1* (1.44), *CDIS2*(1.92) and *CDIS3* (0.2) have been determined from experiments with air and water for the fundamental turbulent shear flows, including homogeneous shear flows and decaying isotropic grid turbulence. They have been found to work fairly well for a wide range of applications [30]. The replacement of the original ϵ_T equation makes the selection of a TLEN value obsolete. The diffusion of dissipation is implemented as (adapted from [23])

$$Diff_{f_\epsilon} = \frac{1}{V_F} \left\{ \frac{\partial}{\partial x} \left(u_\epsilon A_x \frac{\partial \epsilon_T}{\partial x} + \frac{\partial}{\partial y} \left(u_\epsilon A_y R \frac{\partial \epsilon_T}{\partial y} \right) + \frac{\partial}{\partial z} \left(u_\epsilon A_z \frac{\partial \epsilon_T}{\partial z} \right) \right) \right\} \quad 3.25$$

3.4.2 *RNG* $k - \epsilon$ model

As further development of the $k - \epsilon$ model was the *RNG*, Renormalization-Group, model developed by [31] and [32]. The default values of *RMTKE*, *CDIS1* and *CNU* are different than those used in the $k - \epsilon$ model; they are 1.39, 1.42 and 0.085, respectively. *CDIS2* is computed from the turbulent kinetic energy (k_T) and turbulent production (P_T) term (equations 3.19 and 3.20).

3.4.3 General remarks

In all turbulence transport models, the kinematic turbulent viscosity ν_T is computed from [23]

$$\nu_T = CNU \frac{k_T^2}{\epsilon_T} \quad 3.26$$

The important parameter TLEN used in the one equation model and in $k - \epsilon$ and its successor RNG $k - \epsilon$ has been replaced by dynamic adaptation employing equations 3.19 and 3.20. In the RNG $k - \epsilon$ model implementation of Flow 3D[®], TLEN is still used to give ϵ_T numerical limits. This was implemented to prevent numerical issues in very low turbulent dissipating regions, ϵ_T could assume near zero values, resulting in instability in the calculation of 3.26. To prevent these occurrences the lower limit using the TLEN parameter and calculated by equation 3.27 was implemented [23]

$$\epsilon_{T,min} = CNU \sqrt{\frac{3}{2} \frac{k_T^{3/2}}{TLEN}} \quad 3.27$$

3.5 Finite difference solution method

The general solver methodology of Flow 3D[®] is called “Finite Difference Solution Method”. It is a similar approach in a donor acceptor iteration model used in the VOF method. There are three steps to the method [23];

1. Explicit approximations of the momentum equations 3.4, 3.5 and 3.6, based on the values of the previous time step values.
2. Satisfying the continuity equations and iteratively adjusting for all cells relations. These iterations are especially important due to the balancing of relations between all 6 neighbouring cells.
3. Fluid surfaces are being updated in similar iteration processes as well as diffusive processes, temperature transport and the turbulence quantities.

All three steps might be iterated if stability criteria are not met and time step has to be reduced. The described procedure is called the “first order procedure”, Flow 3D[®] offers a second order solver. The second order solution adds an extra iteration after the first step the approximation with values of current time step. The next iteration will use the new time step values, which are then used to create averages between the two time steps to create a evaluable time step of “ $t + \frac{1}{2}$ ”, additionally to “ t ” and “ $t + 1$ ”.

3.6 Flow 3D boundary conditions

As discussed in section 3.2 the CFD simulation is based on a grid like mesh structure. The limits of these meshes, in the cartesian digital environment, are called boundaries. A mesh block has 6 boundaries, x_{min} , x_{max} , y_{min} , y_{max} , z_{min} and z_{max} . these boundaries get assigned different conditions. A condition defines the behaviour and interaction of such a “border” with the simulated fluids [23].

3.6.1 Free-slip boundary

This boundary is used as a general rule for all rigid and free boundary surfaces, for example physical obstacles. The condition requires to have zero tangential stresses, this is imposed by setting all velocity derivatives on the specific cell surface to zero. If needed Flow 3D® gives the option to allow wall stresses for specific scenarios such as rotating mixing containers or similar scenarios [23].

3.6.2 Fixed pressure/velocity boundary

This boundary creates an extra layer of cells outside of the mesh. These cells are being assigned constant values, these values influence then cells next to them in the simulation area by imposing fixed pressure values onto them without reducing the simulation environment. Hereby is to consider that the values given will be located half a cell away from the actual boundary, which might have to be considered if velocity direction, temperature or other distance/direction relying conditions is being imposed. Cases like specific surface elevation, are filled with water, combined with an appropriate pressure gradient over the height and is kept constant in the additionally generated boundary cells [23].

3.6.3 Time dependent boundary

These boundaries act the same as the fixed boundary conditions, the only major difference is they are based on tables which specify the desired values for a given time. Functions need to be broken down into an appropriately small step size and feed in table form to the boundary condition in Flow 3D® [23].

3.6.4 Outflow boundary

This boundary lets a flow vanish in its cell. Supposedly this boundary condition should let a flow pass to outside the simulation area without any impact on the upstream flow. This creates issues in the donor acceptor relationship between all cells in the simulation. The flow values are deleted after the successful calculation of the transport equation, not after each pass through the pressure iteration. The not deletion of the value between every iteration is mitigating the influence of the boundary on the upstream flow. Flow 3D® itself advises to use this boundary with caution since in most cases this boundary has an influence on upstream behaviour [23].

3.7 Flow 3D specialized bubble tracking

The “void” regions determined by the VOF method, or nul fluid fractions regions are in most cases the gases above the fluid fraction, but they can be bubbles enclosed by fluid or fluid and structure. The default handling of these bubbles treats them as regions with uniform pressure void region. The VOF handling processes then treats the surface of the bubble as pressure boundary condition, which is an excellent approximation in most scenarios. The inclusion in the VOF method, enables density changes and therefore buoyancy effects to be simulated [23].

3.7.1 Adiabatic bubbles

Specific attention can be given to the fact that if there is no source of energy or heat, the bubble acts as an adiabatic bubble and will change pressure on the basis of [23]

$$p = p_0 \left(\frac{V_0}{V} \right)^\gamma \quad 3.28$$

in this case, p and V are the new pressure and volume values which makes p_0 and V_0 the original pressure and volume values, with, $\gamma = C_p/C_v$ the isentropic exponent where C_p is the specific heat at constant pressure and C_v is the specific heat at constant volume.

3.7.2 Variable pressure void bubble

In case of fluid enclosed void regions which experience a change in pressure, this has to be taken into consideration, for example rising air bubbles in a water environment. Flow 3D® simplifies the pressure change inside such bubbles by assuming perfect gas, reversible, adiabatic changes, therefore the isentropic pressure relation

$$\frac{p_1}{p_2} = \left(\frac{\rho_2}{\rho_1} \right)^\gamma \quad 3.29$$

with, $\gamma = C_p/C_v$ as described in previous section. Such bubbles may coalesce or break up, which are behaviours processed by the default bubble pressure model. Combination of two bubble volumes create a new combined volume with a new pressure, the breaking up process is more complex. The model simulates newly created smaller bubbles at the previous pressures. This is a rough assumption made by Flow 3D®, with low influence on the overall simulation estimated by Flow 3D® [23].

3.7.3 Buoyant flow due to bubbles

Buoyancy forces are a result of density change, commonly the density is evaluated with the temperature. The buoyancy model incorporates bubbles or a secondary fluid in the density evaluation. The implemented equation is [23].

$$\rho = F\rho_{1(T)} + (1 - F)\rho_{2(T)} \quad 3.30$$

where both ρ are functions and F is the fluid fraction determined by equation 3.16

$$\rho_{(T)} = RHOF[1 - THEXF(T - T^*)] \quad 3.31$$

with, T^* being the reference temperature, THEXF is the thermal expansion coefficient and RHOF the reference density. This newly evaluated density will create pressure gradients at appropriate locations.

3.8 Mesh generation and “FAVOR” algorithm

The mesh generation in the software Flow 3D® is a strongly automated process. Flow 3D® employs an algorithm, “FAVOR”. This algorithm first determines if mesh edges and corners represent inside or outside of the generated subcomponents. This is done in three steps [23]:

- If all four corners of a cell face are inside the subcomponent, then the entire face is defined to be within the subcomponent.
- Similarly, if all corners lie outside, then the entire face is assumed to be outside the subcomponent.
- When some face corners are inside a subcomponent and some are outside, the area fraction generator computes the intersection of the subcomponent with the face edges. Area fractions are then computed from these intersection points assuming straight-line connections between intersection points within the face. The straight-line assumption introduces a small error in the fractional area when the subcomponent boundary is curved inside the cell. The approximation improves as the grid resolution is refined.

The result of this is that solids with no intersecting corners of the mesh are being neglected. This is shown in Figure 3-2. On the left is an example structure in its original shape, on the right is the recognized shape by the FAVOR method. As an example, for the limitations of the method, the top left circle is completely neglected by the FAVOR method on the right (arrow pointing in empty space), due to no intersecting corners. The same goes for the triangular tip on the right side (arrow pointing at the structure) of the dominant central shape, which may have important implications for the flow behaviour.

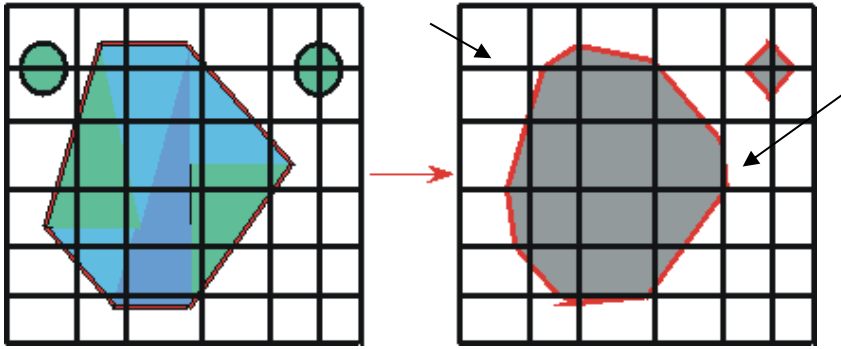


Figure 3-2 Solid recognition examples by the FAVOR method used in Flow 3D® [23]

Chapter 4

Implementation of Numerical Models

4.1 Preliminary remarks

This chapter will focus on the creation of the 3D model, based on the case study and its transfer into the mesh environment of the Flow 3D® software. Also the generation of the different meshes and their boundary conditions will be explained. This chapter will conclude with the selection of the solving algorithm and models.

4.2 Case study, Pedrógão dam

The “Pedrógão” dam is part of the “Alqueva project”, with its main purpose to ensure water supply security for the surrounding 400 ha² of agricultural land. The large hydroelectric dam, “Alqueva”, is a 96m high dam and has a storage capacity of up to 3.15 hm³ usable water. The power producing turbines have a rated power of 2 * 260MW [33], the whole structure can be seen in Figure 4-1.



Figure 4-1 Alqueva dam, view from downstream (photograph by the author, December 2017)

The focused structure of this report is the smaller partner Pedrógão dam. This smaller dam has been added to the project to enable the use of the hydroelectric dam as a day-night cycle pump storage system and is located 20km downstream. Pedrógão is 43m high and has a usable storage capacity of 54hm³, with an installed turbine power of 10MW. Pedrógão started operation in 2006, 4 years after its larger partner Alqueva [33].



Figure 4-2 Pedrógão dam, view from downstream (photograph by the author, December 2017)

Due to its relatively small height, financial and other considerations, a overtopping stepped spillway with RCC construction method was chosen [33].

4.2.1 The experimental study and its purpose

In 2003 the National Laboratory of Civil Engineering (LNEC) in Lisbon was in charge with the safety analyses of the protection walls downstream. This part summarizes the experimental study reported in [34]. The Pedrógão dam has been subject of model scale testing in the facilities of LNEC. These studies were commissioned by EDIA to reconsider the safety of the embankment protection and cavitation damage safety of the existing structure, Pedrógão dam. For this purpose, LNEC has built a 1:65 scale model of the environment of Pedrógão and the hydraulic system to sustain testing of varying unit discharges up to $12000\text{m}^3\text{s}^{-1}$ (scaled to prototype). The upper end of the simulation range has been determined as a 1000 year flood and determines the maximum discharge of certified safety of the structure [34].

4.2.2 Experimental set-up

In LNEC physical model studies, the surrounding topographic information, construction plans and rating curves of outflow and inflow of Pedrógão dam were provided by EDIA. All original plans are displayed in the Appendix E. Based on the given topography and the construction plans a concrete model of the dam and its surroundings was built, including a gravel river bed, for scour movement representation. Figure 4-3 shows a scheme representing a cut through the model at the LNEC laboratories where the important locations of the roller and surge in the roller bucket basin are marked [35].

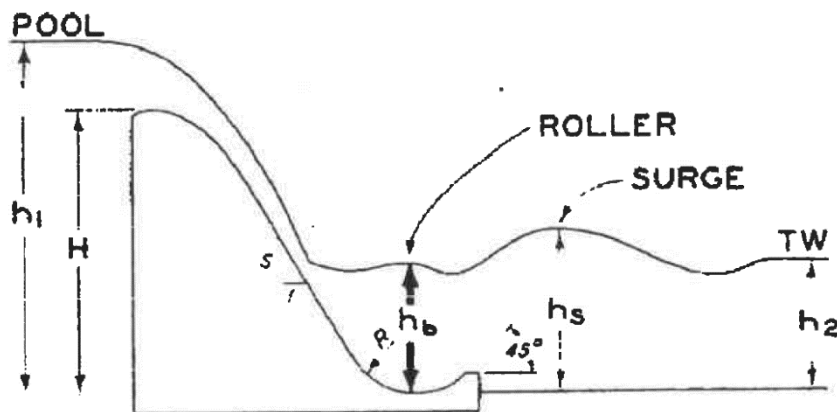


Figure 4-3 Representative slice of Pedrógão dam, including important positions in roller and surge locations, from the original report, [35] in [34].

Roller and surge are the focused-on flow depths in the report since they have been identified as the dominating flow depths, dictating the shape of the shore protection walls.

4.2.3 Execution

The tests were executed for a range of discharges, most of the documented analyses focus on the $12000\text{m}^3\text{s}^{-1}$ discharge scenario and are supplemented by some data for a $7000\text{m}^3\text{s}^{-1}$ discharge scenario. The free surface elevation oscillates and has been observed carefully during the testing. The oscillation was documented in minimal and maximal values for the pressure head data and surface elevation in the roller bucket, separately documented for surge and roller [34]. Additional information informally obtained from J. Falcão de Melo, author of [34] include subjective observations that the shape changes of river bed downstream of the structure had a significant impact on the flow depth in the roller bucket. A picture of the river bed, after a $12000\text{m}^3\text{s}^{-1}$ test, can be seen in Figure 5-11. In this informal statement, the author of the report could not give a definite answer if this change in the roller bucket impacted the non-aerated chute section. Considering the purpose of the study and small geometrical scale, the main flow measurements should be analysed with caution. As a given example, the free surface measurements were taken manually, as well as being measured at the side walls, left and right. The measurements at the side walls are expected to be higher than those at the centreline, due to bulking, the magnitude of which remains to be discussed.

4.2.4 Results and discussion

The LNEC study came to the conclusion that the bank protection was not sufficient and suggested a higher layout. On the other hand, they found no risk of cavitation along the ogee crest weir and stepped chute [34]. After considering a risk analysis, EDIA decided on the upgrade on the embankment protections walls for a flow rate of $7000\text{m}^3\text{s}^{-1}$, smaller than that corresponding to the 1000 year flood.

4.3 Creation and import of the 3-dimensional model

The model of the Pedrógão dam has been created in the 3D modelling software, Inventor, on the basis of official construction drawings of December 1999 and can be seen in the Appendix E [36]. The completed 3D model has been exported as an stereolithography file type and then imported into Flow 3D®. Figure C-1 shows the settings used in the Inventor export. Flow 3D® itself uses the stereolithography data format to handle its solid objects during simulation. In the case of a build model in Flow 3D® or one of the other import methods, Flow 3D® transforms the solid into the stereolithography data format. This format saves the surface data in the form of coordinates for individual triangles and a

normal vector pointing away from the inner parts of the solid, Figure 4-4.

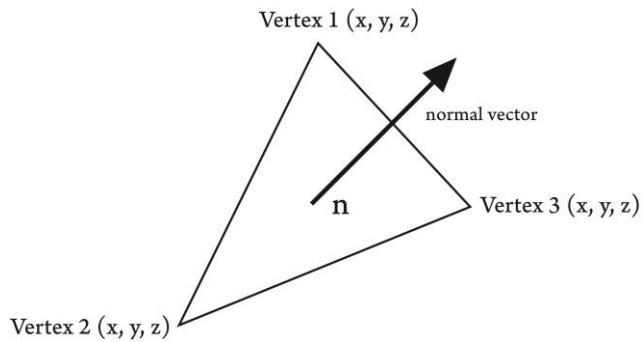


Figure 4-4 Single stereolithography triangle with its vertex coordinates and its normal vector, example of stereolithography data format [23]

Importing the solid data in a stereolithography format in the first-place reduces the simulation preparation time significantly and gives control over the resolution. If the pre-processor of Flow 3D[®] creates the stereolithography data, the relevant mesh resolution is used for the stereolithography resolution [23]. By exporting from third party software the resolution can be fine-tuned.

4.4 Mesh generation and orientation

As discussed in section 3.8 the application of the FAVOR algorithm in Flow 3D[®] is considered in choosing and orientating the meshes. For this specific case it was chosen to orientate the mesh positioning and cell size on the dominant reoccurring step size of 0.6 m height and 0.48 m length. It was settled on three different mesh sizes, 1:3, 1:6 and 1:12, of the dominant geometrical parameter, the step height. The absolute cell size was determined by the step height divided by, 3, 6 and 12, therefore the absolute cell sizes were, 0.2 m, 0.1 m and 0.05 m. Common practice in CFD simulation increases the cell size in the region leading up the critical region as well as the roller bucket region [6] [23]. A picture of all the mesh regions can be seen in Figure 4-5.

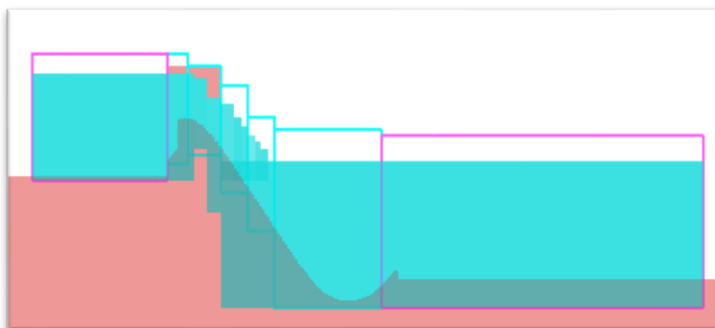


Figure 4-5 Mesh blocks in the simulated environment

The first and last mesh blocks, in x direction, are called rough mesh blocks (pink marked in the Figure

4-5), these were considered to be leading up to the simulation environment and downstream of the roller bucket. Following these common practices, the rough mesh block were double in size during the 1:12 simulations. All exact mesh sizes are mentioned in Table 4-1. The specific information on all mesh setups can be found in the Appendix D. The mesh setups will be referred to from here on as 1:3, 1:6 and 1:12 and the related cell size information is shown in Table 4-1. All simulations will be executed in one of these mesh styles and as mentioned, are named after the cell size, which is a fraction of the dominant geometrical characteristic, the step height.

Table 4-1 Mesh cell sizes and total number of cells

	Rough Mesh	Fine Mesh	Total Number of Cells
	[m]	[m]	[-]
Mesh 1:3	0.2	0.2	75225
Mesh 1:6	0.1	0.1	300900
Mesh 1:12	0.1	0.05	923200

As mentioned earlier the meshes should be orientated towards the dominating structure as closely as possible and at least two cells per dominating influence, structure, turbulent eddy, etc. [37]. Therefore, the mesh was positioned to have its boundary of cells aligned with the surface of the most reoccurring geometrical measure, the stepped constant sloping chute reach. Since the step height is the determining factor of the mesh size, the meshes were orientated at the horizontal edge of the steps as shown in Figure 4-6.

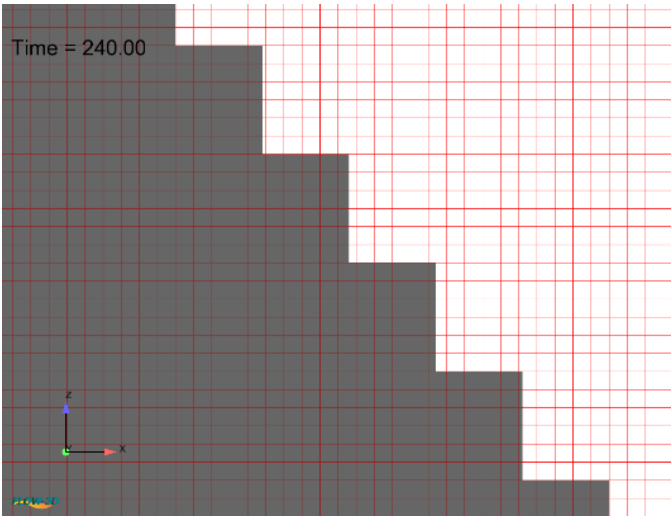


Figure 4-6 Cell orientation on the constant sloped reach of the stepped spillway

The largest discrepancies between the solid structure and the mesh representation occurs at the ogee crest of the dam. As shown in Figure 4-7, the resolution of the mesh sizes is insufficient for the complex shape of the ogee crest.

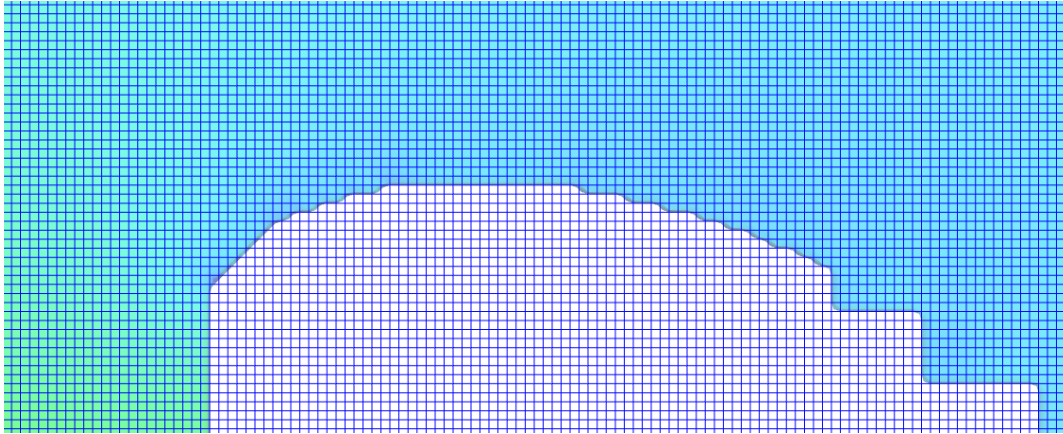


Figure 4-7 Outline of the individual cells in the ogee crest region for the 1:12 mesh size

A second set of simulations in the scale of 1:65 was executed and organized in the exact same way. All mesh sizes and structures are scaled exactly 1:65. The mesh orientation was kept the same as the full-scale simulations. The absolute values of cell size are scaled by the same factor. Therefore, the mesh setups stay the same and are referred to as, 1:3 model scale and 1:6 model scale with 3.08 mm and 1.54 mm cell sizes, respectively. Due to the constant scaling of all geometrics the meshes have the same number of cells as their full-scale counter parts, as shown in Table 4-2.

Table 4-2 Mesh cell sizes and the total number of cells in the scale set ups

	Rough Mesh	Fine Mesh	Total Number of Cells
	[m]	[m]	[-]
Mesh 1:3	0.00308	0.00308	75225
Mesh 1:6	0.00154	0.00154	300900

4.5 Boundary condition selection

Due to the common simplification in CFD simulations of assuming a 2D flow, the same was done in all executed simulations. All walls have been set with the symmetry conditions, apart from global x_{min} and x_{max} . Inflow and outflow use the static pressure condition, with a given water elevation, explained in section 3.6. The water elevations were determined using the rating curves mentioned in section 4.2.2 and shown in Appendix E. The flow will then adjust itself to create the necessary volume flux. Same goes for the outflow, it is set with constant pressure and water elevation, which in turn follows the rating curve provided by EDIA [33]. Flow 3D[®] detects automatically neighbouring mesh blocks and connects them.

4.6 Steady state criterion

In the field of CFD simulations common steady state criteria are, the “Mass-averaged turbulent kinetic energy”, the “Mass-averaged fluid mean kinetic energy” and “Mass-averaged turbulent dissipation” [23]. These steady state criteria were also applied in the simulations of this thesis. The chosen numerical values were no change higher than 1% in any of the three values over a time period of 10s. Nevertheless, the mainly discussed simulations, 1:6 mesh sizes were run longer. An overview over the simulation environment can be seen in Figure 4-8. All steady state graphs as outputs of the post processing software FlowSight, can be found in Appendix G.

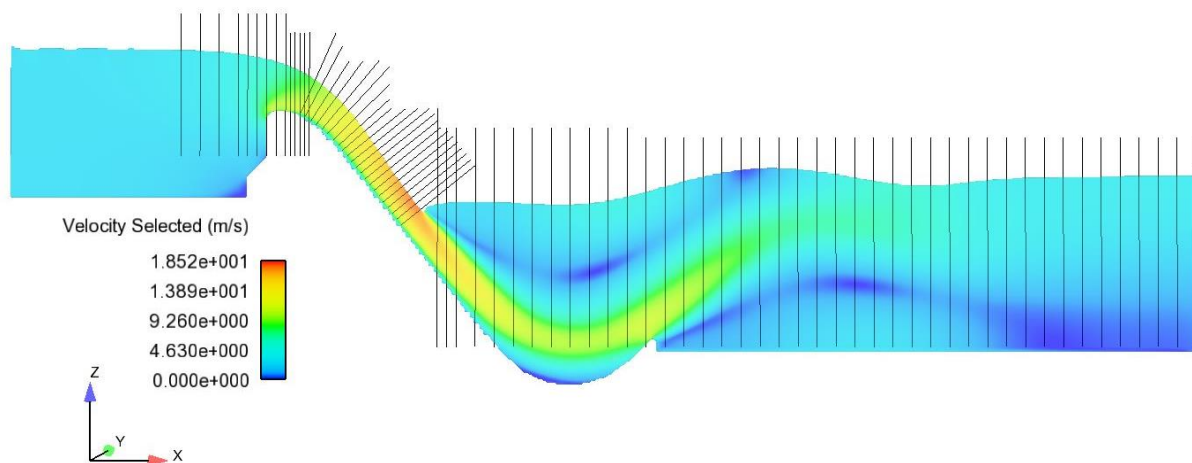


Figure 4-8 Overview over simulation environment, with isometric colouring for velocity

4.7 Probe positioning

Probes are used in Flow 3D® for specific data extraction. This report utilized mostly line probes and a few point probes. The lines probes can be positioned by end and beginning coordinates. For each probe the data to be extracted can be specified, to show any simulated value. The data can then be transferred via clipboard to spreadsheet software, for example “Microsoft Excel” and be processed further.

4.7.1 Step probes

The step probes were positioned at the tips of each step. The reason for that is that most data analyses in skimming flow use the pseudo-bottom as reference. As discussed earlier in section 2.3.3, the pseudo-bottom is the line along all tips of the steps along the chute. Therefore, all probes start at the tip of the steps and therefore at the pseudo-bottom. In the reach of the ogee crest the tips of the steps follow the function

$$z = \frac{5}{2} \left(\frac{x}{5} \right)^{1.85} \quad 4.1$$

where x is the relative horizontal distance to the crest and z the vertical distance to the top of the crest in negative vertical direction. To be able to get perpendicular probe lines this function was derived, and perpendicular norm vector calculated. Using this the start and end coordinates of the line probes were determined, as well as the corresponding equations describing the positioning of the individual probes, in the given coordinate systems. All step probe functions are displayed in Figure B-1 of the Appendix B. These equations serve the purpose of displaying the probes in graphs and being able to handle flow depth results mathematically.

4.7.2 Ogee crest probes and roller bucket probes

In the smooth reach and in the terminal structure reach, vertical probes were used in selected intervals. In the regions closest to the stepped chute region smaller intervals between the probes were selected, to obtain a better surface resolution. These probes have only been used for surface recognition. Their positioning can be seen in Figure B 1 of the Appendix B.

4.7.3 Pressure taps

The experimental readings for the pressure head in the physical model were carried out with piezometers [34]. The translation to extract the same data from the CFD model would mean point probes at these specific coordinates. Surface pressure extracting from CFD simulation is very sensitive task and needs human intervention, as well as common sense, to be reliable. Figure 4-9 shows the location of a line probe in FlowSight. This line probe is located along the ramp at the downstream end of the roller bucket. Such a linear structure surface is suitable for easy and reliable data extraction. An overview over the coordinates of all probes is presented in Table B-1 of the Appendix B.

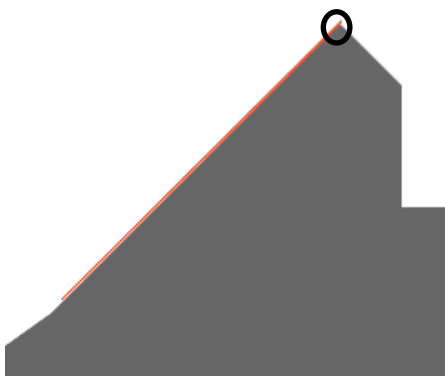


Figure 4-9 Line probe for pressure reading, along the ramp of the roller bucket, slight extension of the line probe is marked

At the ogee crest, the data collection is a very difficult and sensitive task. To match the surface as closely as possible a line probe has been positioned at the ogee crest (Figure 4-10).

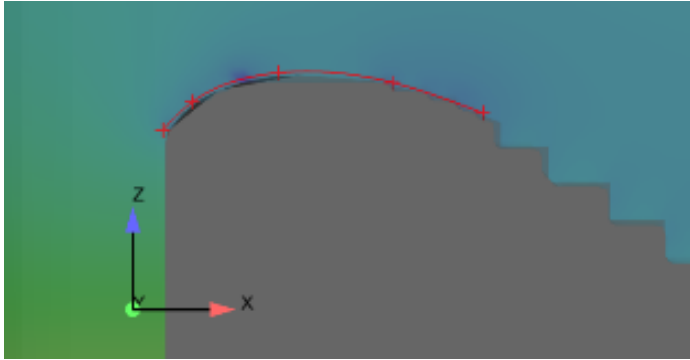


Figure 4-10 Manually positioned spline probe

The data is highly unreliable as visible in Figure 4-11, the difference is often a single CFD cell between realistic readings and readings that are corrupted by small volume fractions, due to the presence of the crest itself. Figure 4-11 shows the pressure readings along the spline probe at the crest, where the distance indicates the progress along the spline starting on the left side of Figure 4-10. Figure 4-12 shows the pressure evolution perpendicular to the top most part of the crest.

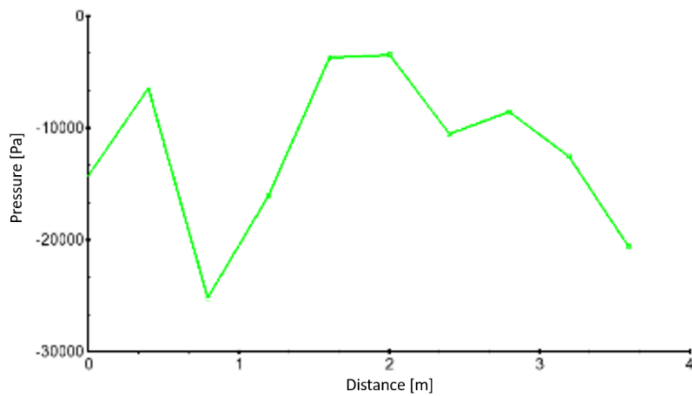


Figure 4-11 Pressure development along the manually positioned spline probe (increasing x coordinate with distance), screenshot of the output graph in the post processing software FlowSight, adapted axis labels

Every data point present in Figure 4-10 – Figure 4.12 represents a centre of a cell. The very first cell has been chosen to be inside of the concrete and therefore has “void” pressure. The next cell at 0.02m is the first cell which centre is inside of the flow reach. Due to the FAVOR method this cell is influenced by concrete of the original stereolithography model. Therefore, it averages the fluid pressures with the “void” pressure of the concrete structure. The third data point at 0.04m is the first cell which shows pure fluid pressure and therefore can be considered for comparison with the pressure head of the piezometer of the experimental model data. This creates confusion since the coordinates of the probes will not be the exact same between the two pressure heads, this has to be sacrificed to extract correct data from the CFD simulations.

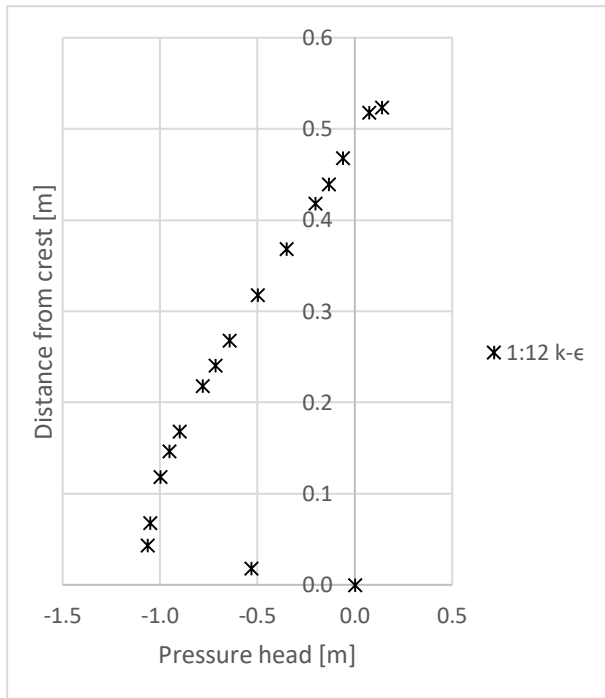


Figure 4-12 Pressure development perpendicular distance evolution, leading away from the crest

Due to these averaging in cells and the resulting inconsistencies, all probes later in this report have been positioned manually and not at the exact coordinates as the experimental model data would demand. In this report no coordinates will be used to the pressure taps or pressure probe, instead they will be referred to as their number given by the LNEC report. A 3-dimensional view, which shows red dots as the positions of the pressure probes is presented in Figure B-4 of the Appendix B.

4.8 Experimental flow depths

The model data from the experimental studies were handed forward to the author of this study in a printed format. The free surface elevation information was taken using “Auto CAD Inventor” and scaled to match the simulation results. A screenshot of the measuring process can be seen in the Appendix E, Figure E-5. These measurements are documented as individual datapoints. The individual data points are converted by the trendline function of Microsoft Excel to generate a function to enable mathematical handling for the necessary data comparisons. The total free surface has been separated in two regions, the chute region and the roller bucket. The free surface elevations were measured on both sides of the chute, left and right [34], here is to say that only the right wall data set will be considered in the comparisons due to the shifted position of the shore protection walls. The representing graphs and the measured free surface coordinates are shown in the Appendix F. The simulation environment is referred to in a cartesian coordinate system, z is representing vertical distance and increasing x coordinates the progress along the river, shown in Figure 4-14. The representing equations are, for $Q_w = 12000m^3s^{-1}$:

Right wall chute region,

$$z = 2.796 * 10^{-6}x^6 - 1.054 * 10^{-4}x^5 + 1.308 * 10^{-3}x^4 - 6.841 * 10^{-3}x^3 - 5.681 * 10^{-3}x^2 - 2.912 * 10^{-1}x + 9.095 * 10^1 \quad 4.2$$

Right wall roller bucket

$$z = -3.461 * 10^{-7}x^6 + 8.005 * 10^{-5}x^5 - 7.606 * 10^{-3}x^4 + 3.795 * 10^{-1}x^3 - 1.047 * 10^1x^2 + 1.512 * 10^2x - 8.144 * 10^2 \quad 4.3$$

Left wall chute region

$$z = 8.717 * 10^{-6}x^6 - 4.397 * 10^{-4}x^5 + 8.575 * 10^{-3}x^4 - 8.272 * 10^{-2}x^3 + 3.797 * 10^{-1}x^2 - 1.132 * x + 9.179 * 10^1 \quad 4.4$$

Left wall roller bucket

$$z = 2.209 * 10^{-7}x^6 - 4.99 * 10^{-5}x^5 + 4.562 * 10^{-3}x^4 - 2.155 * 10^{-1}x^3 + 5.546 * x^2 - 7.371 * 10^1x + 4.723 * 10^2 \quad 4.5$$

For $Q_w = 7000m^3s^{-1}$ the equation obtained for the right wall of the roller bucket is:

$$z = -1.46 * 10^{-8}x^6 + 1.63 * 10^{-6}x^5 - 1.899 * 10^{-5}x^4 - 4.295 * 10^{-3}x^3 + 2.270 * 10^{-1}x^2 - 4.377 * x + 1.033 * 10^2 \quad 4.6$$

Figure 4-13 shows a picture of the original graphs the free surface data was derived from, with digital overlays of the representation formulae and the dam surface.

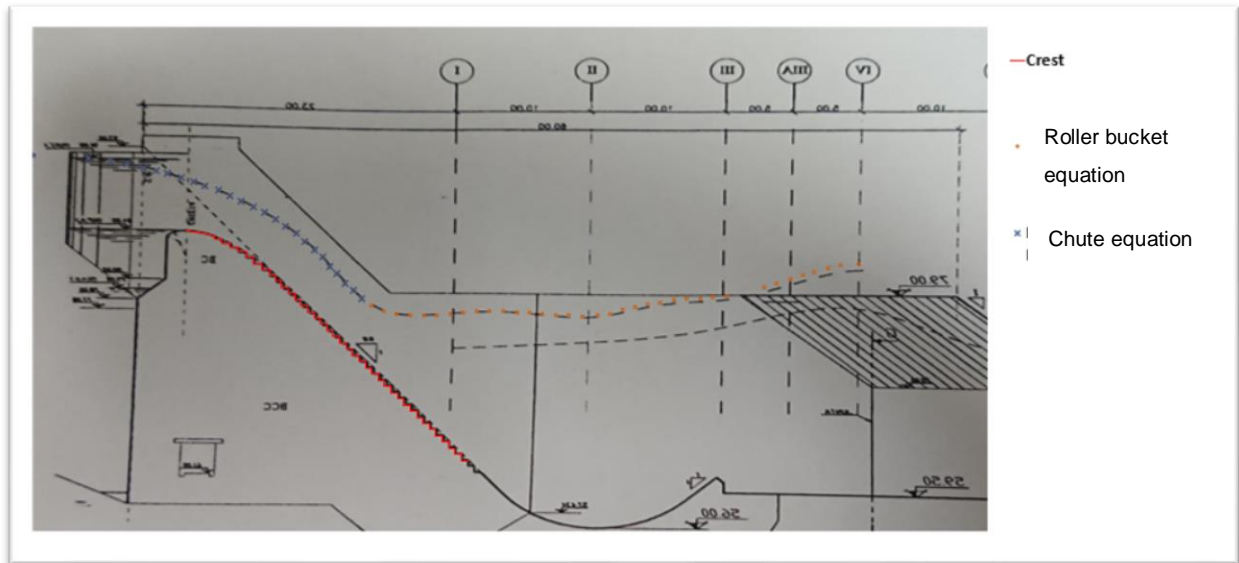


Figure 4-13 Free surface digital data overlay on top of the original graph

The flow depths were then determined by setting the equations and the equations of the step probes equal to find their intersection point. For simplicity the numerical solver function of Microsoft excel has been used to find the intersecting x coordinate. For the possible solver solutions minima and maxima were given to the excel solver, in the form the start/end coordinates of the probes perpendicular to the steps. The intersecting x coordinate can then be used to derive the flow depth obtained in the model experiments.

4.9 Mesh convergence

As described in section 4.4 all simulations were executed in the meshes 1:3, 1:6 and 1:12 (Table 4-3). This report focuses the analyses on two different regions, the chute reach and the roller bucket reach. Therefore, two mesh flow depth convergence analyses were done independently of each other, as well as a velocity convergence analyses, in steady state.

4.9.1 Chute region

The chute region of the simulated stepped spillway has as major obstacle the steps in its surface. The mesh has been geared towards accommodating the steps. Table 4-3 shows quite clearly the importance of cell size in the reach of the chute. The differences were calculated using equation 4.7,

$$\delta\% = \left| \frac{d_{1:6,L_i} - d_{1:12,L_i}}{d_{1:12,L_i}} \right| * 100 \quad 4.7$$

Due to the small average difference of ~3% in the chute region the 1:6 mesh set up was considered to

provide effectively mesh size independent results. Perpendicular probes were used as measurement positions, explained in section 4.7.1 and shown in Figure 4-18 in the appendix.

Table 4-3 Relative flow depth differences on the chute based on mesh size and turbulent model

Mesh size and turbulent model	avg. $\delta\%$	max. $\delta\%$
1:12 k- ϵ to 1:3 k- ϵ	10.30	14.77
1:12 k- ϵ to 1:3 RNG k- ϵ	10.72	14.77
1:12 k- ϵ to 1:6 k- ϵ	1.15	3.02
1:12 k- ϵ to 1:6 RNG k- ϵ	2.93	6.21

A full overview over the flow depths at specific steps for all mesh resolutions are shown in Table A-1 of the Appendix A. Figure 4-14 shows the chute and the flow depth of all mesh resolution simulations visually. This visual overview over the chute show that the 1:3 mesh simulation gives higher flow depths than the 1:6 and the 1:12 simulations.

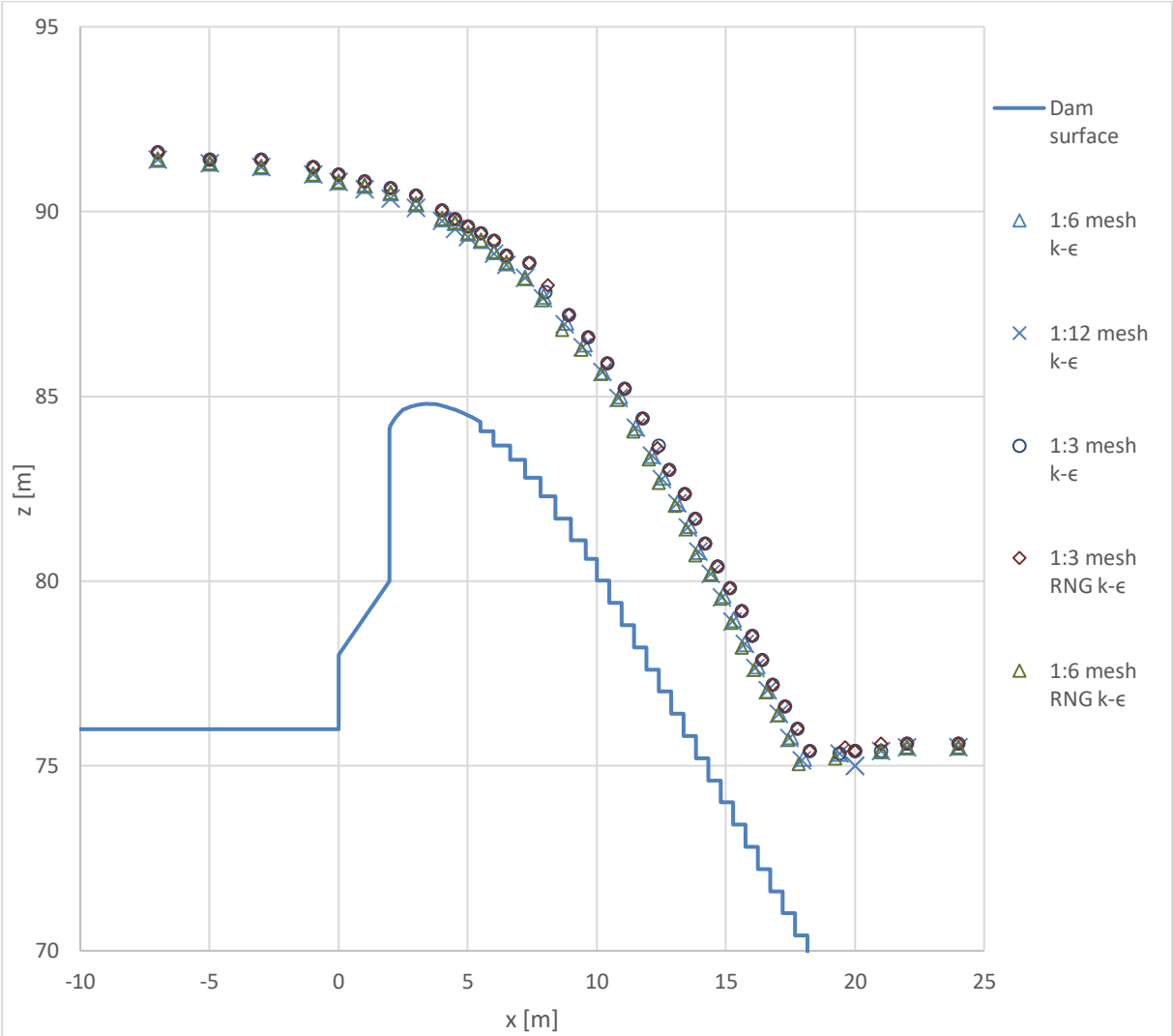


Figure 4-14 Free surface elevation in chute region

The velocity profiles evolve along the chute and show the flow development; the velocity profiles for steps 2, 5, 10, 15 and 20 are shown in Figure 4-15.

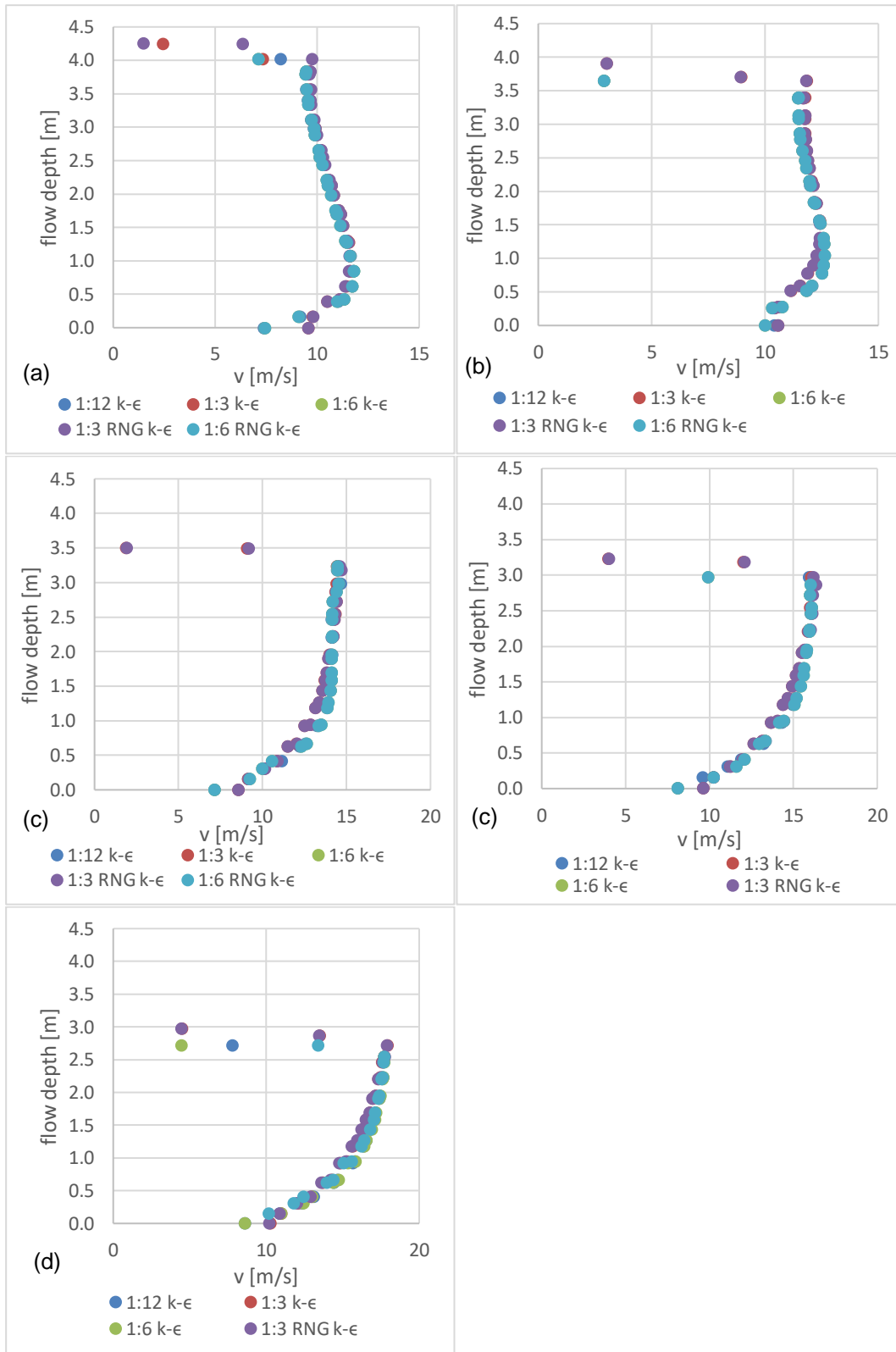


Figure 4-15 (a) Velocity profiles at step 2 ($L/L_i = 0.047$); (b) Velocity profile at step 5 ($L/L_i = 0.084$); (c) Velocity profile at step 10 ($L/L_i = 0.152$); (d) Velocity profile at step 15 ($L/L_i = 0.217$); (e) Velocity profile at step 20 ($L/L_i = 0.282$)

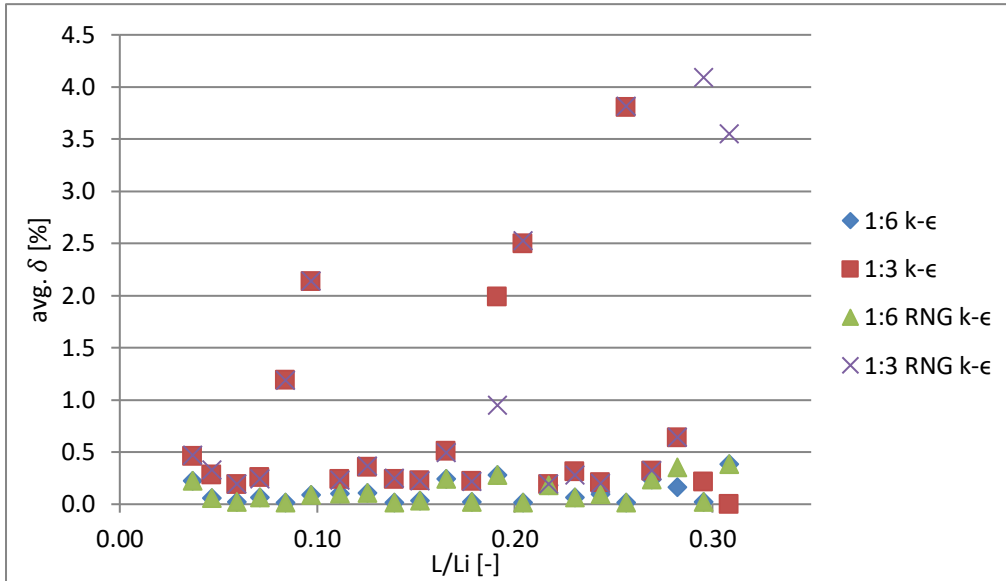


Figure 4-16 Relative average velocity differences per step, of different mesh sizes and turbulent models to the 1:12 k-ε average velocities in function of the individual steps

Figure 4-16 shows the relative differences of the average velocity values per step. Both 1:6 mesh size simulations are constantly within 0.5% of the 1:12 simulation values, and therefore can be considered acceptable. The exact differences per step can be seen in Table F-3 in Appendix F.

4.9.2 Roller bucket

In the roller bucket the physical restricting geometries are at a minimum and do not influence the flow significantly, as described in section 4.4. This reduces the need of small cell sizes in the CFD simulation. The three mesh size setups 1:3, 1:6 and 1:12 described in section 4.4 show very similar results. The analyses of this report has its focus on the free surface elevation or flow depth, which is why this measure is used for the mesh convergence study. The relative differences in flow depth can be seen in Table 4-4 and are calculated with equation 4.8

$$\delta\% = \left| \frac{(z_{1:6,x} - z_x) - (z_{1:12,x} - z_x)}{(z_{1:12,x} - z_x)} \right| * 100 \quad 4.8$$

where, z_x is the river bed elevation at position x and the differences to the individual surface elevations represent the flow depths, e.g. $(h_{1:6,x} = z_{1:6,x} - z_x)$. The 1:12 and 1:6 meshes both have the 1:6 cell size in the roller bucket, and therefore explain the extremely low variation, which is basically only the first 3 probes and the influence of different chute results. Nonetheless even the results of the 1:3 meshes are quite similar to those of 1:12 mesh size, which indicated convergence to be achieved already at the mesh size of 1:3. This confirms the general assumption to be able to use larger meshes in the upstream reservoir and in the downstream reach.

Table 4-4 Flow depth relative differences in the roller bucket to the 1:12 k- ϵ mesh, based on mesh size and turbulence model

Mesh size and turbulence model	avg. $\delta\%$	max. $\delta\%$
1:12 k- ϵ to 1:3 k- ϵ	1.46	3.54
1:12 k- ϵ to 1:3 RNG k- ϵ	1.78	6.26
1:12 k- ϵ to 1:6 k- ϵ	0.03	0.91
1:12 k- ϵ to 1:6 RNG k- ϵ	0.18	1.45

The free surface elevations are displayed in Figure 4-17. The largest variations visually are happening in the developing section of the surge.

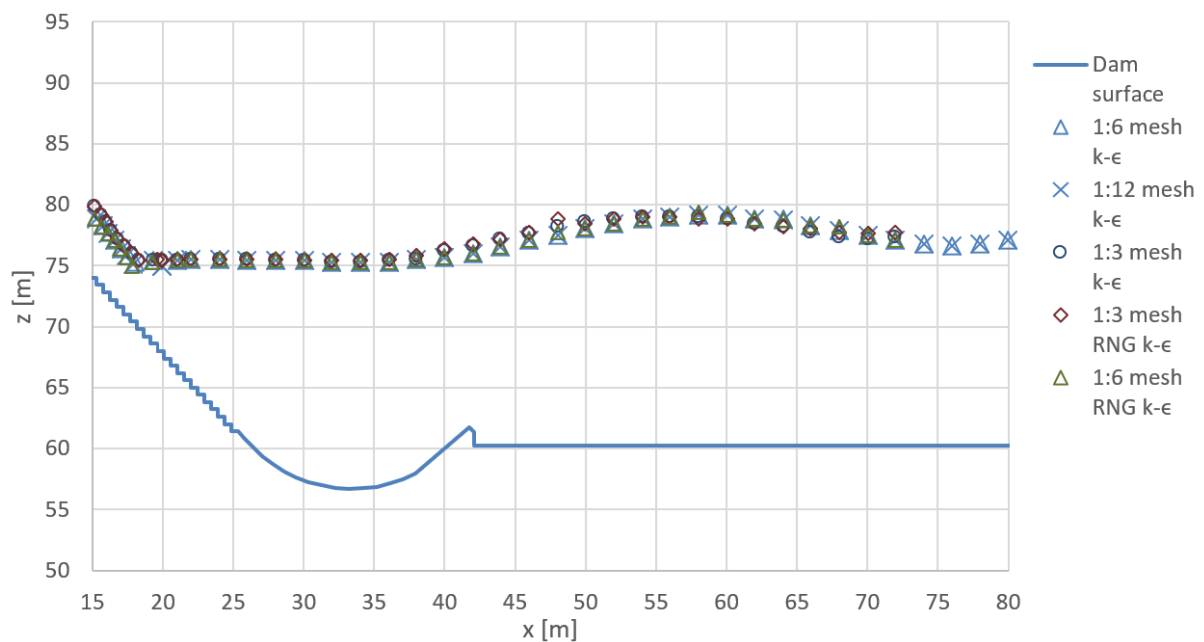


Figure 4-17 Free surface elevation in the roller bucket, for different turbulent models and mesh sizes

4.10 Turbulence model selection

The previous tables, Table 4-3 and Table 4-4 also showed the small variation between the k- ϵ and the RNG k- ϵ models. As discussed in section 3.4. RNG k- ϵ is an adapted k- ϵ model, where the RNG model uses different empirical parameters and replaces one of the empirical constants with a relation to the turbulent dissipation k_t . RNG k- ϵ is known to produce more accurate results, with the cost of longer calculation time. Therefore, RNG k- ϵ simulations were adopted for the subsequent simulations, except for some convergence analyses where longer simulation times were desirable. The influence of the turbulence model analyses will be evaluated along with the flow depth analysis in section 5.2 and 5.3.

4.11 Time convergence for velocities on the chute

A convergence analyses regarding the velocity profiles was also performed, with the 240 s steady state run, with mesh model 1:6 and k- ϵ turbulence model. This simulation was chosen due to the desired extremely long simulation time and the previously shown turbulence model independence, in section 4.9.1. The numerical velocity profiles were compiled with data from the probes perpendicular to the steps 1,5,15 and 20, the steps are indicated in red in Figure 4-18 and explained in section 4.7.1. These specific steps have been selected to be evenly distributed over the clear water flow region. The flow region in Figure 4-18 is coloured, were the colours scales with velocity, as seen in the legend in the top right corner.

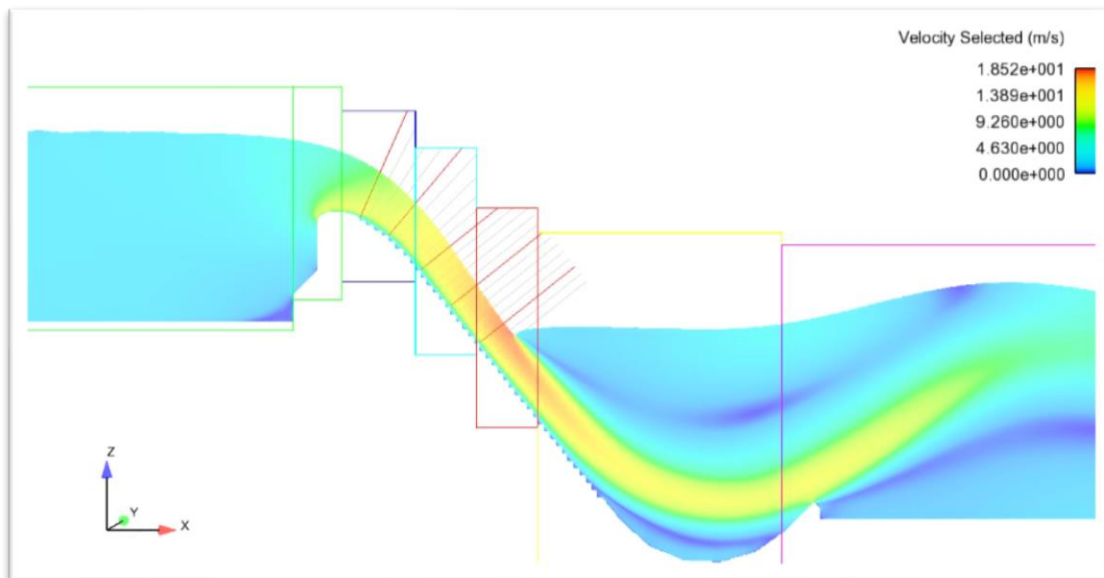


Figure 4-18 Simulation environment with marked analysed steps in the time convergence analysis

Figure 4-19 shows the development of the mass averaged kinetic energy in the simulated environment. The steady state criteria's have been achieved at time $t=150$ s. To verify the convergence of the velocity profiles in the clear water region, five times for data sets have been selected. These were 107 s, 134 s, 213 s, 220 s and 226 s, all times are marked in the steady state criteria evolution of mass averaged kinetic energy in Figure 4-19.

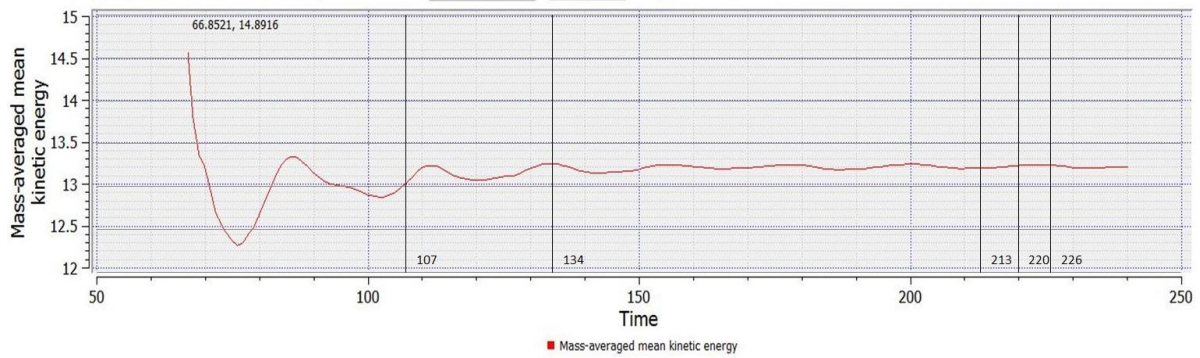


Figure 4-19 Mass-averaged mean kinetic energy time evolution of the 1:6 k-ε 240s simulation

The three times above 200 s have been selected to have a minimum kinetic energy point, a maximum kinetic energy point and a point in the intermediate region. It was also selected a point of very strong change in mass average kinetic energy and a local maximum in mass average kinetic energy at 134 s and a point with large local gradient, at 107 s. All times are marked in Figure 4-19. A picture of the flow states of the simulation environment, for all selected times can be found in Appendix I. Interesting to note on these pictures is how similar the overall shape of the flow stays, even though the mass averaged mean kinetic energy graph implies very significant variation in the flow. The largest difference is visible in the very end of the roller bucket.

For the convergence comparison of the velocity profiles, the latest time, 226 s has been selected as baseline and all other velocity profiles will be compared point by point to the values of time 226 s. All the differences were then converted into relative differences. An example is shown for the comparison between 226 s and 220 s.

$$\delta v_{xy} = \left| \frac{(v_{226(xy)} - v_{220(xy)})}{v_{226(xy)}} \right| * 100 \quad 4.9$$

All results were then averaged over the velocity profile and shown in Table 4-5. This table also shows the maximum differences of the averaged values for all comparisons.

Table 4-5 velocity profile comparisons, avg. δ and maximum δ , in % and $m s^{-1}$

compared to time 226 s	Unit	Time 220 s		Time 213 s		Time 134 s		Time 107 s	
		avg. δ	max δ						
Step1	abs. $m s^{-1}$	3.19E-06	1.85E-06	1.27E-05	2.09E-05	1.53E-04	1.85E-04	4.43E-05	2.35E-04
	%	0.00323	0.00157	0.01282	0.01770	0.15433	0.15687	0.04479	0.19848
Step5	abs. $m s^{-1}$	7.31E-06	1.90E-05	4.56E-06	8.09E-06	1.20E-04	1.52E-04	1.29E-04	3.02E-04
	%	0.00631	0.01501	0.00394	0.00640	0.10392	0.12024	0.11098	0.23854
Step10	abs. $m s^{-1}$	4.19E-05	3.31E-05	1.12E-05	2.65E-06	6.29E-05	1.34E-05	1.90E-04	4.85E-04
	%	0.03269	0.02282	0.00876	0.00183	0.04912	0.00921	0.14863	0.33406
Step15	abs. $m s^{-1}$	1.01E-04	2.01E-04	3.78E-05	1.56E-04	1.90E-04	3.42E-04	1.04E-03	1.16E-03
	%	0.07228	0.12556	0.02697	0.09758	0.13539	0.21320	0.74066	0.72322
Step20	abs. $m s^{-1}$	4.21E-04	1.09E-03	3.06E-04	5.88E-04	1.07E-03	2.39E-03	8.23E-03	1.59E-02
	%	0.27730	0.61684	0.20125	0.33188	0.70702	1.35165	5.41854	9.00661

Table 4-5 shows that the largest average difference between the times 226, 220 and 213 s is 0.3%. The largest individual point difference is 0.6% at step 20. Both values are more than sufficient for the accuracy desired for this study, therefore this work will use values taken at single time steps for, for the velocity profiles and will assume their accuracy to be sufficient.

Chapter 5

Results

5.1 Preliminary remarks

This chapter is dedicated to comparing the CFD results with empirical formulae as well as with experimental data from the physical model of Pedrógão dam. Comparisons include the flow depths in the chute region, qualitative showing velocity profiles, the flow depths in the roller bucket reach and the pressure heads on the spillway surface of the crest region and on the ramp of the roller bucket.

5.2 Flow depths on the chute

The flow depths on the chute of the stepped spillway can be compared between different methods. As mentioned in section 2.3.3 the free-stream velocity can be calculated by equation 2.3. Due to the continuity law the flow depth can be calculated using the analytical boundary layer depth, calculation based on Meireles, et al. [19], as described in section 2.3.3 . These combined calculations are then iterated to find the predicted flow depth. Meireles et al. [19] also proposed an empirical method, which uses a single calculation process to estimate the flow depth in skimming flow over steeply sloped chutes, as described in section 2.3.3. It is important to mention that this method is applicable for $L/L_i \geq 0.1$. Figure 5-1 shows these empirical predictions as well as the selected CFD simulation results and the experimental results of LNEC [34]. This is shown in the simulations coordinate system with the dam surface as reference points. As mentioned in section 4.7.1, the flow depths were measured perpendicular to the dam surface.

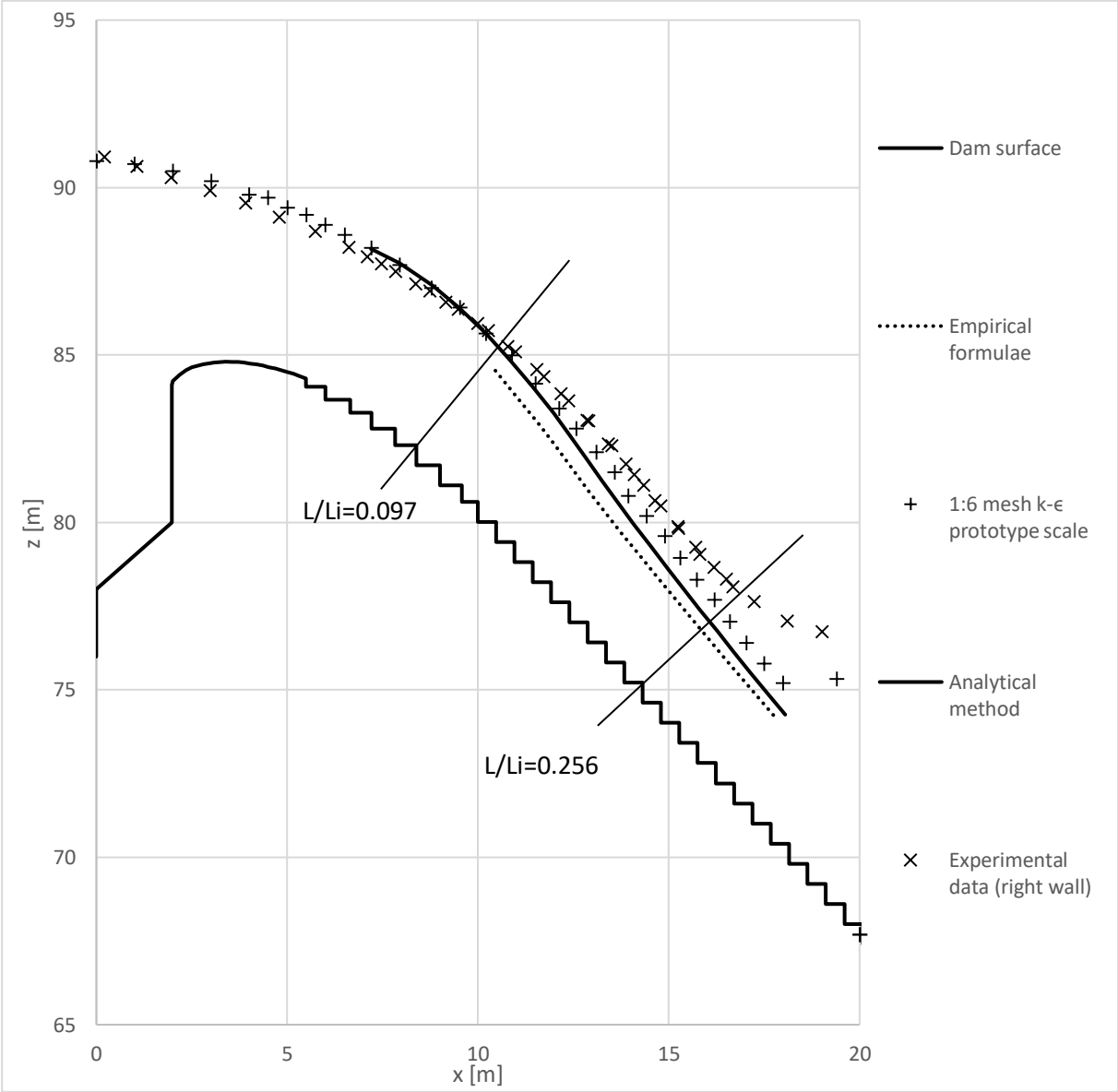


Figure 5-1 Free surface elevation along the chute

Visually the empirical method, analytical method and CFD flow depth predictions represent the experimental results rather well. The compared flow depths are plotted in function of the L/L_i , in Figure 5-2. The experimental flow depths are the smallest in the very early parts of the chute, this reverses latest at $L/L_i = 0.08$ and the flow depths keep diverging. The empirical method, analytical method and the CFD simulations predict smaller flow depths in the higher L/L_i parts, as seen in Figure 5-2. One of the main reasons for this could be the bulking at the chute walls. As described in section 4.2.3 the experimental measurements were taken at the wall while the empirical and CFD simulations refer to the centre of the chute cross-section. The graph is plotted until $0.25 L/L_i$ due to the start of the tailwater flow, and the resulting distortion of the graph.

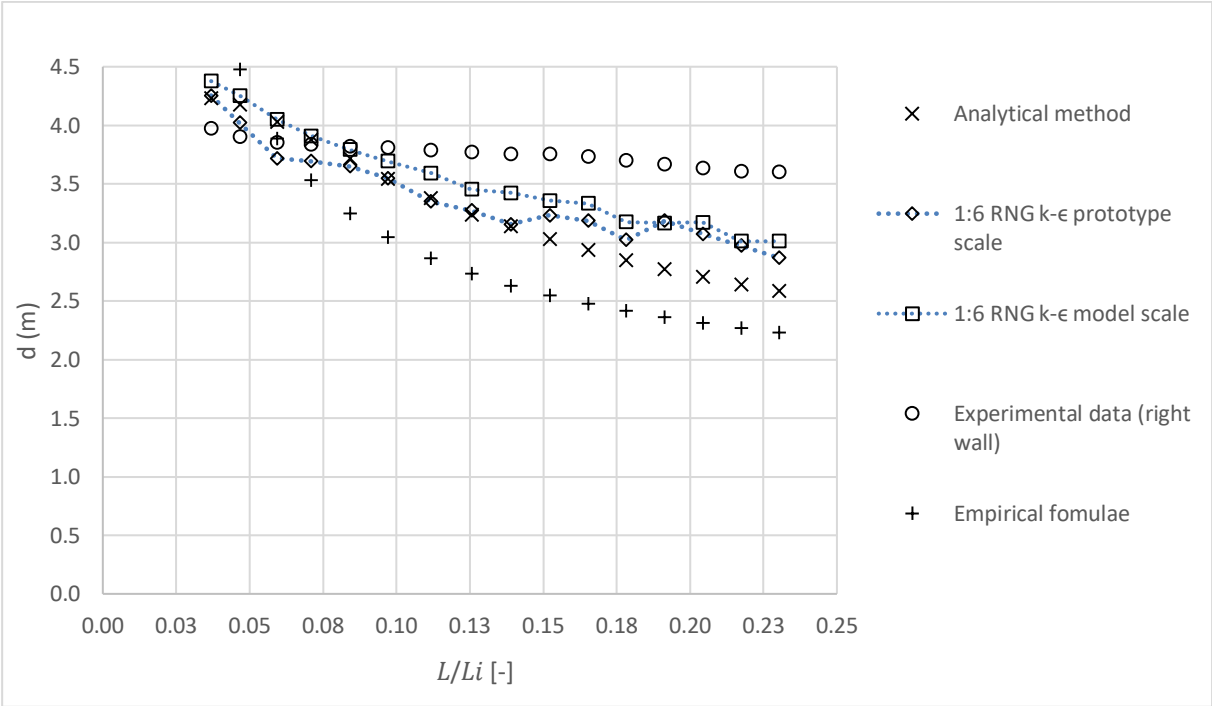


Figure 5-2 Flow depth along the chute

This behaviour was observed in the same way by the experiments of Bombardelli et al. [6] which consisted of a very similar set up, of similar ogee crest, and a chute slope of 53° . As mentioned before Pedrógão has a chute slope of 51° . Bombardelli et al. [6] does not mention specific difference values for the smaller L/L_i values, visual analyses show them to be on average $\sim 10\%$ larger. The measurements in the experiments carried out by Bombardelli et al. [6] were measured in the centre of the chute cross-section and therefore do not contain bulking distortion.

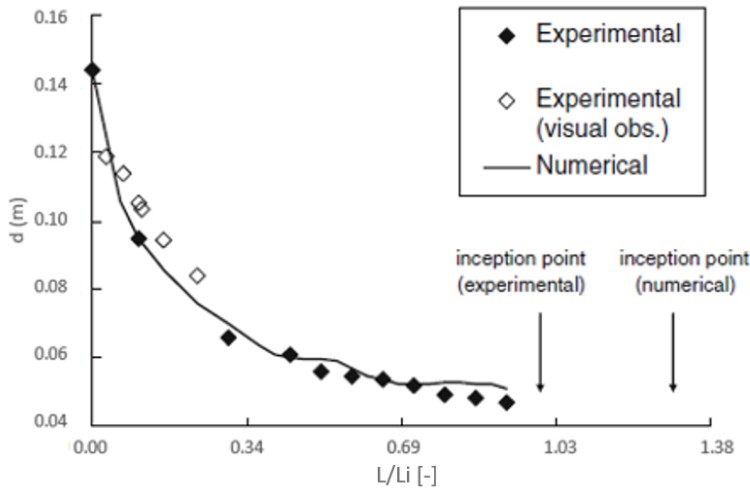


Figure 5-3 Flow depth results by Bombardelli et al. [6], adapted to have L/L_i axis

Figure 5-4 shows the flow depth differences in abs. $\delta\%$ when compared to the experimental values of LNEC, plotted in function of L/L_i . The simulation in 1:65 scale represents the experimental values the closest.

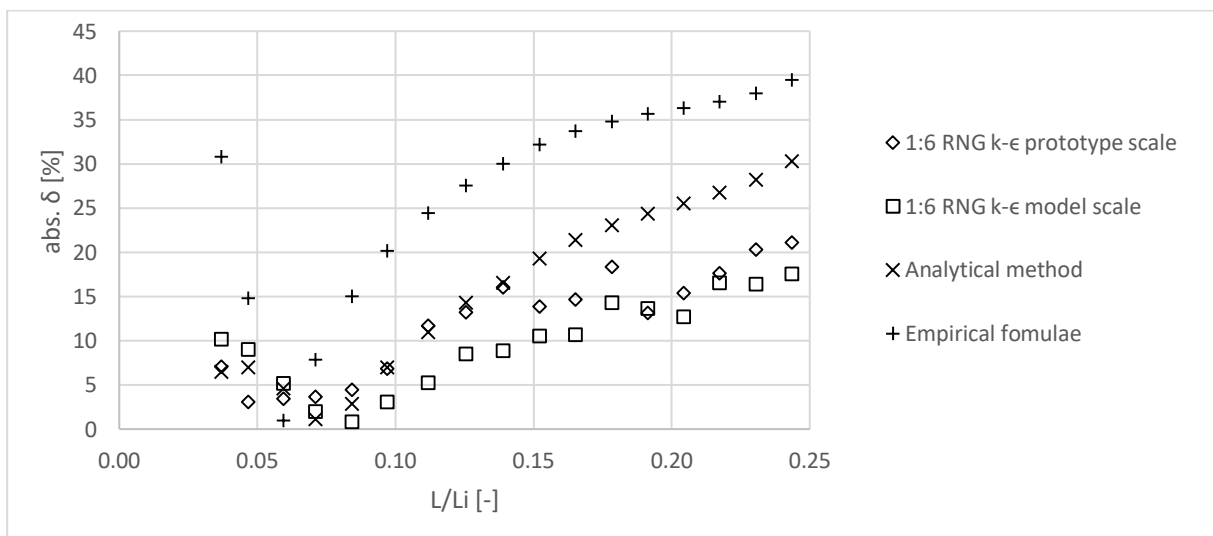


Figure 5-4 Flow depth differences compared to their experimental counterpart

When comparing the prototype scale CFD simulation and the model scale CFD simulation to the experimental values, the scale simulation is closer to the experimental values. Scaling in CFD simulations is its own research field and this comparison between the simulations clearly show that there are non-negligible effects in CFD scaling. Table 5-1 shows the average discrepancies. These averages were taken over all steps (perpendicular line probes, section 4.7.1) upstream of the roller bucket. This excludes the empirical formulae method results of the first steps, due to being outside of these methods applicability area. A full overview can be seen in Table F-1 in Appendix F.

Table 5-1 Flow depth average and maximum, relative differences to LNEC experimental results

	Analytical method	1:6 RNG k-ε prototype scale	1:6 RNG k-ε model scale	Empirical formulae
	δ[%]	δ[%]	δ[%]	δ[%]
Average	15.87	12.00	9.71	26.99
Maximum	30.31	21.13	17.57	39.49

Considering that the empirical formulae were based on various laboratory data absent of bulking effects, the empirical estimations should be considered reliable. A similar drift between CFD simulation results and experimental data, against analytical predictions, indicating diverging flow depths along the chute, is visible in Figure 5-5. This figure shows the absolute $\delta\%$ differences of the analytical predictions with the CFD simulations, empirical formulae and experimental data in function of L/L_i .

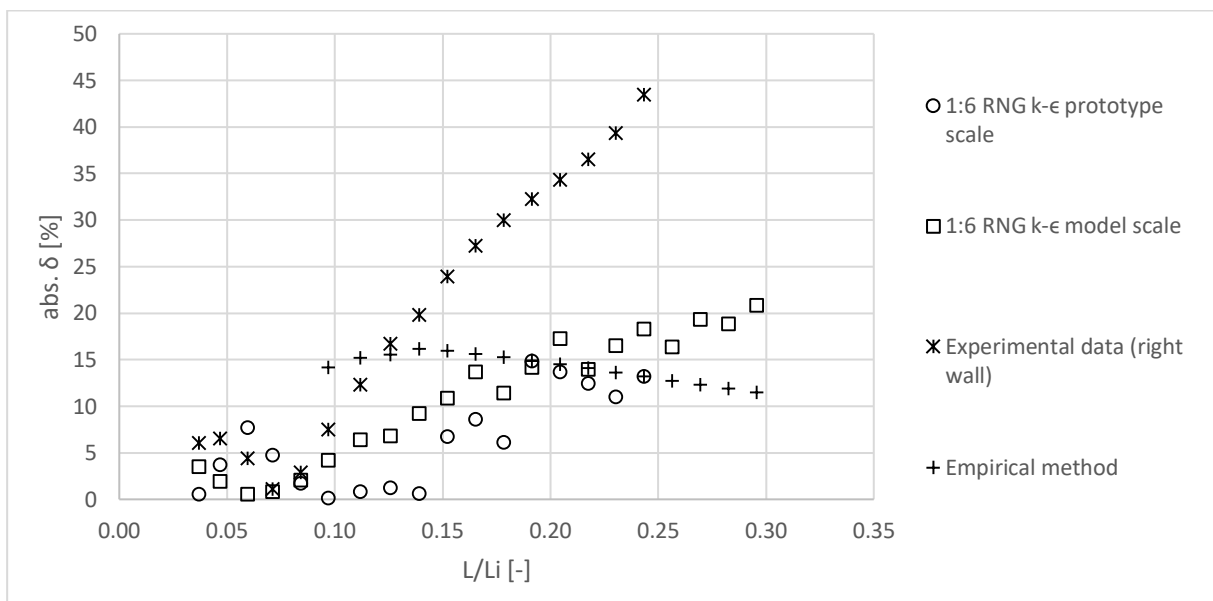


Figure 5-5 Flow depths relative differences of analytical formulae versus CFD simulation, empirical formulae and experimental data in function of L/L_i

Figure 5-6 compares the absolute differences in flow depth of the CFD simulations and the experimental results to the analytical method predictions, along the chute, in function of L/L_i . Noteworthy in this section is the difference between the empirical formulae by Meireles et al. [19] and the analytical method. Figure 2-6 showed the data the empirical formula was derived from and its inaccuracy in the region $L/L_i < 0.35$. The flow on Pedrógão dam spillway does not reach higher values of L/L_i at high unit discharge values. Therefore, the analytical prediction method will be used for comparison with the CFD simulations. The values in δ relative to the CFD simulations, for $L/L_i > 0.18$, show a practically constant trend.

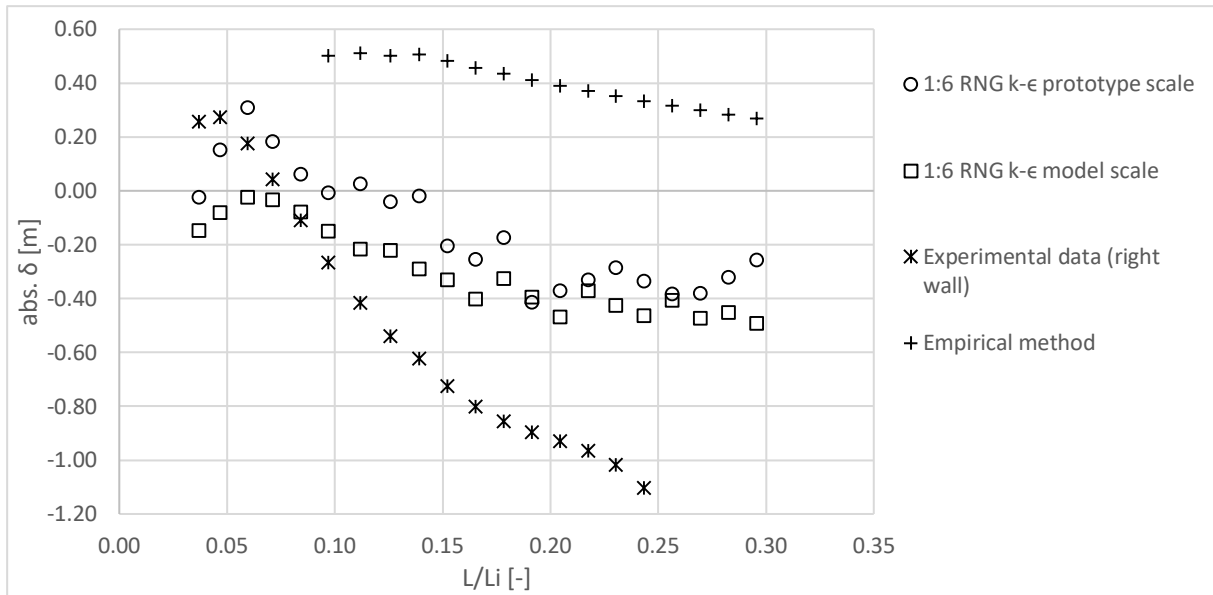


Figure 5-6 Flow depth differences, analytical formulae versus CFD simulation, empirical formulae and experimental data, in function L/L_i

Looking at the evolution of the velocity profiles for the 1:6 RNG k- ϵ simulation, Figure 5-7 shows the velocity profile above step 1 ($L/L_i = 0.037$) perpendicular to the pseudo-bottom. Plotted are the velocity profiles for the 1:3 and 1:6 RNG k- ϵ simulation, in function of the distance to the pseudo-bottom. It shows the small impact of CFD simulation mesh size, except close to the pseudo-bottom.

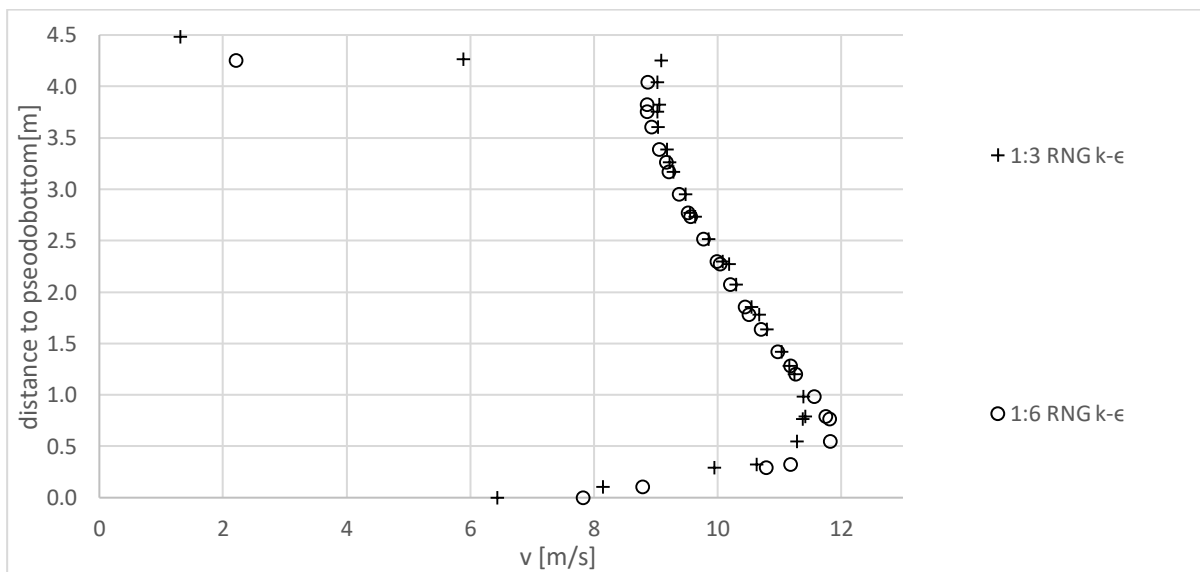


Figure 5-7 Velocity profiles at step 1 ($L/L_i = 0.037$)

The velocity profiles near $L/L_i = 0.2$ region evolve to the known free flow shape. This is shown in Figure 5-8 where the velocity distributions for steps 7-10 are plotted in function of the distance to the pseudo-bottom. Step 9, where $L/L_i = 0.139$, is the first step which shows a velocity distribution typical of the flow in the chute region, as talked about in 2.3.3. Considering the converging δ correlating with the shift in boundary layer shape, it leads to a possible misrepresentation of the boundary layer by the CFD simulation or the analytical method used to predict the flow depth.

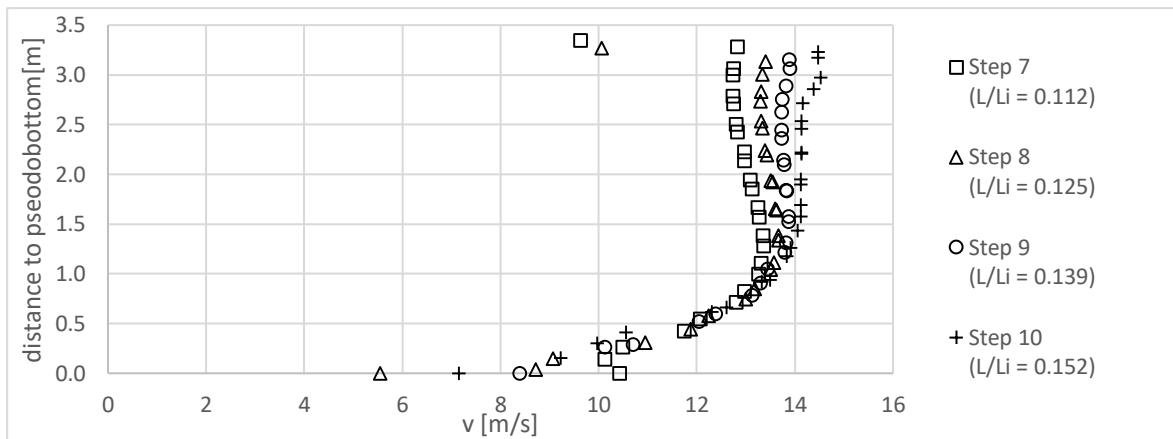


Figure 5-8 Velocity profiles for 1:6 RNG $k-\epsilon$ ($L/L_i = 0.112 - 0.152$)

5.3 Flow depths on the roller bucket

The roller bucket is a turbulent flow region with oscillation in the free surface elevation as talked about in section 4.2.4. Figure 5-9 gives an overview of the different free surface-elevations plotted in function of the x development and the bottom surface, all flow depths are in relation to. The oscillation in flow depth is indicated at the roller bucket and at the surge and roller location with their minimal and maximal values, for the experimental model values only. Comparing the flow depths of the experimental values to the CFD simulations shows slightly lower flow depths for the simulations. Considering the indicated oscillation of the experimental values the CFD simulations are well within the range of the experimental flow depths, in the roller area, and the model scale simulation in the surge area.

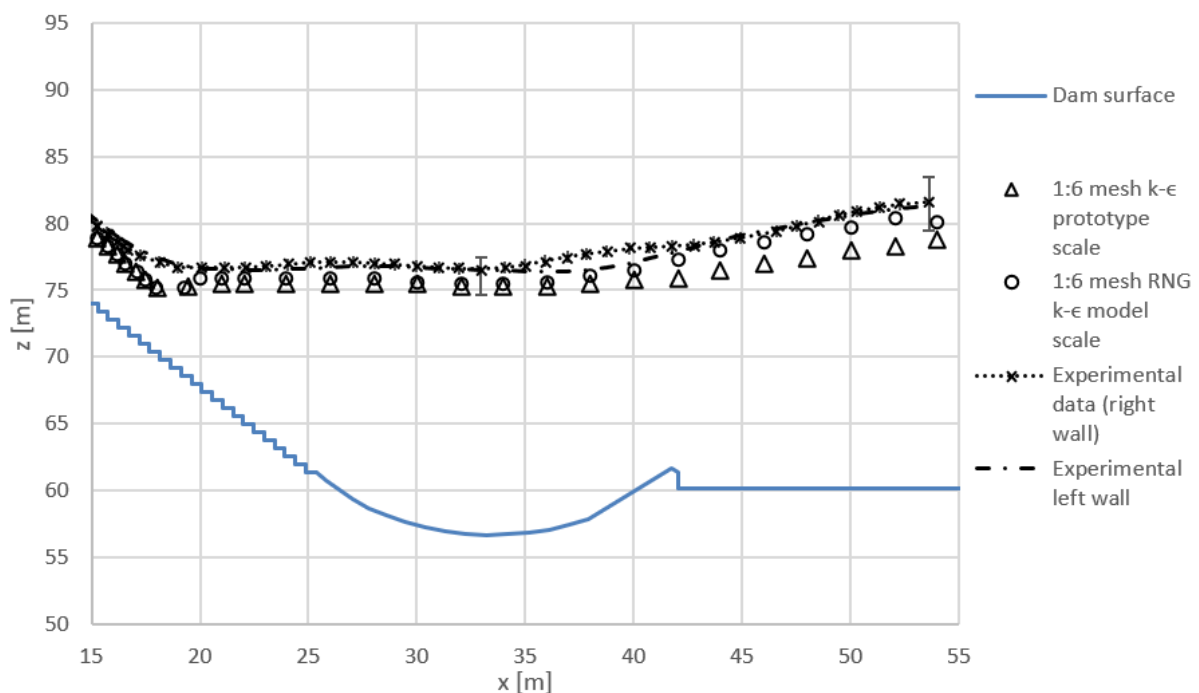


Figure 5-9 Free surface elevation on the roller bucket, Experimental and CFD, scale and full scale, data

The general shape of the flow is easily recognizable and the average and maximum relative difference in flow depths are as shown in Table 5-2.

Table 5-2 Flow depth in the roller bucket: avg. $\delta\%$ and max. $\delta\%$, compared with experimental results

Flow depth in the roller bucket	avg. $\delta\%$	max. $\delta\%$
Experimental to 1:6 RNG $k - \epsilon$ model scale	5.58	8.86
Experimental to 1:6 RNG $k - \epsilon$ prototype scale	10.05	14.07

The simulation at 1:65 model scale is generally closer to the experimental values, which further enforces the issue of scaling effects in simulations. Figure 5-10 shows the $\delta\%$ abs. evolution in function of the roller bucket region in comparison to the experimental results. The evolution of $\delta\%$ abs. in scale does not have a clear converging or diverging trend.

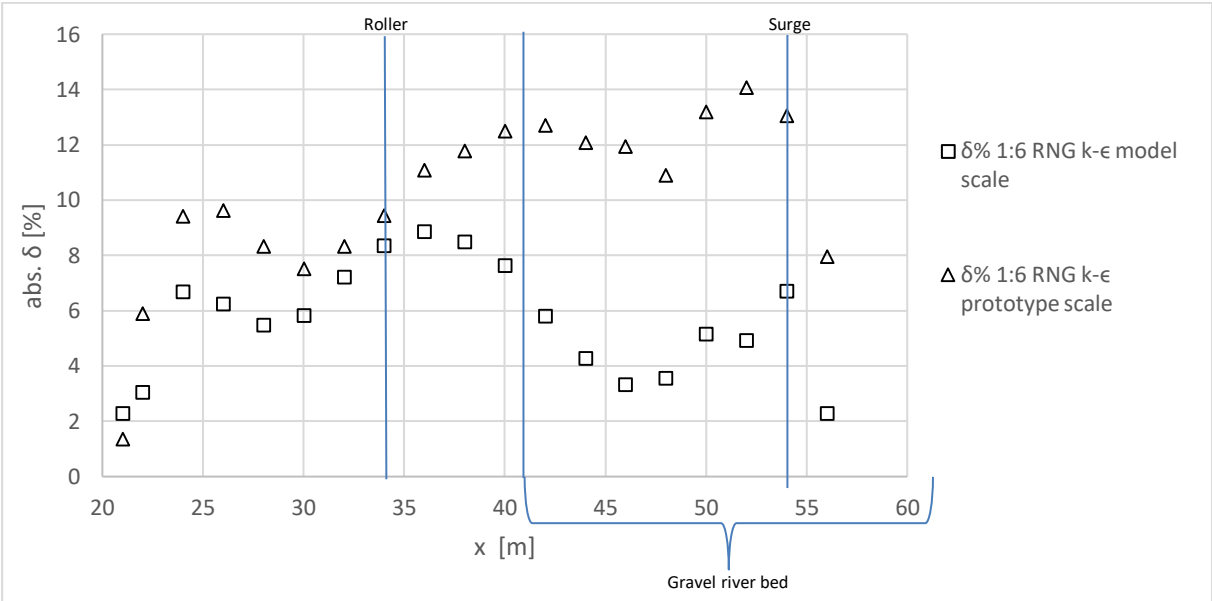


Figure 5-10 Flow depth relative differences along the roller bucket with experimental right wall as baseline data

The experimental study by LNEC included a gravel river bed downstream of the roller bucket which acquired a wavy pattern due to impact of the flow at the toe of the spillway. This wavy pattern is shown in Figure 5-11, the pike of the pattern is located at measurement $x = 46$ m in the simulation environment. To be able to match the experimental results with a CFD simulation this riverbed deformation has to be incorporated in the simulation environment or be simulated as well. Flow 3D[®] would offer an option to simulate the scour movement. This opens up new ways of improving CFD simulations by incorporating environmental change like this riverbed scour, but has not been done in this thesis, due to time and computational power constraints.

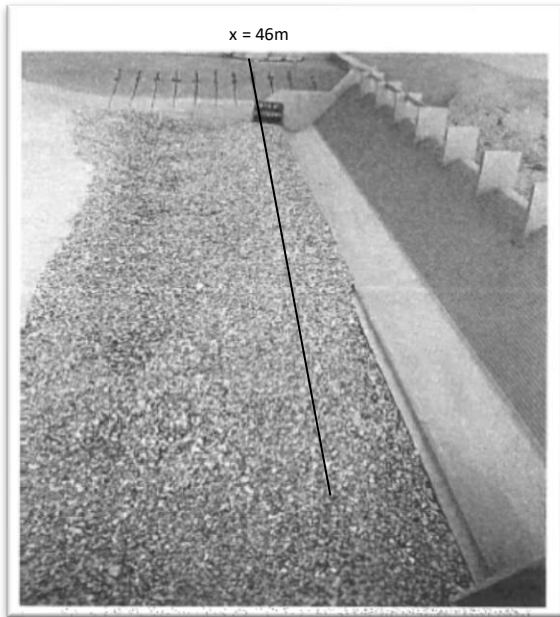


Figure 5-11 Riverbed deformation and scour documentation after a test run for $Q=12000 \text{ m}^3 \text{ s}^{-1}$ adapted from [34]

The second set of comparisons between experimental results and simulations at a discharge of $7000 \text{ m}^3 \text{ s}^{-1}$ showed increased discrepancies, between the experimental results and the simulation, as shown in Table 5-3. The general behaviour of the simulations remains the same as the $12000 \text{ m}^3 \text{ s}^{-1}$ comparison, with regards to neglected bulking and not consideration of the changes in the river bed due to scour.

Table 5-3 Flow depth relative differences in the roller bucket compared to experimental data, for $Q = 7000 \text{ m}^3 \text{ s}^{-1}$

Flow depth in the roller bucket	avg. δ [%]	max δ [%]
Experimental right wall to 1:6 RNG prototype scale	20.08	24.79
Experimental right wall to 1:6 RNG model scale	13.59	20.80

The visual comparison of the free surfaces in the roller bucket for the $7000 \text{ m}^3 \text{ s}^{-1}$ is shown Figure 5-12. The drawn free surface elevation for the physical model [34] seems to be on the high end of the spectrum, considering the oscillation indication given for the roller and the surge height. The simulations do not predict flow depths well in the roller bucket reach. The available data and comparative analysis did not evidence a clear reasoning for this increase in discrepancy.

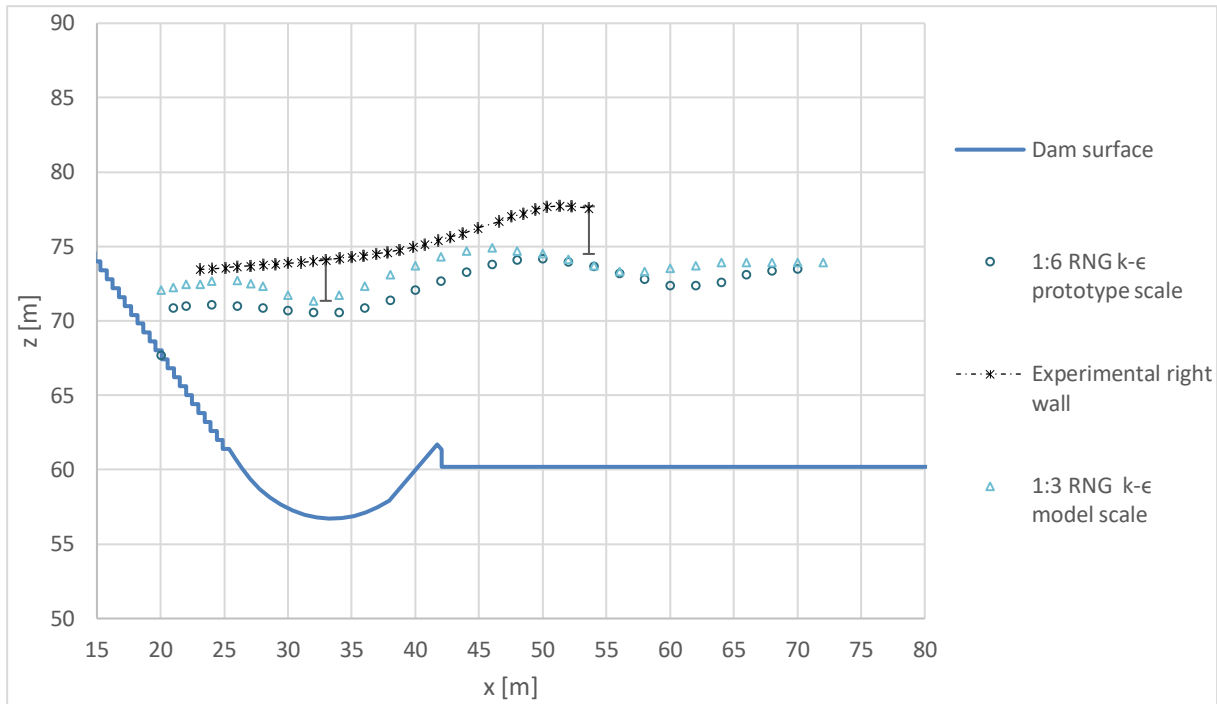


Figure 5-12 Free surface elevation on the roller bucket, for $Q=7000m^3s^{-1}$

5.4 Pressure heads at the ogee crest and roller bucket

Figure 5-13 displays the pressure head evolution along the line probe. Along with the pressure evolution are marked the pressure head values of the experimental results of LNEC [34]. The experimental values roughly match the simulation values. The last value is located at an x/z coordinate set which would be located in the middle of the flow, because the line probe in FlowSight reaches longer than the ramp. Figure 4-9 shows the position of the line probe, in section 4.7.3. The piezometer was located at the tip of the ramp. This has to be taken into account and considered while comparing the results. This shows that the result of the CFD simulation at 42.6 m should be compared to the experimental pressure value at 42,65 m. This is a very important factor to consider and is largely related to the usage of averages over a full mesh cell, the cell to compare might not be the cell in the exact same position, as the pressure tap in the physical model. This can be due to the averaging of not desired pressure regions, or the shift in position of the solid edge due to the FAVOR solid recognition algorithm talked about in section, 4.7.3 and specifically the explanatory Figure 4-12. The marked experimental values are the pressure taps 6,7 and 8. The pressure taps are marked at their specific x coordinate values, provided by drawings in the LNEC report shown in Figure B-3 of the Appendix B [34].

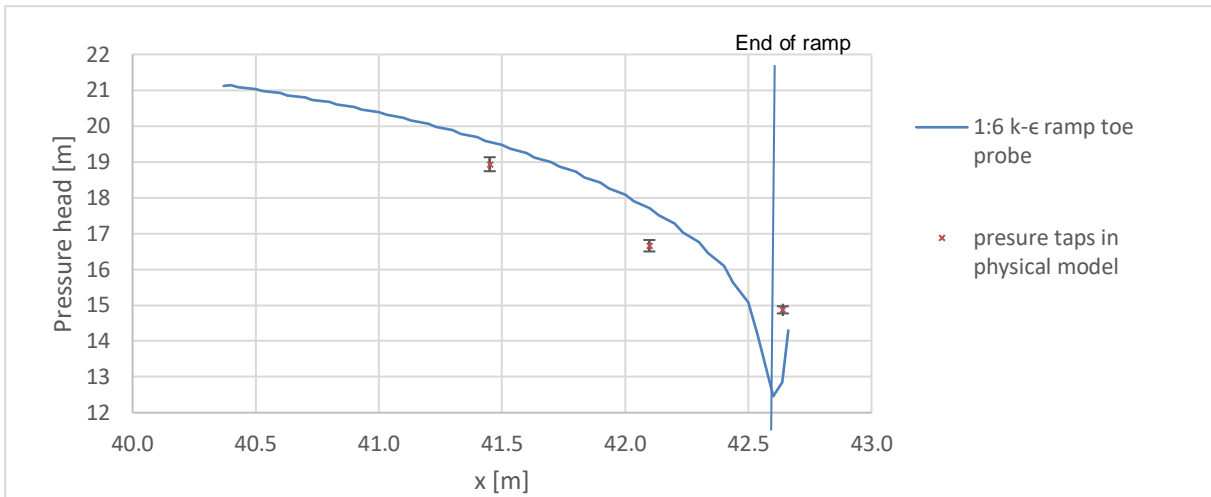


Figure 5-13 Pressure head development along the ramp of the roller bucket, comparison of CFD simulation with experimental data at pressure taps number 6, 7 and 8, with oscillation indication

The pressure head results of the experimental study by LNEC [34] showed fluctuation and therefore are documented as ranges. Figure 5-14 shows both maximum and minimum of the experimental values, together with the actual flow depth above the probe and the pressure head data of different mesh sizes.

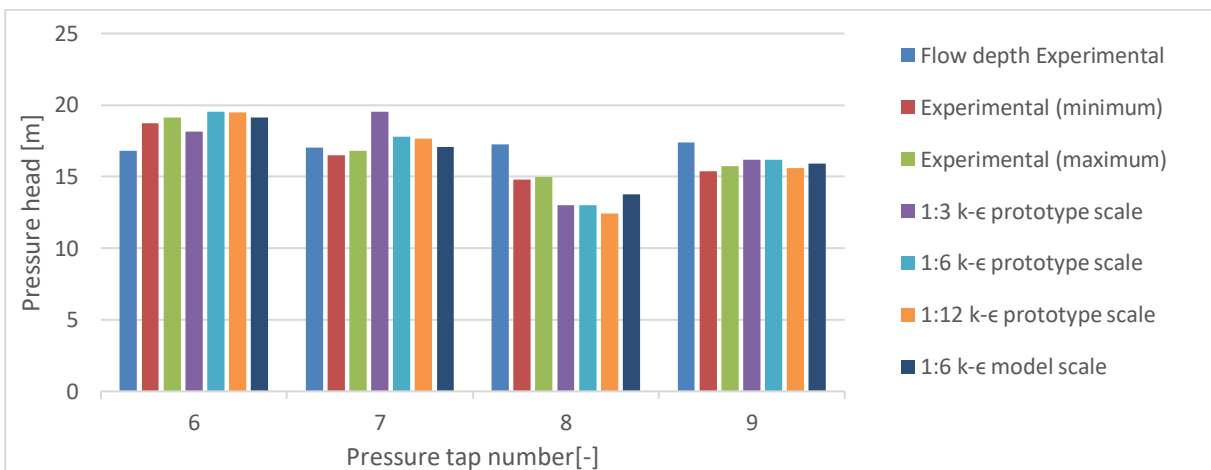


Figure 5-14 Pressure head and flow depth along the ramp of the roller bucket

The pressure head values are within the ranges of the experimental values Figure 5-15 shows the $\delta\%$ as evolution over the different probes. In the roller bucket region the scale simulation stays within about 10% deviation compared to the experimental values. All simulations have the same relative pressure trends as the experimental values, therefore the simulation values can be seen as good estimates.

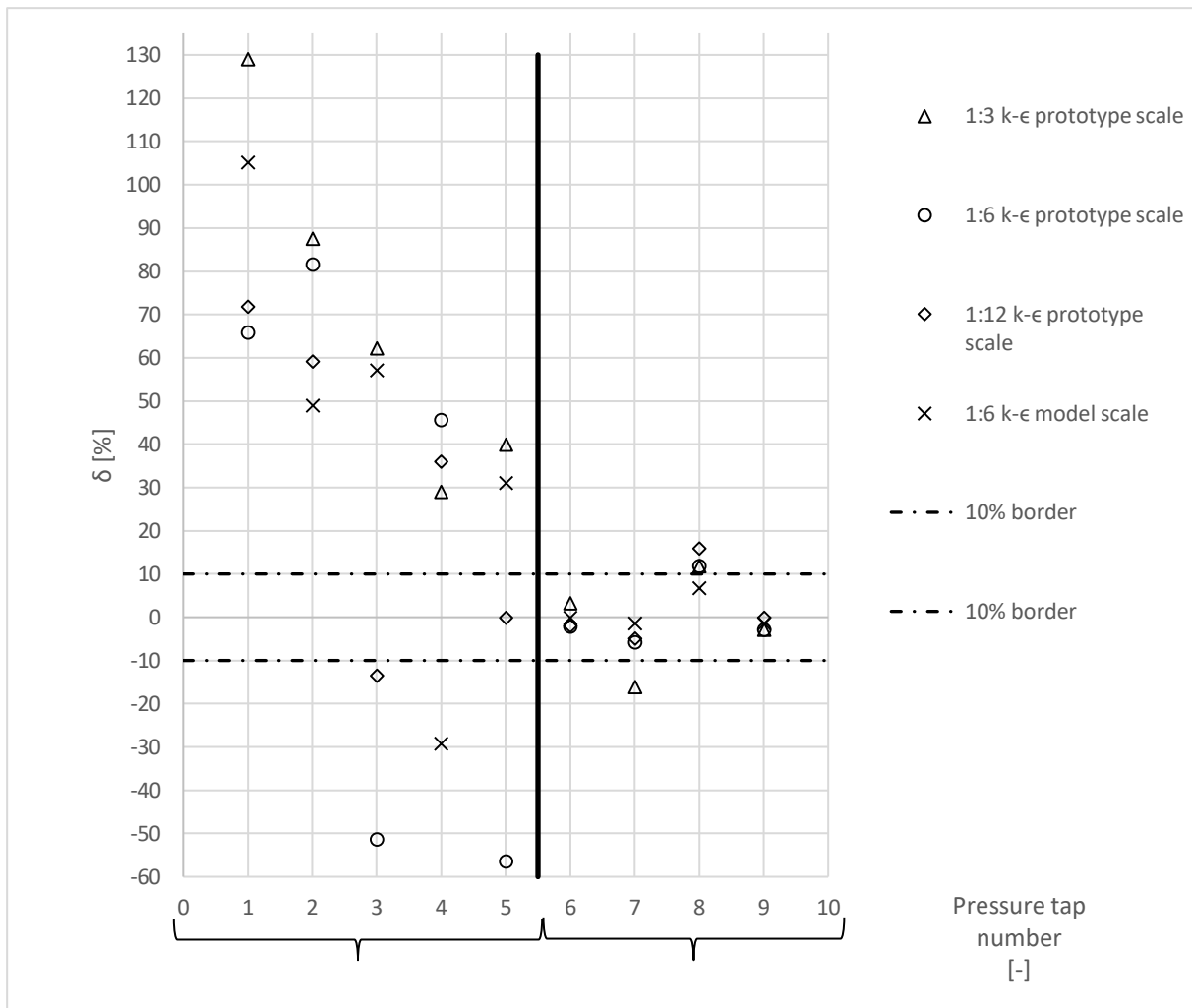


Figure 5-15 Pressure head differences compared to model values in %, ordered by pressure tap number

Similarly as for the crest region the $\delta\%$ shown in Figure 5-15 are very high, also showing a strong connection to mesh size. This seems largely related to the averaging of pressure values over a cell. The pressures in the crest region are very sensitive to location in the CFD simulation, which is also the case for physical models. In the CFD simulation a big issue is the representation of the boundary layer and accurate representation of the crest. The pressure evolution over the boundary layer is substantial and will be averaged over the mesh size. This is verified by the obvious trend of the pressure values with increasing crest length towards the experimental results (crest region). With the development of the boundary layer, it can be concluded that the pressure values of the CFD simulation tends towards those of the experimental data. Figure 5-16 shows the absolute values of the different mesh sizes at the probe locations in the crest area. Considering that the mesh size 1:3 k-ε shows positive relative pressures where negative relative pressures were to be expected, it is not suited for pressure analyses in the crest region. The higher mesh sizes predict the correct relative pressures, but the minimal pressure deviation is 11% and reaches upwards 100%, excluding probe 5 mesh size 1:12. All mesh sizes cannot be considered fine enough to predict accurately pressure head in the ogee crest region.

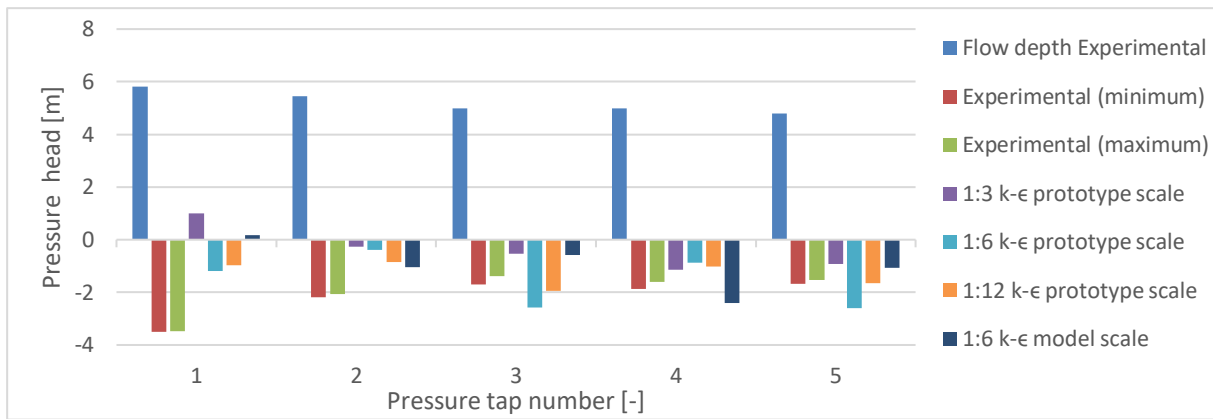


Figure 5-16 Pressure head and flow depth in the ogee crest region

When considering the pressure distribution at the crest the gradients seem to be too large to be handled by the executed simulations. Figure 5-17 shows the pressure distribution at the crest in the 1:12 k-ε simulation, which is the smallest of the executed simulations. The possible data points of the simulations are in the centre of each cell marked in the figure. The visible variations need to be taken into account which is why the probes have to be positioned manually to be comparable to pressure taps.

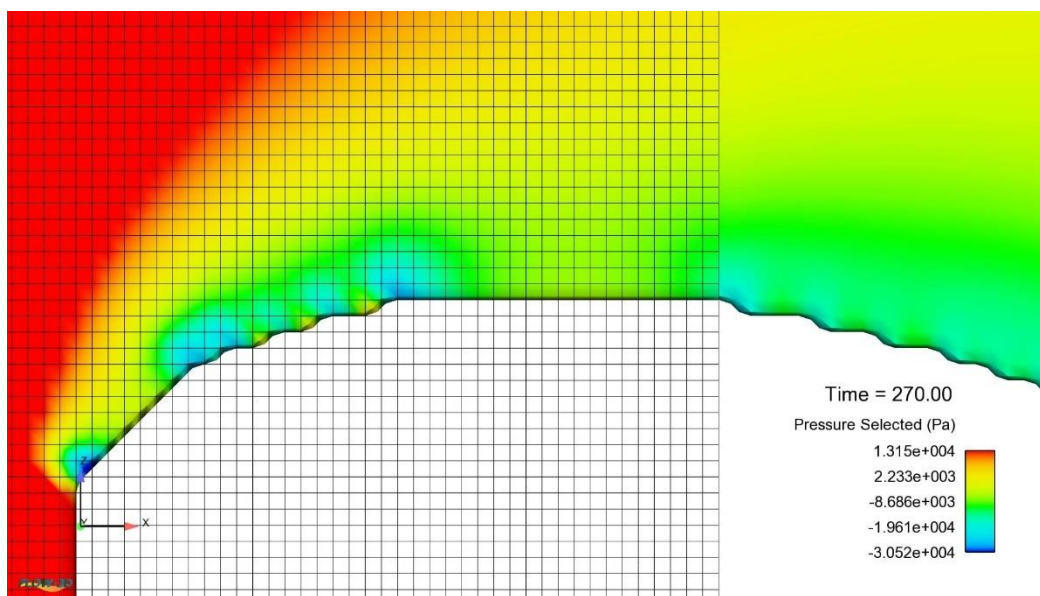


Figure 5-17 Pressure distribution isometric colouring view at the crest in the 1:12 k-ε simulation, with gridlines

For a good representation of a delicate shape as the ogee crest finer meshes would be required or a new approach has to be found.

Chapter 6

Conclusions and outlook

6.1 Concluding remarks

A numerical study of the flow over Pedrógão dam spillway and roller bucket using the Computational Fluid Dynamics software code FLOW-3D[®] was undertaken.

When comparing the different regions of the CFD simulation with the experimental results and the empirical predictions, the mesh size convergence is usually evaluated based on a chosen parameter. A closer look into the different parameters, show there is a need for more specific or individual mesh size convergence analyses. The ramp of the roller bucket seemed to converge in its results in the range of the 1:6 mesh size, as shown in Figure 5-15. However, the crest region did not show convergence for the analysed mesh sizes, as also shown in Figure 5-15. This confirms that different geometrical shapes require different mesh sizes to be accurately modelled. In the chute region, the flow depth and the velocity profiles converged to a satisfactory level for the 1:6 mesh size, shown in section 5.2. In turn, the flow on the roller bucket showed consistent mesh convergence over all analysed mesh sizes and

therefore the 1:3 mesh size would be sufficient.

In general, the flow was qualitatively represented quite well for all mesh sizes and models. The model scale simulation showed generally better agreement with the experimental data, as one would expect, due to small physical model geometrical scale (1:65) and its inherent scale effects. These results suggest that scaling effects in CFD should be looked at in a deeper way, in future studies.

A fair level of accuracy of the pressure head in the crest region was not reached, due to the lack of appropriate mesh convergence. In fact, the CFD results showed a poor agreement with the experimental data (Figure 5-15). In the roller bucket ramp region, accuracy within 10% of the experimental values was achieved. The pressure head development along the crest (Figure 4-11) showed clearly the uncertainties of the pressure head, which was further shown by the isometric distribution (Figure 5-17). A solution to this problem may lie in looking at the pressure development in the isometric overview, such as in Figure 5-17, and manually position the probe at the desired location. This includes vertical variation, to prevent averaging of solid structure pressures into the fluid pressures, as shown in Figure 4-12.

In the chute reach, the flow depths of the CFD simulations were, on average, within 12% for the full-scale simulation (1:6 RNG k- ϵ), whereas the equivalent scaled CFD simulations were limited to approximately 10% (Table 5-1). An ongoing extensive study on scaling effects in CFD simulation of spillway chutes downstream of labyrinth weirs by Torres [38] showed average flow depth variations between 14 to 18% (for low flow rates) and 4 to 6% (for high flow rates). These comparisons were between same scale experiments and CFD simulations and no bulking effects were included. This shows that the general results of this thesis are in the same accuracy range, considering dissimilar scale comparisons and not accounted bulking effects. Also, it reinforces the interest on CFD scaling experiments in stepped spillway applications.

When considering the evolution of the absolute deviation between the analytical method results and the CFD simulations along the chute, the absolute flow depth difference tends towards a constant value, for locations downstream of $0.18 L/L_i$ (Figure 5-6). At such location, the velocity profile seems no longer influenced by the entrance conditions (Figure 5-8). An interesting approach would be to compare a calibrated simulation for high L/L_i estimations to a crest estimation calibrated CFD simulation. This would require accurate model data for both regions with no bulking effects or other influences present.

The numerical results of the flow on the roller bucket were found to agree well with their experimental counterparts, in particular considering the constant river bed in the CFD simulations, compared to the changes in river bed observed on the physical model tests.

The accuracy on the roller bucket was, on average, 6% for the model scale simulation and 10 % for the full-scale simulation (Table 5-2). Considering the oscillation of the flow, the model scale simulation results are within the oscillation values documented in the model experiments, but in general the flow depths are slightly underestimated, probably due to bulking effects at the walls. The impact of the bulking should be estimated with experimental model or prototype data. Both were not available for this thesis and are mentioned in the outlook. The same goes for the scour at the river bed and for a 3-dimensional

simulation approach. To give precise numbers of the accuracy of the CFD simulations, these parameters would need to be included in the simulation or their impact on the simplified flow needs to be defined.

6.2 Outlook

There are various options on how to proceed with the analysis of the hydraulics of Pedrógão dam spillway and energy dissipator, and further improving the usefulness of the available model data. Free surface measurements of the flow on the prototype dam, would give the option to evaluate flow depths and bulking at the sidewalls. These flow depths could then be compared to those obtained from the respective CFD simulations. This would give good opportunities to analyse scale effects in CFD simulations, by calibrating both individually and comparing the calibrated parameters. Another good continuation would be simulations of the effects of scour in the river bed. For reliable scour simulations a 3-dimensional approach is necessary. The scour movement simulations could also be done between the model scale, full size dam, full size CFD and model scale CFD. This requires a good grasp on the scour simulation of Flow 3D[®] and appropriate computational power or time. This 4-way analyses could also be done on the pressure heads; this would require significant analyses on the mesh size, which might be one of the easiest variables to vary. A focus could be on crest representation and same scale simulation focused on high L/L_i representation to compare each other calibration values and derive conclusions from that. A suggestion to automate the boundary layer recognition, as per the simple code listed in Appendix H, could be used for further analyses in the boundary layer CFD representation. This improvement should have significant impact on the pressure head estimation at the crest. A solution for accurate distribution could be assessed, for example necessary mesh resolution, an additional model in the crest region or even a new boundary condition for this specific application. The pressure head prediction along the crest is one of the most important regions where accurate predictions are necessary, to enable maximum usage out of a dam without risk of cavitation at the crest. To expand the capacity of the Pedrógão dam reservoir could be of potential interest for the future. First possible solutions brought up could be installing gates on the top of the dam. A higher upstream water depth would increase the storage capacity and would increase the risk of cavitation due to higher velocities at the crest, therefore potential solutions would need significant testing and planning. Another variable to be considered in future work would be the impact of the piers splitting the crest of Pedrógão dam. These piers have been neglected in this work due to the 2-dimensional assumption but need to be considered when setting up for design relevant supporting CFD simulations. In the case of an actual experimental model campaign, the installation of sensors in sensitive areas for CFD simulations should be considered. This could be a unique opportunity to complement the experimental model data acquired in the previous LNEC study and to expand on the available discharge datasets for extensive calibration and testing of the quality of CFD simulations using Flow 3D[®].

References

- [1] C. Zarfl, A. E. Lumsdon, J. Berlekamp, L. Tydecks and K. Tockner, "A Global Boom in Hydropower dam Construction," *Aquatic Sciences*, pp. 1-11, 8 October 2014.
- [2] The US Bureau of Reclamation, "Appurtenant Structures for Dams (Spillways and Outlet Works) Design Standard," The Bureau of Bureau of Reclamation, 2014.
- [3] J. F. Ruff and J. P. Ward, "Hydraulic Design of Stepped Spillways," Final Report: Research Project 99FC800156 ,U.S. Bureau of Reclamation, Denver, Colorado, 2002.
- [4] H. Chanson, "Melton Dam Overflow Stepped Spillway, Australia," 2000. [Online]. Available: <http://staff.civil.uq.edu.au/h.chanson/pictures/melton2a.jpg>.
- [5] J. Matos and I. Meireles, "Hydraulics of Stepped Weirs and Dam Spillways: Engineering Challenges, Labyrinths of Research," in *5th International Symposium on Hydraulic Structures*, Brisbane, Australia, 2014.
- [6] F. A. Bombardelli, I. Meireles and J. Matos, "Laboratory Measurements and Multi-Block Numerical Simulations of the Mean Flow and Turbulence in the Non-Aerated Skimming Flow Region of Steep Stepped Spillways," *Environ Fluid Mech*, pp. 263-288, 26 June 2011.
- [7] H. Chanson, "Prediction of the Transition Nappe/Skimming Flow on a Stepped Channel," *Journal of Hydraulic Research*, vol. 34, no. 3, pp. 421-429, 1996.
- [8] W. K. Frizell and K. H. Frizell, "Guidelines for Hydraulic Design of Stepped Spillways," U.S. Department of the Interior Bureau of Reclamation, Denver, Colorado, 2015.
- [9] M. Lejeune and A. Lejeune, "About the Energy Dissipation of Skimming Flows Over Stepped Spillways," in *1st International conference, Hydroinformatics*, Delft, Netherlands, 1994.
- [10] M. Bindo, J. Gautier and F. Lacroix, "The Stepped Spillway of M'Bali Dam," *International Water Power and Dam Construction*, vol. 45, pp. 35-36, January 1993.
- [11] R. M. Chamani and N. Rajaratnam, "Jet Flow on Stepped Spillways," *Journal of Hydraulic Engineering*, vol. 120, no. 2, pp. 254-259, 2. Febuary 1994.

- [12] H. Chanson and C. A. Gonzalez, "Hydraulic Design of Stepped Spillways and Downstream Energy Dissipators," *Dam Engineering*, vol. XI, pp. 205-242, 2001.
- [13] S. André, "High velocity aerated flow on stepped chutes with macro-roughness elements," PhD Thesis, EPFL, Lausanne, Switzerland, 2004.
- [14] J. Matos and A. Quintela, "Discussion of Jet Flow in Stepped Spillways by Chamani, M.R. and Rajaratnam, N.," *Journal of Hydraulic Research*, vol. 120, no. 2, pp. 443-444, 1995.
- [15] K. H. Frizell, "Hydraulics of Stepped Spillways for RCC Dams and Dam Rehabilitations," Project Report: PAP- 596 San Diego, USA, 1992.
- [16] A. C. Gonzalez and H. Chanson, "Interactions Between Cavity Flow and Main Stream Skimming Flows," *Canadian Journal of Civil Engineering*, vol. 31, no. 1, pp. 33-44, 2004.
- [17] H. Chanson, "Hydraulics of Stepped Chutes and Spillways," Balkema, Lisse, Netherlands, 2002.
- [18] A. Amador, M. Sánchez-Juny and J. Dolz, "Developing Flow Region and Pressure Fluctuations on Steeply Sloping Stepped Spillways," *Journal of Hydraulic Engineering*, vol. 135, no. 12, pp. 1092-1100, 2009.
- [19] I. Meireles, F. Renna, J. Matos, F. Bombardelli and A. M. ASCE, "Skimming, Nonaerated Flow on Stepped Spillways over Roller Compacted Concrete Dams," *Journal of Hydraulic Engineering*, vol. 138, no. 10, pp. 870-877, October 2012.
- [20] H. Ramos, A. Betâmio de Almeida, M. M. Portela and H. Pires de Almeida , "Guidelines for Design of Small Hydropower Plants", 1st ed., Belfast, North Ireland: Western Regional Energy Agency & Network, 2000.
- [21] D. Kositgittiwong, "Validation of Numerical Model of the Flow Behaviour Through Smooth and Stepped Spillways Using Large-Scale Physical Model," PhD Thesis, King Mongkut's University of Technology Thonburi, Thonburi, 2012.
- [22] H. Schlichting, K. Gersten, "Boundary-Layer Theory", 9th ed., Heidelberg: Springer- Verlag Berlin Heidelberg, 2017.
- [23] Flow Science Inc., "Flow3D User Manual," 2012.
- [24] C. Gualtieri, A. Angeloudis, F. Bombardelli, S. Jha and T. Stoesser, "On the Values for the Turbulent Schmidt Number in Environmental Flows," *MDPI Fluids*, vol. 2, pp. 1-27, 17 April 2017.

- [25] C. W. Hirt and B. D. Nichols, "Volume of Fluid (VOF) Method for the Dynamics of free Boundaries," *Journal of Computational Physics*, vol. 39, no. 1, pp. 201- 255, 1 November 1981.
- [26] Flow Science Inc., User Manual Flow 3D, Santa Fe, 2000.
- [27] M. H. Boyaghchi, S. Fard and F. A., "Studies of the Influence of Various Blade Outlet Angles in a Centrifugal Pump when Handling Viscous Fluids," *American Journal of Applied Sciences*, vol. 4, no. 9, pp. 718-724, January 2007.
- [28] F. Harlow and J. Welch, "Numerical Calculation of Time-Dependent Viscous Incompressible Flow," *Physics of Fluids*, vol. 8, 1965.
- [29] B. E. Launder and D. B. Spalding, "The Numerical Computation of Turbulent Flows," *Computer Methods in Applied Mechanics and Engineering*, vol. 3, no. 2, pp. 269-289, 1974.
- [30] W. Rodi, "Turbulence Models and their Application in Hydraulics: A state-of-the-art review," *IAHR Monograph*, June 1980.
- [31] V. Yakhot and S. Orszag, "Renormalization Group Analysis of Turbulence. I. Basic Theory," *Journal of Scientific Computing*, vol. 1, no. 1, pp. 3-51, March 1986.
- [32] V. Yakhot and L. Smith, "The Renormalization Group, the ϵ -Expansion and Derivation of Turbulence Models," *Journal Scientific Computing*, vol. 7, no. 1, pp. 35-61, March 1992.
- [33] EDIA, "Alqueva project, Empresa de Desenvolvimento e Infra-estruturas do Alqueva, S.A.," 2013. [Online]. Available: <http://www.edia.pt/en/alqueva/multiple-purposes/187>. [view in 25-08-2018].
- [34] J. Melo, "Barragem de Pedrógão. Estudo em Modelo Reduzido do Descarregador de Cheias e da Descarga Auxiliar," NRE, LNEC, Lisbon, 2003.
- [35] U.S. Army Corps of Engineers, "Hydraulic Design Criteria," 1973.
- [36] J. Lira, *Official drawing no. 00606*, Barragem: Hidrorumo, EDP, 1999.
- [37] I. Otic, "CFD Simulation for Power Engineers," Karlsruhe Institut für Technology, Karlsruhe, 2016.
- [38] C. Torres, D. Borman, A. Sleigh and D. Neeve, "Determination of Scale Effects for a Scaled Physical Model of a Labyrinth Weir Using CFD," in *7th International Symposium on Hydraulic Structures*, Aachen, Germany, 2018.
- [39] R. M. Boes, W. H. Hager, "Two-Phase Flow Characteristics of Stepped Spillways," *Journal of*

Hydraulic Engineering, vol. 129, no. 9, pp. 661- 670, September 2003.

- [40] L. B. a. H. I. T. Theofanous, "A Theoretical Study on Bubble Growth in Constant and Time-Dependent Pressure Fields," *Chemical Engineering Science*, vol. 24, no. 5, pp. 885- 897, May 1969.
- [41] F.H. Harlow and P.I. Nakayama, "Turbulence Transport Equations," *Physics of Fluids*, vol. 10, pp. 2634-2649, 1967.
- [42] H. Chanson, "Stepped Spillway Flows and Air Entrainment," *Canadian Journal of Civil Engineering*, vol. 20, no. 3, pp. 422-435, June 1993.

Appendix A. Simulation result tables

Table A-1 Flow depth on the chute overview by steps for the prototype scale mesh sizes and turbulent models

Step No.	L/Li	1:12 k-e	1:6 k-e	δ abs.	δ	1:3 k-e	δ abs.	δ	1:3 RNG	δ abs.	δ	1:6 RNG	δ abs.	δ
[-]	[-]	[m]	[m]	[m]	[%]									
1	0.037	4.26	4.26	-4.32E-04	1.01E-02	4.70	-4.38E-01	1.03E+01	4.70	-4.38E-01	1.03E+01	4.26	-4.32E-04	1.01E-02
2	0.047	4.08	4.13	-5.66E-02	1.39E+00	4.26	-1.82E-01	4.47E+00	4.47	-3.96E-01	9.72E+00	4.13	-5.66E-02	1.39E+00
3	0.059	3.89	3.96	-6.79E-02	1.75E+00	4.19	-3.06E-01	7.86E+00	4.19	-3.06E-01	7.86E+00	3.96	-6.79E-02	1.75E+00
4	0.071	3.78	3.89	-1.14E-01	3.02E+00	4.12	-3.44E-01	9.10E+00	4.12	-3.44E-01	9.10E+00	3.86	-8.44E-02	2.23E+00
5	0.084	3.71	3.71	-1.00E-06	2.70E-05	4.02	-3.12E-01	8.40E+00	4.02	-3.12E-01	8.40E+00	3.71	-1.00E-06	2.70E-05
6	0.097	3.61	3.68	-6.81E-02	1.89E+00	3.95	-3.41E-01	9.43E+00	3.95	-3.41E-01	9.43E+00	3.68	-6.81E-02	1.89E+00
7	0.112	3.49	3.49	5.00E-06	1.43E-04	3.86	-3.67E-01	1.05E+01	3.86	-3.67E-01	1.05E+01	3.49	5.00E-06	1.43E-04
8	0.125	3.43	3.43	0.00E+00	0.00E+00	3.81	-3.81E-01	1.11E+01	3.73	-2.98E-01	8.70E+00	3.43	0.00E+00	0.00E+00
9	0.139	3.30	3.38	-7.71E-02	2.34E+00	3.68	-3.85E-01	1.17E+01	3.68	-3.85E-01	1.17E+01	3.38	-7.71E-02	2.34E+00
10	0.152	3.36	3.36	0.00E+00	0.00E+00	3.75	-3.85E-01	1.15E+01	3.75	-3.85E-01	1.15E+01	3.36	0.00E+00	0.00E+00
11	0.165	3.27	3.35	-8.00E-02	2.45E+00	3.64	-3.71E-01	1.14E+01	3.64	-3.71E-01	1.14E+01	3.35	-8.00E-02	2.45E+00
12	0.178	3.19	3.19	-1.00E-06	3.14E-05	3.53	-3.49E-01	1.10E+01	3.53	-3.49E-01	1.10E+01	3.19	-1.00E-06	3.14E-05
13	0.191	3.19	3.19	0.00E+00	0.00E+00	3.51	-3.20E-01	1.01E+01	3.51	-3.20E-01	1.01E+01	3.19	0.00E+00	0.00E+00
14	0.204	3.11	3.19	-8.00E-02	2.58E+00	3.51	-4.00E-01	1.29E+01	3.51	-4.00E-01	1.29E+01	3.19	-8.00E-02	2.58E+00
15	0.217	3.04	3.10	-6.40E-02	2.11E+00	3.48	-4.48E-01	1.48E+01	3.48	-4.48E-01	1.48E+01	3.10	-6.40E-02	2.11E+00
16	0.23	3.03	3.03	-1.00E-06	3.31E-05	3.38	-3.55E-01	1.17E+01	3.38	-3.55E-01	1.17E+01	3.03	-1.00E-06	3.31E-05
17	0.243	2.95	3.02	-7.72E-02	2.62E+00	3.28	-3.33E-01	1.13E+01	3.28	-3.33E-01	1.13E+01	3.02	-7.68E-02	2.61E+00
18	0.256	2.92	2.92	4.00E-06	1.37E-04	3.19	-2.66E-01	9.10E+00	3.19	-2.66E-01	9.10E+00	2.92	4.00E-06	1.37E-04
19	0.269	2.87	2.87	0.00E+00	0.00E+00	3.19	-3.20E-01	1.12E+01	3.19	-3.20E-01	1.12E+01	2.87	0.00E+00	0.00E+00
20	0.282	2.78	2.84	-6.40E-02	2.30E+00	3.19	-4.07E-01	1.46E+01	3.19	-4.07E-01	1.46E+01	2.84	-6.40E-02	2.30E+00
21	0.295	2.79	2.87	-8.00E-02	2.87E+00	3.19	-4.00E-01	1.44E+01	3.19	-4.00E-01	1.44E+01	2.87	-8.00E-02	2.87E+00
22	0.309	4.05	4.05	2.00E-06	4.94E-05	4.05	2.00E-06	4.94E-05	4.30	-2.56E-01	6.33E+00	3.53	5.12E-01	1.27E+01
Average					1.15			10.30			10.72			1.69
Maximum					3.02			14.77			14.77			12.66

Appendix B. Probe positioning along the chute steps

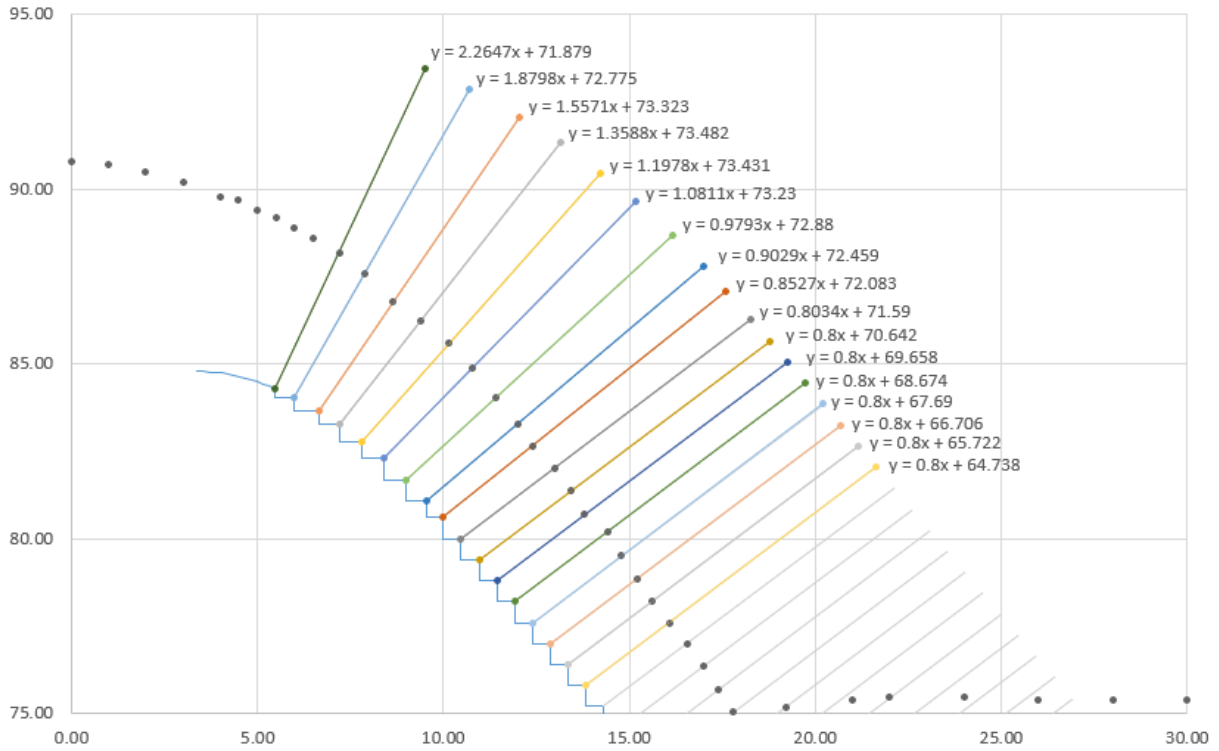


Figure B-1 Perpendicular step probes and their functions

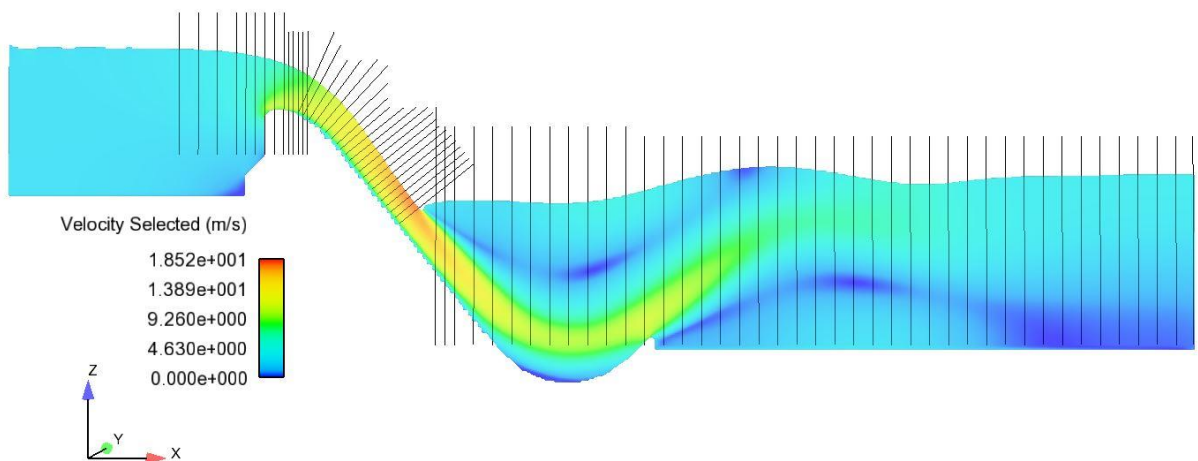


Figure B-2 All line probe positions in the simulated area

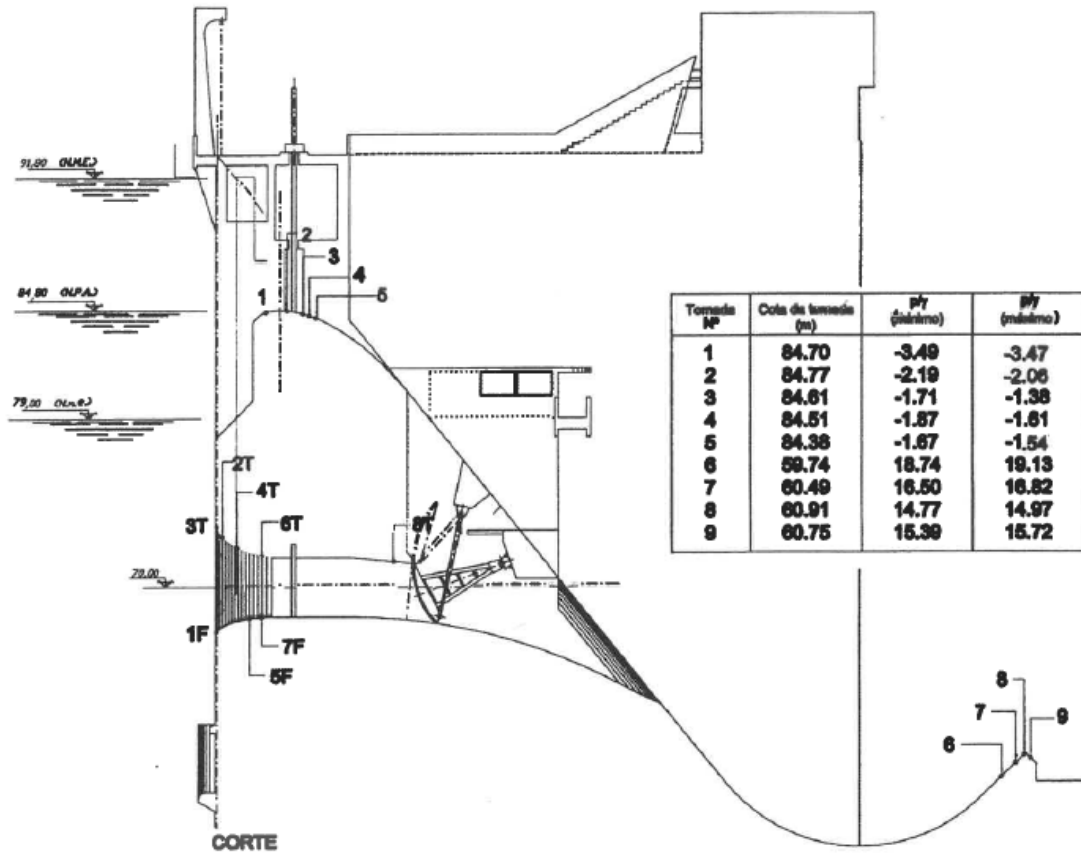


Figure B-3 Pressure tap location overview [34]

Table B-1 Coordinates of pressure taps

Pressure tap No.	X coordinates	Z coordinates
-	m	m
1	2.24375	84.5163
2	3.34297	84.8235
3	4.33451	84.7124
4	4.59198	84.6407
5	5.04658	84.4875
6	41.45	59.821
7	42.098	60.4416
8	42.64	61
9	42.9655	60.6949

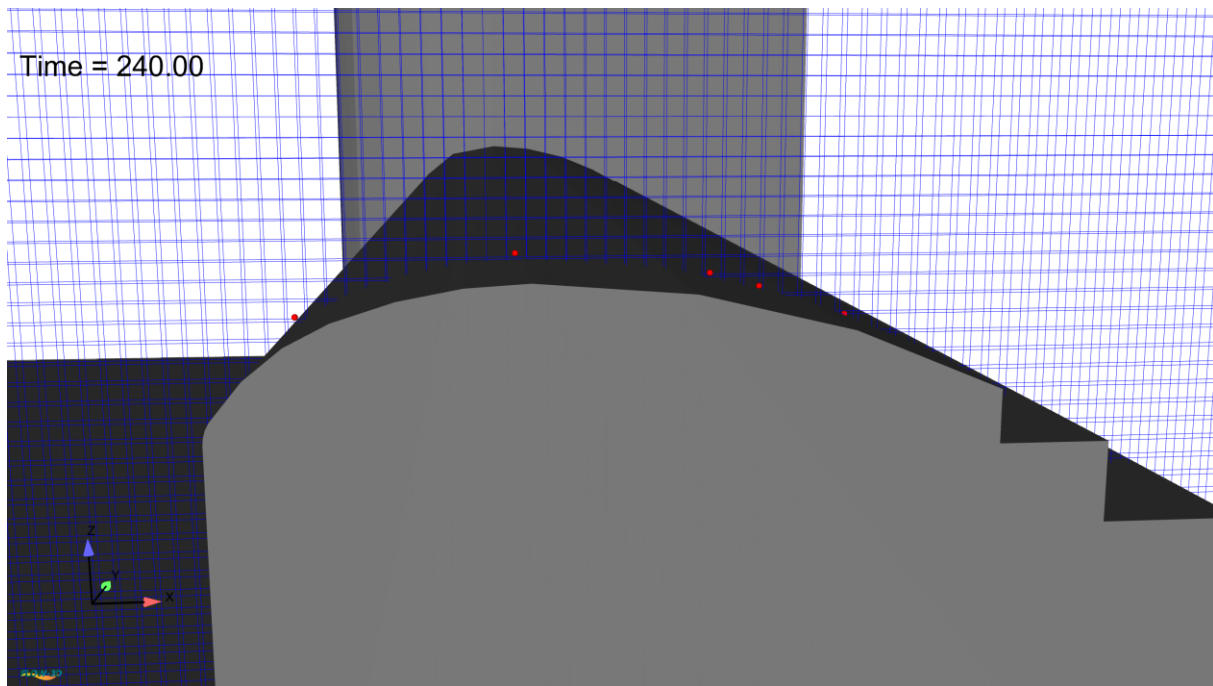


Figure B-4 Manually positioned pressure probes at the ogee crest (3D view)

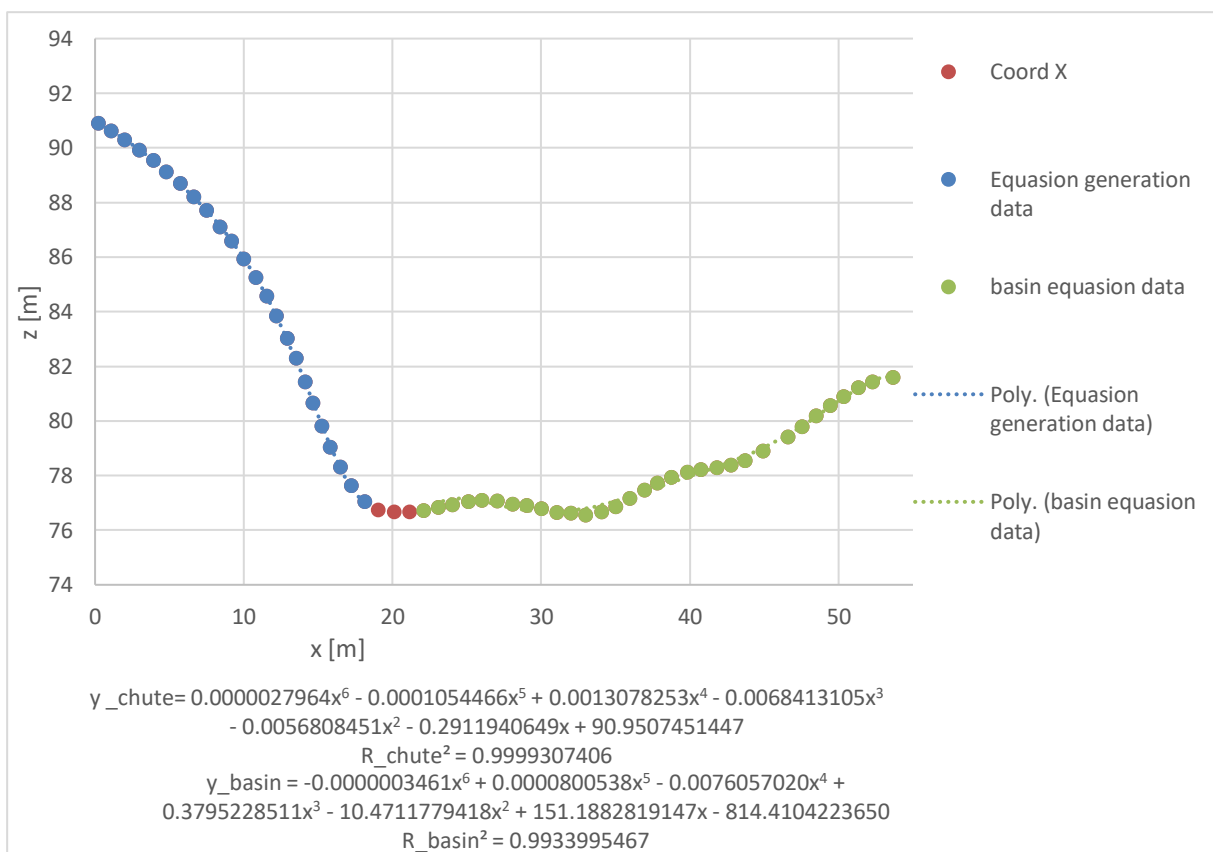


Figure B-5 Experimental free surface elevation on the right wall, for $Q = 12000\text{m}^3\text{s}^{-1}$

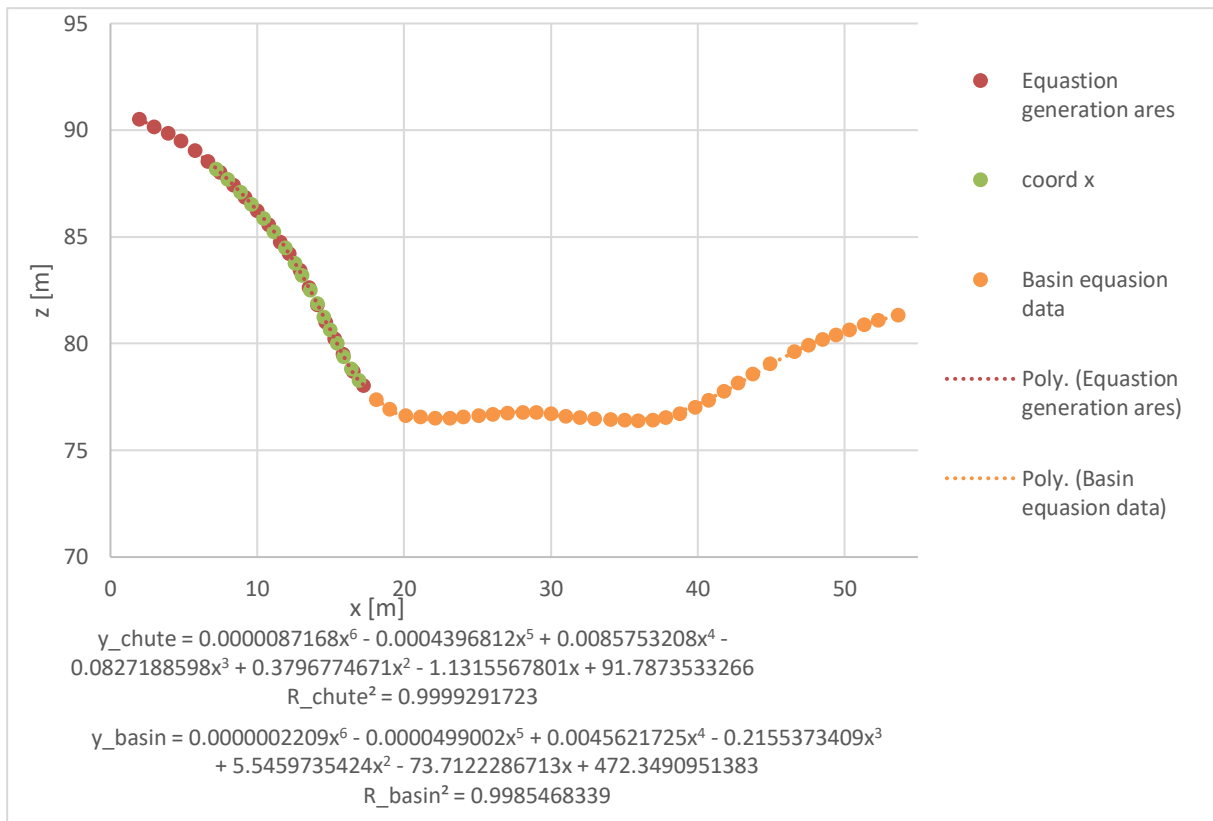


Figure B-6 Experimental free surface elevation on the left wall, for $Q = 12000\text{m}^3\text{s}^{-1}$

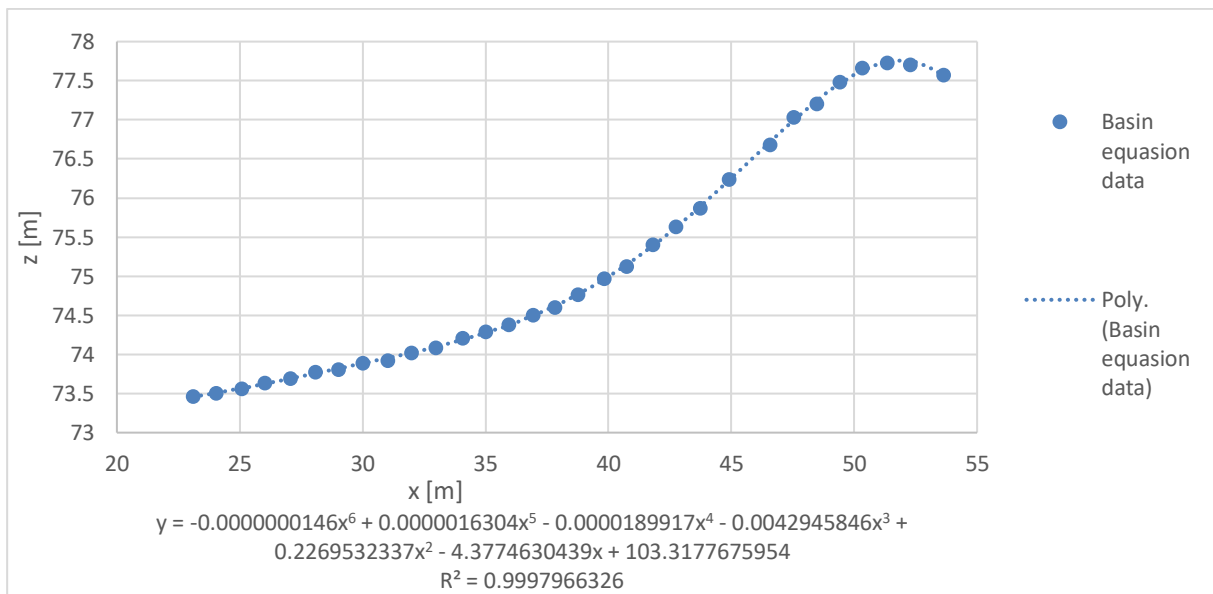


Figure B-7 Experimental free surface elevation on the right wall, for $Q = 7000\text{m}^3\text{s}^{-1}$

Appendix C. Export options for Stereolithography

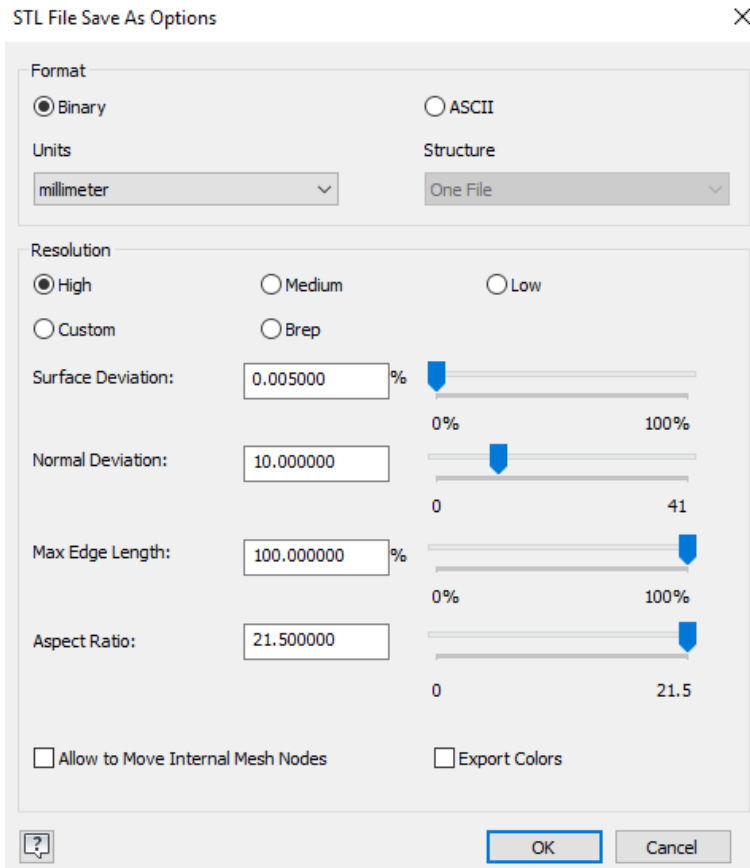


Figure C-1 Export options while saving Stereolithography file from inventor

Appendix D. Mesh block documentation

Table D-1 Individual mesh block data, mesh 1:3

Mesh outline block arrangement 1:3 prototype scale											
Mesh no.	x min	x max	y min	y max	z min	z max	Cell size	No cells x	No cells y	No cells z	Sum cells
[-]	[m]	[-]	[-]	[-]	[-]						
1	-25	0	1	1.2	75	95	0.2	125	1	100	12500
2	4	10	1	1.2	79	93	0.2	30	1	70	2100
3	20	40	1	1.2	55	83	0.2	100	1	140	14000
4	40	100	1	1.2	55	82	0.2	300	1	135	40500
5	10	15	1	1.2	73	90	0.2	25	1	85	2125
6	15	20	1	1.2	67	85	0.2	25	1	90	2250
7	0	4	1	1.2	77.5	95	0.2	20	1	87.5	1750
										Sum	75225

Table D-2 Individual mesh block data, mesh 1:6

Mesh block arrangement 1:6 prototype scale											
Mesh no.	x min	x max	y min	y max	z min	z max	Cell size	No cells x	No cells y	No cells z	Sum cells
[-]	[m]	[-]	[-]	[-]	[-]						
1	-25	0	1	1.1	75	95	0.1	250	1	200	50000
2	4	10	1	1.1	79	93	0.1	60	1	140	8400
3	20	40	1	1.1	55	83	0.1	200	1	280	56000
4	40	100	1	1.1	55	82	0.1	600	1	270	162000
5	10	15	1	1.1	73	90	0.1	50	1	170	8500
6	15	20	1	1.1	67	85	0.1	50	1	180	9000
7	0	4	1	1.1	77.5	95	0.1	40	1	175	7000
										Sum	300900

Table D-3 Individual mesh block data, mesh 1:12

Mesh block arrangement 1:12 prototype scale											
Mesh no.	x min	x max	y min	y max	z min	z max	Cell size	No cells x	No cells y	No cells z	Sum cells
[-]	[m]	[-]	[-]	[-]	[-]						
1	-25	0	1	1.1	75	95	0.1	250	1	200	50000
2	4	10	1	1.1	79	93	0.05	120	2	280	67200
3	20	40	1	1.1	55	83	0.05	400	2	560	448000
4	40	100	1	1.1	55	82	0.1	600	1	270	162000
5	10	15	1	1.1	73	90	0.05	100	2	340	68000
6	15	20	1	1.1	67	85	0.05	100	2	360	72000
7	0	4	1	1.1	77.5	95	0.05	80	2	350	56000
										Sum	923200

Table D-4 Individual mesh block data, mesh 1:6 model scale simulation

Mesh block arrangement 1:6 model scale											
Mesh no.	x min	x max	y min	y max	z min	z max	Cell size	No cells x	No cells y	No cells z	Sum cells
[-]	[m]	[m]	[m]	[m]	[m]	[m]	[m]	[-]	[-]	[-]	[-]
1	-0.3846	0.0000	1	1.0015	1.1538	1.4615	0.0015	250	1	200	50000
2	0.0615	0.1538	1	1.0015	1.2154	1.4308	0.0015	60	1	140	8400
3	0.3077	0.6154	1	1.0015	0.8462	1.2769	0.0015	200	1	280	56000
4	0.6154	1.5385	1	1.0015	0.8462	1.2615	0.0015	600	1	270	162000
5	0.1538	0.2308	1	1.0015	1.1231	1.3846	0.0015	50	1	170	8500
6	0.2308	0.3077	1	1.0015	1.0308	1.3077	0.0015	50	1	180	9000
7	0.0000	0.0615	1	1.0015	1.1923	1.4615	0.0015	40	1	175	7000
										Sum	300900

Table D-5 Individual mesh block data, mesh 1:3 model scale simulation

Mesh block arrangement 1:3 model scale											
Mesh no.	x min	x max	y min	y max	z min	z max	Cell size	No cells x	No cells y	No cells z	Sum cells
[-]	[m]	[m]	[m]	[m]	[m]	[m]	[m]	[-]	[-]	[-]	[-]
1	-0.3846	0.0000	1	1.0031	1.1538	1.4615	0.0031	125	1	100	12500
2	0.0615	0.1538	1	1.0031	1.2154	1.4308	0.0031	30	1	70	2100
3	0.3077	0.6154	1	1.0031	0.8462	1.2769	0.0031	100	1	140	14000
4	0.6154	1.5385	1	1.0031	0.8462	1.2615	0.0031	300	1	135	40500
5	0.1538	0.2308	1	1.0031	1.1231	1.3846	0.0031	25	1	85	2125
6	0.2308	0.3077	1	1.0031	1.0308	1.3077	0.0031	25	1	90	2250
7	0.0000	0.0615	1	1.0031	1.1923	1.4615	0.0031	20	1	87.5	1750
										Sum	75225

Appendix E. Original drawings and data extrapolation

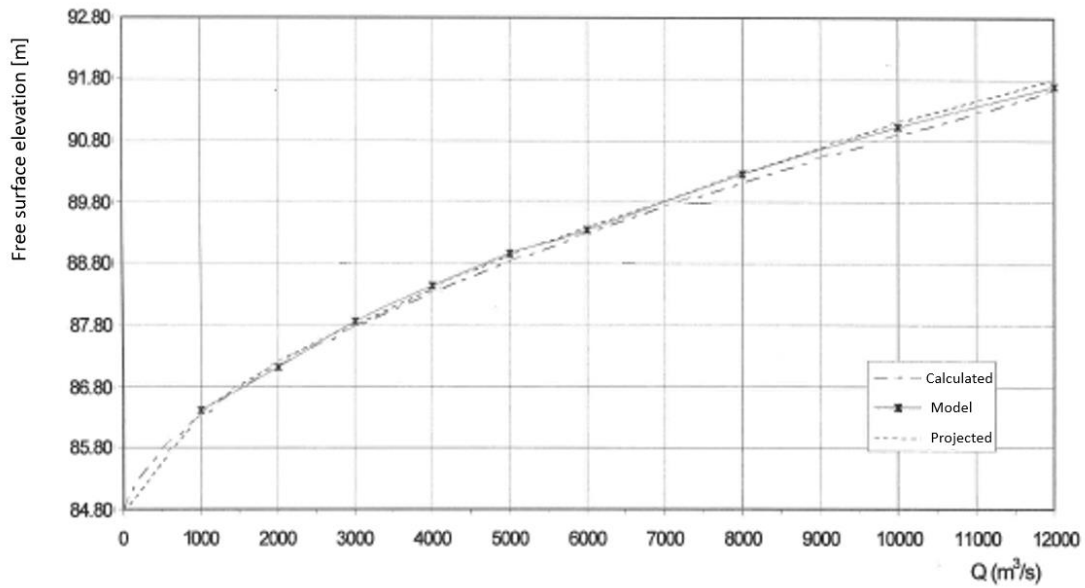


Figure E-1 Rating curve of the Pedrógão dam spillway; designer computation, prototype and semiempirical formula, as well as physical model (adapted from [34])

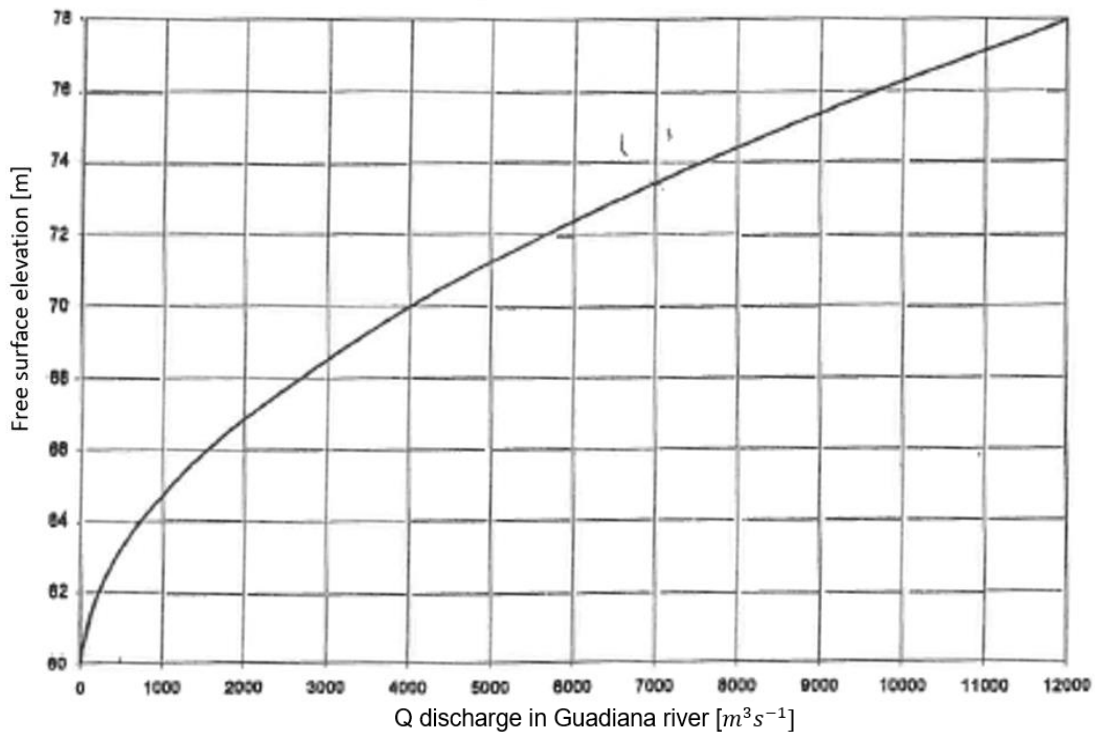


Figure E-2 Rating curve downstream of Pedrógão dam (adapted from [34])

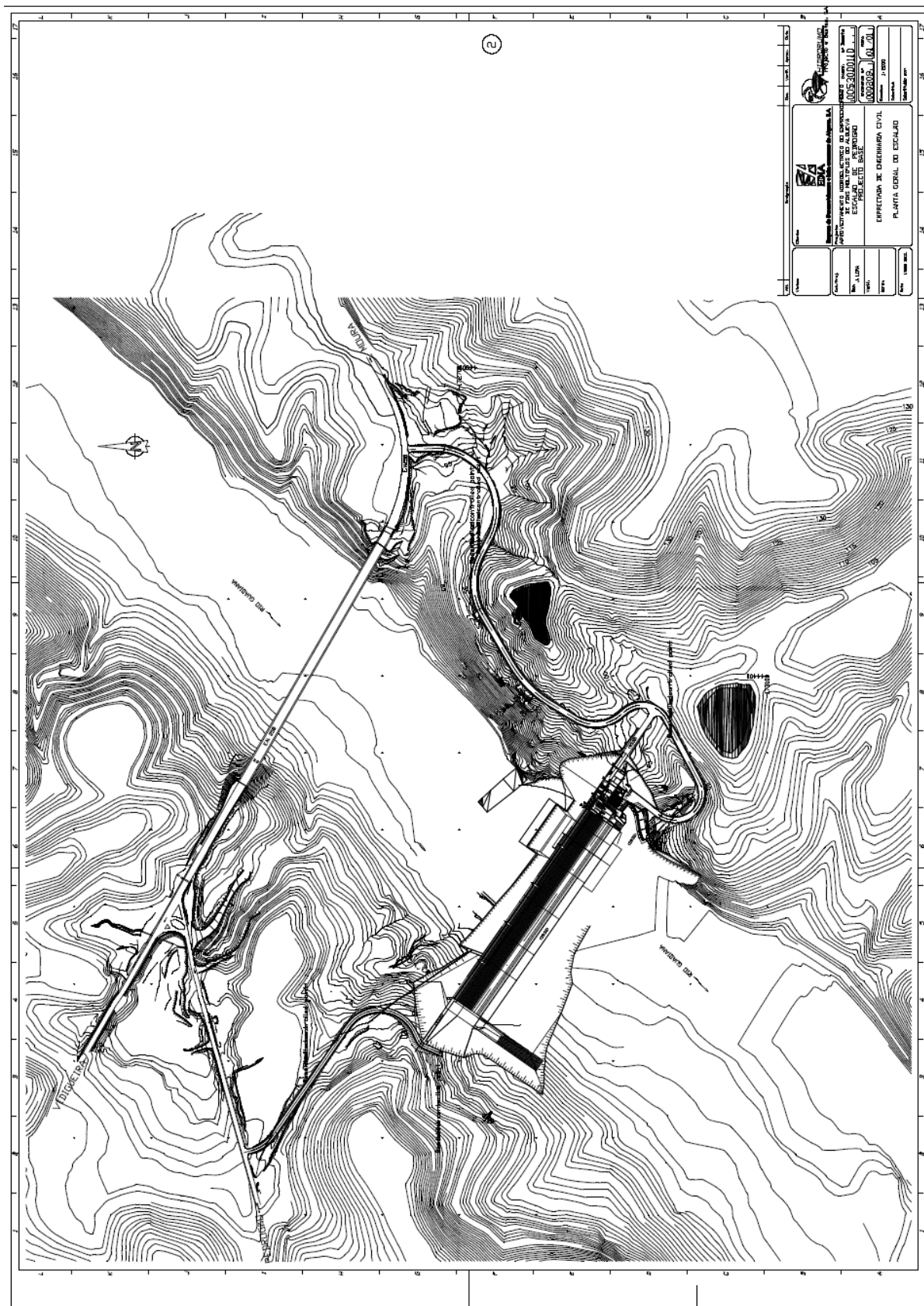
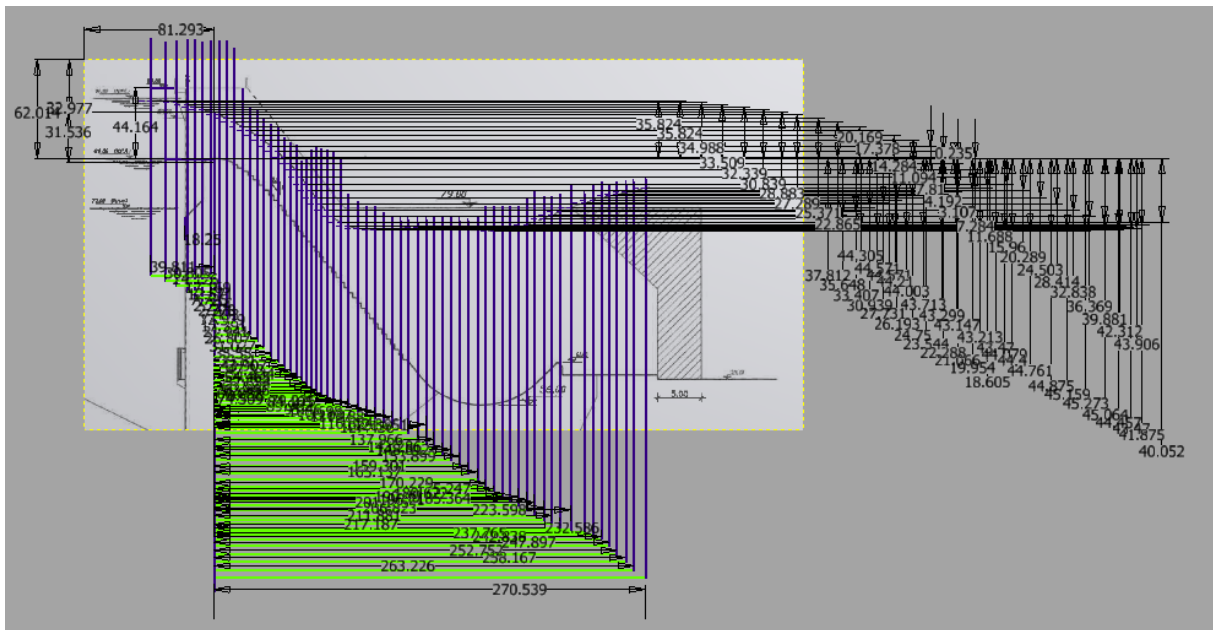


Figure E-4 Original plans, showing the topography of the surrounding area of Pedrógão [36]



Appendix F. Flow depth and velocity profile comparative analyses tables

Table F-1 Flow depth comparisons per step along the chute, LNEC experimental data as baseline

Compare to LNEC right wall	Analytical method		1:6 RNG prototype scale		1:6 RNG model scale		
	L/Li	δ abs.	δ	δ abs.	δ	δ abs.	δ
	[-]	[m]	[%]	[m]	[%]	[m]	[%]
	6.23E-03	-0.10	2.52	-0.28	7.04	-0.40	10.14
	1.16E-02	-0.05	1.28	-0.12	3.07	-0.35	9.04
	2.19E-02	0.06	1.58	0.13	3.44	-0.20	5.17
	3.45E-02	0.18	4.76	0.14	3.65	-0.08	1.98
	5.27E-02	0.32	8.25	0.17	4.47	0.03	0.82
	7.43E-02	0.43	11.31	0.26	6.83	0.12	3.05
	1.04E-01	0.54	14.30	0.44	11.66	0.20	5.25
	1.36E-01	0.64	16.86	0.50	13.24	0.32	8.48
	1.65E-01	0.70	18.60	0.60	16.05	0.33	8.86
	2.01E-01	0.78	20.79	0.52	13.85	0.39	10.52
	2.14E-01	0.85	22.66	0.55	14.66	0.40	10.69
	2.27E-01	0.89	24.11	0.68	18.37	0.53	14.31
	2.40E-01	0.93	25.28	0.48	13.13	0.50	13.67
	2.53E-01	0.96	26.32	0.56	15.39	0.46	12.69
	2.66E-01	0.99	27.40	0.64	17.62	0.60	16.52
	2.79E-01	1.04	28.77	0.73	20.33	0.59	16.39
	2.92E-01	1.12	30.78	0.77	21.13	0.64	17.57
	Average		16.80		12.00		9.71
	Maximum		30.78		21.13		17.57

Table F-2 Flow depth comparisons per step along the chute, analytical prediction results as baseline

Compare to analytical method	Experimental data right wall		1:6 RNG prototype scale		1:6 RNG model scale	
	δ abs.	δ	δ abs.	δ	δ abs.	δ
L/Li	[m]	[%]	[m]	[%]	[m]	[%]
6.23E-03	0.10	2.45	-0.18	4.41	-0.30	7.44
1.16E-02	0.05	1.27	-0.07	1.77	-0.30	7.66
2.19E-02	-0.06	1.60	0.07	1.89	-0.26	6.85
3.45E-02	-0.18	5.00	-0.04	1.17	-0.26	7.08
5.27E-02	-0.32	9.00	-0.14	4.12	-0.28	8.10
7.43E-02	-0.43	12.75	-0.17	5.05	-0.31	9.32
1.04E-01	-0.54	16.69	-0.10	3.09	-0.34	10.57
1.36E-01	-0.64	20.28	-0.14	4.35	-0.32	10.08
1.65E-01	-0.70	22.85	-0.10	3.14	-0.37	11.96
2.01E-01	-0.78	26.24	-0.26	8.76	-0.39	12.96
2.14E-01	-0.85	29.30	-0.30	10.35	-0.45	15.48
2.27E-01	-0.89	31.77	-0.21	7.56	-0.36	12.92
2.40E-01	-0.93	33.83	-0.45	16.25	-0.43	15.53
2.53E-01	-0.96	35.71	-0.40	14.82	-0.49	18.49
2.66E-01	-0.99	37.74	-0.35	13.47	-0.39	14.99
2.79E-01	-1.04	40.39	-0.30	11.85	-0.45	17.38
2.92E-01	-1.12	44.46	-0.35	13.93	-0.48	19.09
3.05E-01			-0.40	16.07	-0.42	17.01
3.18E-01			-0.39	16.14	-0.48	19.94
3.31E-01			-0.33	13.80	-0.46	19.37
3.44E-01			-0.26	11.27	-0.50	21.26
Average		21.84		8.73		13.50
Maximum		44.46		16.25		21.26

Table F-3 Velocity average differences to simulation results 1:12 k-ε, per step

Step	L/L_i	1:6 k-ε	1:3 k-ε	1:6 RNG k-ε	1:3 RNG k-ε
[-]	[-]	[%]	[%]	[%]	[%]
1	0.037	0.227	0.461	0.227	0.476
2	0.047	0.061	0.284	0.061	0.329
3	0.059	0.022	0.189	0.022	0.194
4	0.071	0.068	0.256	0.068	0.245
5	0.084	0.021	1.192	0.021	1.188
6	0.097	0.095	2.135	0.095	2.144
7	0.112	0.104	0.241	0.104	0.236
8	0.125	0.114	0.356	0.114	0.370
9	0.139	0.016	0.242	0.016	0.254
10	0.152	0.038	0.226	0.038	0.227
11	0.165	0.244	0.510	0.244	0.496
12	0.178	0.024	0.223	0.024	0.221
13	0.191	0.280	1.991	0.280	0.952
14	0.204	0.016	2.496	0.016	2.527
15	0.217	0.182	0.193	0.182	0.198
16	0.230	0.067	0.311	0.067	0.281
17	0.243	0.098	0.206	0.098	0.202
18	0.256	0.018	3.805	0.018	3.817
19	0.269	0.241	0.322	0.241	0.325
20	0.282	0.165	0.637	0.354	0.648
21	0.295	0.022	0.216	0.022	4.097
22	0.309	0.386	0.000	0.386	3.553

Appendix G. Steady state screenshots

All following graphs use seconds as dimension for time and the parameter, mass-averaged fluid mean kinetic energy uses J/kg, mass-averaged turbulent dissipation uses J/kg/s and mass-averaged turbulent kinetic energy uses J/kg. Any simulation not starting a zero seconds is a restart simulation. The reasons for a restart simulation vary, they might be computational optimisation attempts to use the previous steady state simulation state as baseline, or technical restarts necessary due to power cut outs, windows updates and similar.

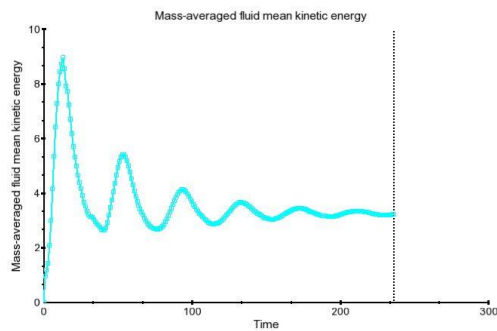


Figure G-1 Mass-averaged fluid mean kinetic energy for 1:3 RNG $k - \epsilon$ model scale ($Q = 7000m^3s^{-1}$)

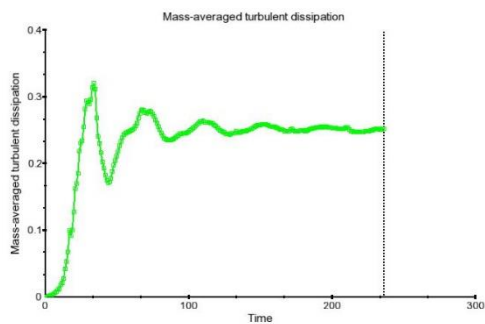


Figure G-2 Mass-averaged turbulent dissipation for 1:3 RNG $k - \epsilon$ model scale ($Q = 7000m^3s^{-1}$)

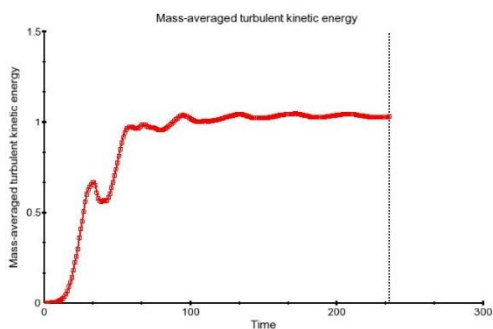


Figure G-3 Mass-averaged turbulent kinetic energy for 1:3 RNG $k - \epsilon$ model scale ($Q = 7000m^3s^{-1}$)

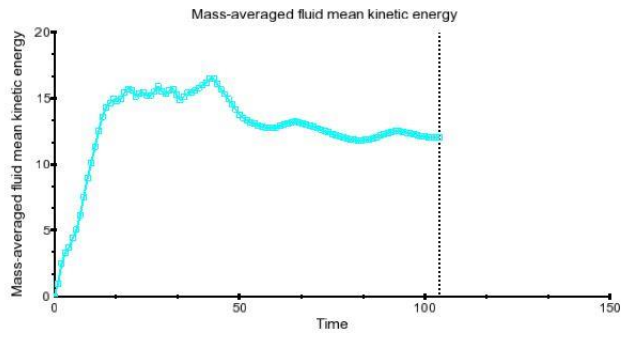


Figure G-4 Mass-averaged fluid mean kinetic energy for 1:3 k- ε prototype scale ($Q = 12000m^3s^{-1}$)

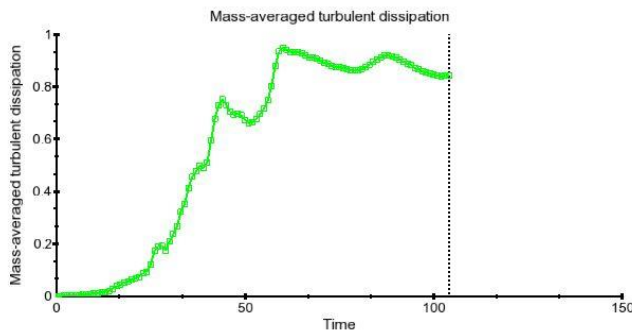


Figure G-5 Mass-averaged turbulent dissipation for 1:3 k- ε prototype scale ($Q = 12000m^3s^{-1}$)

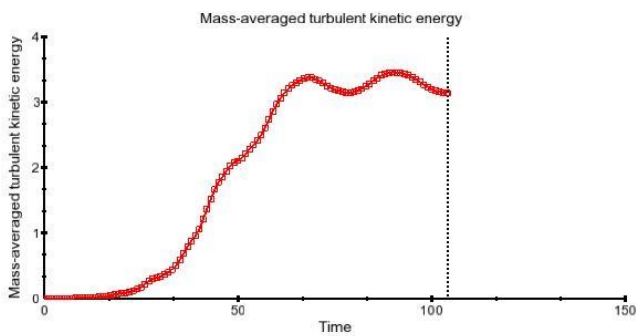


Figure G-6 Mass-averaged turbulent kinetic energy for 1:3 k- ε prototype scale ($Q = 12000m^3s^{-1}$)

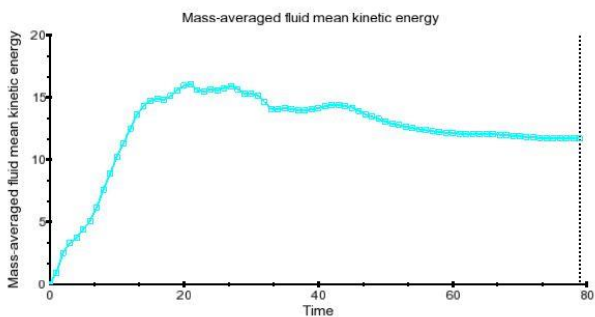


Figure G-7 Mass-averaged fluid mean kinetic energy for 1:3 RNG k- ε prototype scale ($Q = 12000m^3s^{-1}$)

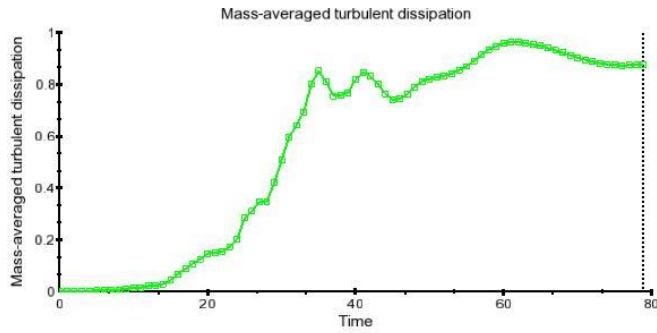


Figure G-8 Mass-averaged turbulent dissipation for 1:3 RNG k- ϵ prototype scale ($Q = 12000m^3s^{-1}$)

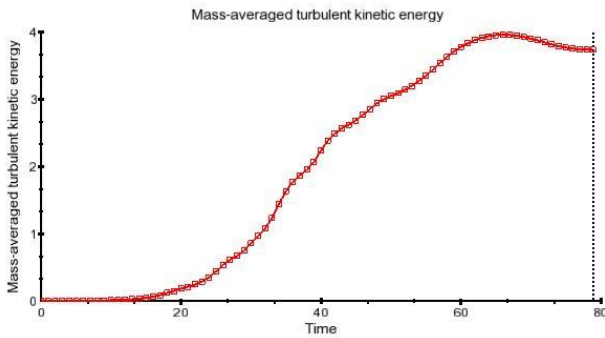


Figure G-9 Mass-averaged turbulent kinetic energy for 1:3 RNG k- ϵ prototype scale ($Q = 12000m^3s^{-1}$)

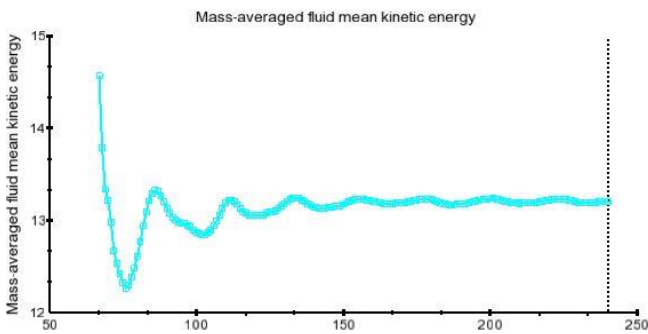


Figure G-10 Mass-averaged fluid mean kinetic energy for 1:6 k- ϵ prototype scale ($Q = 12000m^3s^{-1}$)

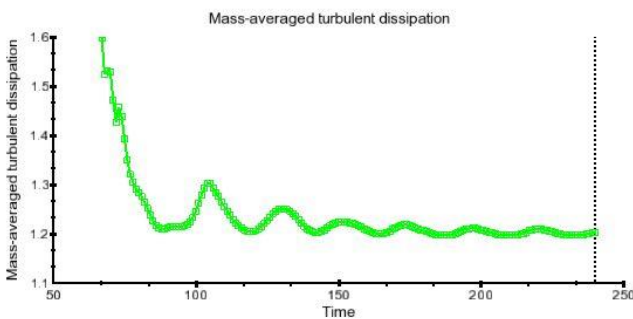


Figure G-11 Mass-averaged turbulent dissipation for 1:6 k- ϵ prototype scale ($Q = 12000m^3s^{-1}$)

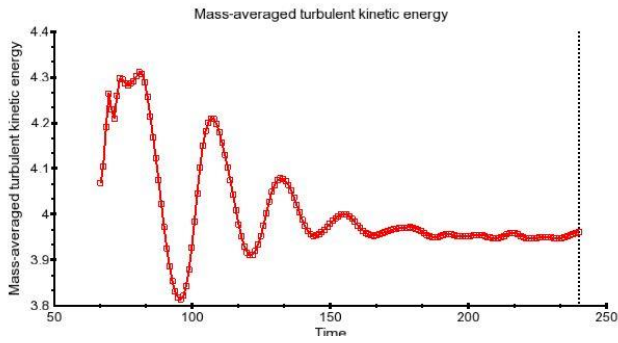


Figure G-12 Mass-averaged turbulent kinetic energy for 1:6 k-ε prototype scale ($Q = 12000m^3s^{-1}$)

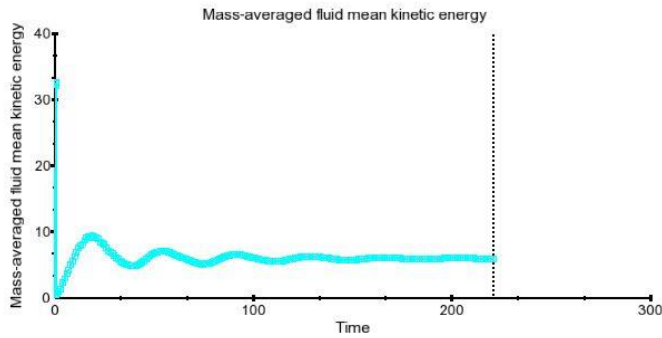


Figure G-13 Mass-averaged fluid mean kinetic energy for 1:6 RNG k-ε model scale ($Q = 12000m^3s^{-1}$)

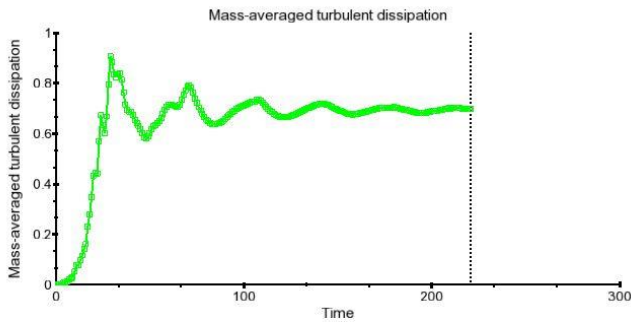


Figure G-14 Mass-averaged turbulent dissipation for 1:6 RNG k-ε model scale ($Q = 12000m^3s^{-1}$)

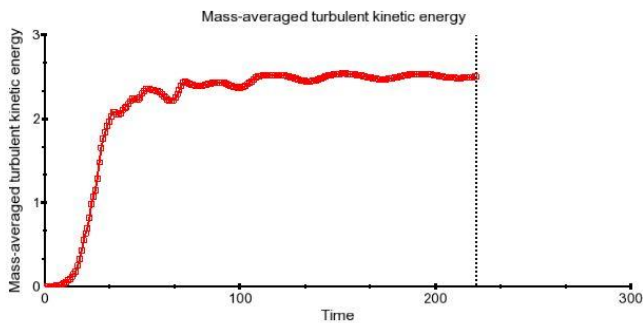


Figure G-15 Mass-averaged turbulent kinetic energy for 1:6 RNG k-ε model scale ($Q = 12000m^3s^{-1}$)

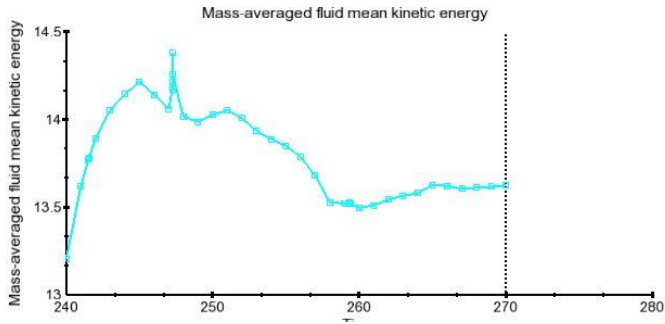


Figure G-16 Mass-averaged fluid mean kinetic energy for 1:12 k- ϵ prototype scale ($Q = 12000m^3s^{-1}$)

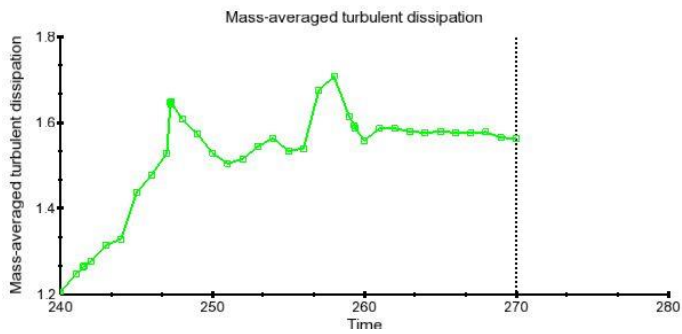


Figure G-17 Mass-averaged turbulent dissipation for 1:12 k- ϵ prototype scale ($Q = 12000m^3s^{-1}$)

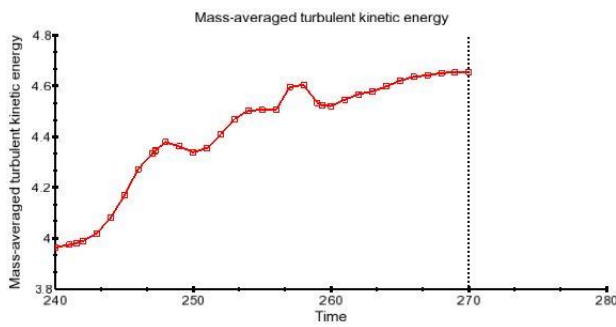


Figure G-18 Mass-averaged turbulent kinetic energy for 1:12 k- ϵ prototype scale ($Q = 12000m^3s^{-1}$)

Appendix H. Boundary layer recognition coding suggestion

Suggestion with step by step evaluation of data points.

```
Data[ ];           //velocity data array
Cord_x [ ];       //x coordinate of the corresponding velocity array
Coord_y[ ];      //y coordinate of the corresponding velocity array

I= 0;            //pointer lowest data point in the average
J= length(data)-1; //highest point in the average
Percentage= 0.01; //percentage deviation from u_max to define boundary layer

Do
Sum=0;
For ii,0,1,length(data)-1
    Sum = data[ii]+Sum;
    Avg = sum/ii;
End

If (abs(v[i]- v[i+1]) > abs(v[j]-v[j-1]))
    I=i+1;
Else
    J=j-1;
end

While ((avg-data[i])/avg > percentage or (avg-data[j])/avg > percentage)
// exit function, cut the next value as long as the lowest boundary layer velocity is higher than 1% different than
//the average value or as long as the highest value velocity value is more than 1% different.
Boundary x coord = Cord_x [i];
Boundary y coord = Cord_y [i];
```

Appendix I. Simulation overview on different times

Time = 107.00

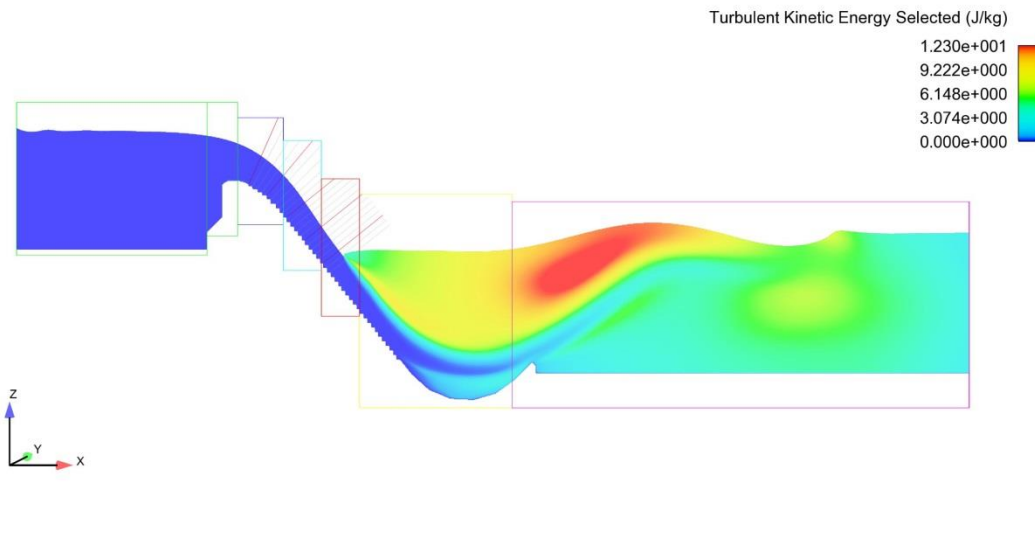


Figure I-1 Simulation overview of 1:6 k- ϵ at time 107 s, colour scaling with velocity

Time = 134.00

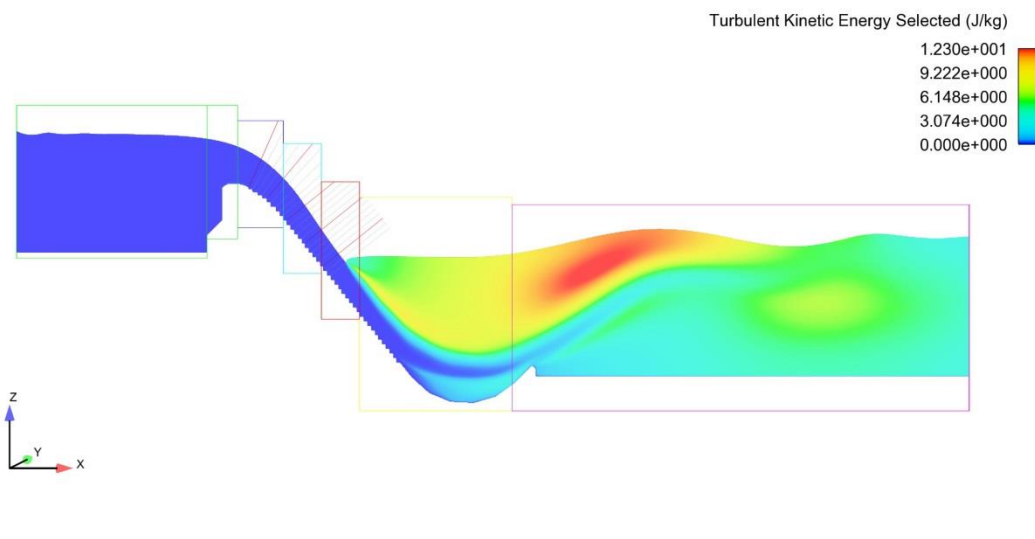


Figure I-2 Simulation overview of 1:6 k- ϵ at time 134 s, colour scaling with velocity

Time = 213.00

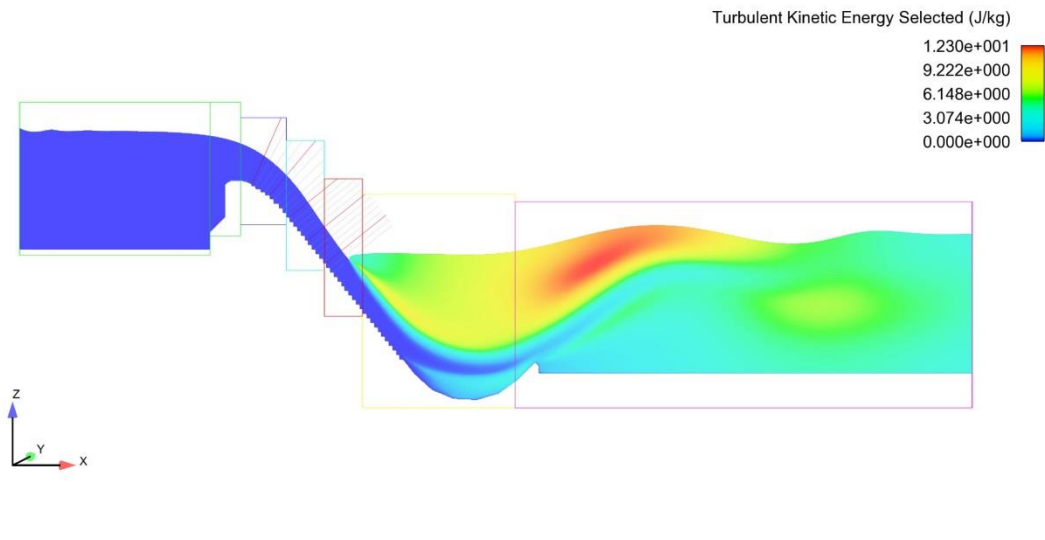


Figure I-3 Simulation overview of 1:6 k- ϵ at time 213 s, colour scaling with velocity

Time = 220.00

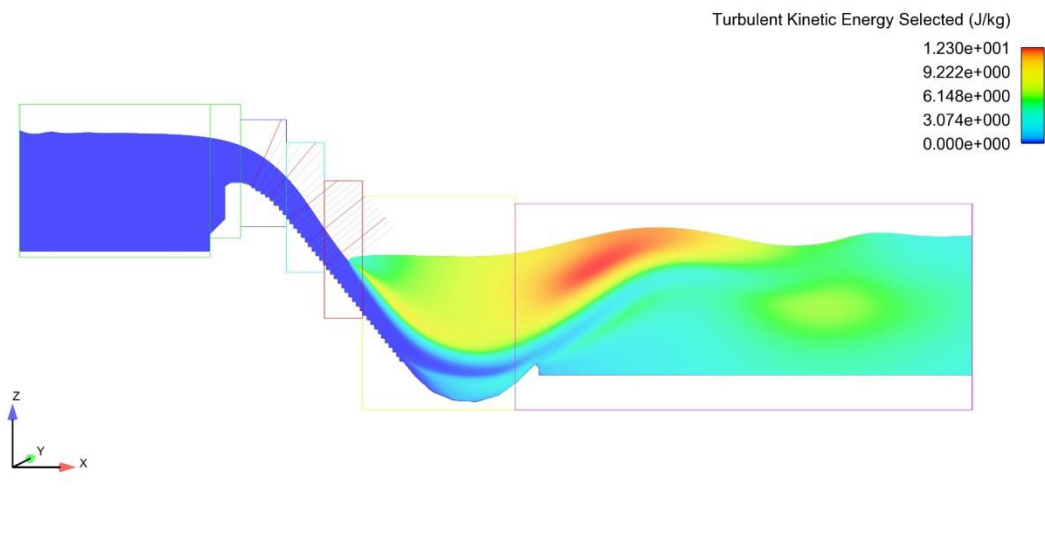


Figure I-4 Simulation overview of 1:6 k- ϵ at time 220 s, colour scaling with velocity